

DESIGN AND ANALYSIS OF A NOVEL COMPOSITE AXIAL
IMPELLER FOR COMPRESSING WATER VAPOR AS
REFRIGERANT

By

Qubo Li

A DISSERTATION

Submitted to
Michigan State University
in partial fulfillment of the requirements
for the degree of

DOCTOR OF PHILOSOPHY

MECHANICAL ENGINEERING

2010

ABSTRACT

DESIGN AND ANALYSIS OF A NOVEL COMPOSITE AXIAL IMPELLER FOR COMPRESSING WATER VAPOR AS REFRIGERANT

By

Qubo Li

In order to compress water vapor as refrigerant, most modern impeller confronts a lot of challenges since the impeller has to be made with strict material and structure requirements. This thesis investigates a novel composite axial impeller to achieve the compression goal which is also able to solve those challenges. Based on an advanced concept, this thesis realizes automatic manufacturing of a composite impeller, as well as an analysis of its mechanical properties, and rotor dynamic and aerodynamic performance analyses.

To compress water vapor as a refrigerant, the typical refrigeration cycle process is modified in such a way that the coefficient of performance is increased approximately 30%. The modified imposes requirements to rotating impellers such as rotating speed, pressure ratio and efficiency. In order to produce an impeller with satisfied mechanical properties, a CNC machine based platform is developed for automated manufacture; its mechanical properties are experimentally tested and results show that this approach is able to manufacture the quality of composite impeller as desired. A new methodology is developed to predict the composite rotating impeller's fatigue life, especially for ones with complicated geometries when aerodynamic force is not negligible. The impeller's patterns' effects, from aerodynamic views, are compared and flow structure inside of a blade-angle-optimized impeller channel shows that a serious boundary layer separation exists between 30% and 50% of impeller span zone.

The investigation brings a concept up to the table and develops a novel axial composite impeller for compressing water vapor as refrigeration. Using this axial impeller, blade angle and geometries have been optimized to prevent boundary layer separation and through investigation, it demonstrates specific pressure ratio and efficiency can be achieved to reach the goal of compressing water vapor as refrigerant.

ACKNOWLEDGMENTS

The Ph.D process at Michigan State University is an eye-opening experience in my life. I would like to express my gratitude to the people who offered help during my stay at MSU.

First, I would like to thank my advisor Dr. Norbert Müller for the opportunity of this interesting project and his support throughout the research. I am privileged to have Dr. Abraham Engeda in my thesis committee who gave me valuable suggestions with insightful comments and questions about the project I am doing. I also want to thank Dr. Elias G. Strangas and Dr. Gaetano Restivo for all their kind advice on different issues. Special thanks are needed to Dr. Janusz Piechna for his valuable guidance for my Ph.D work during his short time staying at MSU.

Much gratitude is extended to all students at MSU turbomachinery laboratory who have provided me with all kinds of teaching and discussion opportunities, in particular Marco Vagani and Christopher Bolin who taught me much about the art of turbomachinery among many other things when I started the program, Jifeng Wang for his help with ANSYS operation guidance, Guangwei Sun for his help with Matlab coding, Mohit Patil for assisting with the equipments and setup of the experiment, Dave Kempf, Zachary Sprinkle and Blake Gower for their English correction to my publications, Eric Tarkleson, Dervesh Chapalkar, Raul Quispe, Parraga Pablo Francisco and Dave Rayman for their cooperation with experiment test and data collection, Pierre Burck for his help with wheel winding, Dan Swain's introduction about America.

I am deeply indebted to my parents and parents in law for their love and unconditional support. I owe my aunt a big thank you for encouraging all the time for my study and life abroad. I also want to thank my brother for taking care of my parents while I am absent during the past

years. The sincerest thank you from the bottom of my heart goes to my wife Yi, who sacrificed much so that I can keep moving forward. I cannot imagine going through the toughest time in the Ph.D process without her love and support.

This research was funded by ASHRAE whose supports are gratefully acknowledged.

Qubo Li

Nov-25-2010

CONTENT

LIST OF TABLES	viii
LIST OF FIGURES	ix
NOMENCLATURE	xiii
CHAPTER 1 Introduction.....	1
1.1 Background.....	1
1.2 Previous Work.....	3
1.2.1 Water Vapor Refrigerant Cycle	3
1.2.2 Refrigeration Turbo Compressor	4
1.2.3 Woven Impeller.....	5
1.3 Research Objectives.....	7
1.4 Technical Approach	8
1.5 Thesis Organization	8
1.6 Thesis Contribution.....	9
CHAPTER 2 Refrigeration Cycle for Water Vapor Refrigerant.....	10
2.1 Introduction.....	10
2.2 Cycle Modification	11
2.2.1 Single Stage Vapor Compression Cycle.....	12
2.2.2 Multi Stage Vapor Compression Cycle.....	15
2.3 Summary.....	20
CHAPTER 3 Manufacturing and Mechanical Characterization of Woven Wheel.....	21
3.1 Manufacturing of Composite Impeller.....	21
3.1.1 Description of Facility	21
3.1.2 Material Selection	23
3.1.3 Design and Manufacturing Process	24
3.2 Mechanical Characterization	26
3.2.1 Determination of Composite Density and Volume Fraction Measurement	26
3.2.2 Specimen Blade Theoretical Properties	28
3.2.3 Effective Specimen Blade Thickness.....	28
3.2.4 Experimental Procedures for the Determination of Mechanical Properties	30
3.2.5 Specimen Blade Strain and Stress Characteristic	32
3.3 Discussion.....	33
3.3.1 Manufacturing Cost	33
3.3.2 Mechanical Properties.....	34
3.3.3 Manufacturing Issues.....	35
3.4 Summary.....	35

CHAPTER 4	Pattern Aerodynamic Comparison	37
4.1	Investigated Impeller Geometries	37
4.2	Blade angle comparison	39
4.3	Numerical Model Setup	40
4.3.1	Assumptions	40
4.3.2	Conservation Equations	40
4.3.3	Boundary Conditions	42
4.3.4	Grid Generation	42
4.3.5	Model Parameter	42
4.4	Results and Discussion	43
4.4.1	Overall Performance Comparison at the Same Rotating Speed	43
4.4.2	Hub's Effect	47
4.4.3	Patterns Effect	50
4.5	Summary	59
CHAPTER 5	Fatigue Life Evaluation to Composite Impeller	60
5.1	Introduction	60
5.2	Modeling	62
5.3	Loading	64
5.4	Composite material's mechanical properties	66
5.5	Strength Analysis Under Centrifugal Force	67
5.6	Strength Analysis Under Peak Aerodynamic Flow	71
5.7	Accumulated Fatigue Damage	75
5.8	Life Prediction Results and Discussion	76
5.9	Summary	79
CHAPTER 6	Aerodynamic Flow Structure Inside of Woven Wheel Channel	81
6.1	Investigated impeller blade angle	81
6.2	Results and Discussion	85
6.2.1	Case 1 0.54 hub/tip ratio	86
6.2.2	Case 2 0.75 hub/tip ratio	96
6.3	Summary	101
CHAPTER 7	Summary and Conclusions	104
7.1	Summary	104
7.2	Conclusions	104
7.3	Contributions	105
7.4	Recommendations for Future Work	106
BIBLIOGRAPHY	108

LIST OF TABLES

Table 2-1	Operating conditions used for analysis.....	20
Table 3-1	Strength properties for some typical materials [18]	23
Table 3-2	Kevlar fiber reinforced epoxy laminate properties from micromechanical theory and experimental results	32
Table 4-1	Typical winding patterns for endless fibers.....	37
Table 4-2	Six cases studied for the axial compressors	38
Table 4-3	Summary of performance for each case	43
Table 5-1	Material mechanical properties (GPa).....	66
Table 5-2	Strength analysis of blade under different events 8C.....	69
Table 5-3	Strength analysis of blade under different events 8B.....	69
Table 5-4	Linear elastic FEM analysis results for 8C.....	74
Table 5-5	Linear elastic FEM analysis results for 8B.....	74
Table 5-6	Life prediction results of patterns.....	79

LIST OF FIGURES

Figure 1-1 Demonstration of inlet and outlet for axial, mixed flow, and centrifugal compressor [4].....	2
Figure 1-2 Multiple axis winding machine, left: Fiber wetting with one bath, right: controlled alternative fiber wetting with two paths [12].....	6
Figure 1-3 Simulated patterns from endless winding [13].....	6
Figure 1-4 Weaving composite impeller on hands [13].....	7
Figure 2-1 Pressure-specific volume diagrams of ideal water and R- 134a vapor compression refrigeration cycles [3].....	11
Figure 2-2 Turbo chiller employing R718 Refrigeration cycle	13
Figure 2-3 Vapor compression cycle with single stage compression	14
Figure 2-4 R 718 Vapor compression cycle with seven stage compression.....	16
Figure 2-5 Comparison of COP between water and R134a.....	19
Figure 2-6 Temperature at each stage's outlet after intercooling and mass percentage of flash water sprayed	20
Figure 3-1 Layout of filament winding facility	22
Figure 3-2 Mandrel picture of an 8-slot pattern.....	24
Figure 3-3 One complete layer for endless fiber winding (left) Computer model wound with single endless fibers (center) Filament wound composite impeller (right).....	25
Figure 3-4 Composite impeller wheel integrated with mandrel (left) Demonstrate with frequency inverter drive @10,000RPM (right).....	26

Figure 3-5	Photograph of static strain-stress measurement	30
Figure 3-6	Comparison of manufacturing hours for steel, thermoset and thermoplastic-composite versions of impeller	34
Figure 4-1	8B pattern rotor for different ratios: 0.43 (left), 0.54(middle) and 0.75(right)	38
Figure 4-2	8C pattern rotor for different ratios: 0.43 (left), 0.54(middle) and 0.75(right)	38
Figure 4-3	Blade angle distribution: leading edge (a) and trailing edge (b).....	39
Figure 4-4	Comparison of performance between different hub sizes for pattern 8C	45
Figure 4-5	Comparison of performance between different hub sizes for pattern 8B	46
Figure 4-6	Velocity field on the middle planes of pattern C at peak performance point (a) Case 1 and (b) Case 3	48
Figure 4-7	Mach number contour on the middle planes of pattern C at the mass flow rate of 1kg/s (a) 0.43ratio (b) 0.54 ratio (c) 0.75 ratio	49
Figure 4-8	Performance comparison between two patterns at the same hub/shroud ratio of 0.43	52
Figure 4-9	Streamwise variation at 1.3kg/s mass flow rate, (a) total pressure ratio (b) total temperature	53
Figure 4-10	Velocity field on the middle planes of two patterns at the same mass flow rate 1.3kg/s (a) pattern C (b)pattern B	55
Figure 4-11	Performance comparison between two patterns at the same hub/shroud ratio of 0.54	56
Figure 4-12	Performance comparison between two patterns at the same hub/shroud ratio of 0.75	58

Figure 5-1	Schematic S-N curve for different industrial components [42]	61
Figure 5-2	Rotor 3D 8C(left) and 8B(right) patterns.....	63
Figure 5-3	Convergence graphs of FE model.....	64
Figure 5-4	Forces acting on a 2D blade.....	65
Figure 5-5	Von Mises equivalent stress distribution for pattern 8C.....	70
Figure 5-6	Keypoint location in the critical section.....	70
Figure 5-7	Von Mises equivalent stress distribution for pattern 8B.....	71
Figure 5-8	FLUENT static pressure distribution on the blade for 8C	72
Figure 5-9	FLUENT static pressure distribution on the blade for 8B	73
Figure 5-10	Transient static pressure trend at weak point under 9,000RPM for 8C	73
Figure 5-11	S-N for unidirectional carbon/epoxy composite material under longitudinal loading [52].....	76
Figure 5-12	Loadings for blade life determination.....	77
Figure 6-1	Axial-line blading without hub	84
Figure 6-2	Blade angle along radial direction.....	85
Figure 6-3	Total pressure ratio curve (a) and isentropic efficiency curve (b) at different $r < 1$ rotational speed ratio (0.54ratio).....	87
Figure 6-4	Total pressure ratio curve (a) and isentropic efficiency curve (b) at different $r > 1$ rotational speed ratio (0.54ratio).....	88

Figure 6-5 Flow angle and blade angle of the rotor at different rotating speed ratio stall point (0.54ratio).....	89
Figure 6-6 Rotor's pitch averaged total pressure ratio (a) and isentropic efficiency (b) at peak efficiency point ($r < 1$).....	91
Figure 6-7 Counter rotor's pitch averaged total pressure ratio (a) and isentropic efficiency (b) at peak efficiency point ($r > 1$).....	92
Figure 6-8 Comparison of rotor's radial velocity distribution at peak efficiency – (a) 30% span, (b) 45% span, (c) 50% span.....	93
Figure 6-9 Total pressure ratio curve (a) and isentropic efficiency curve (b) at different $r < 1$ rotational speed ratio (0.75ratio).....	96
Figure 6-10 Total pressure ratio curve (a) and isentropic efficiency curve (b) at different $r > 1$ rotational speed ratio (0.75ratio).....	97
Figure 6-11 Rotor's pitch averaged total pressure ratio (a) and isentropic efficiency (b) at peak efficiency point ($r < 1$).....	100
Figure 6-12 Counter rotor's pitch averaged total pressure ratio (a) and isentropic efficiency (b) at peak efficiency point ($r > 1$).....	101

NOMENCLATURE

E	Young's modulus
ν	Poisson ratio
d	Fiber diameter
N	Number of fiber thread
t	Blade average thickness
V	Volume fraction
w	Blade width
θ	Angle between specimen axis and material axis
ε	Strain
σ	Stress
G	Shear modulus
C_p	Specific heat capacity under constant pressure
G_k	Generation of turbulence kinetic energy
R	Gas constant
u	Velocity
γ	Specific heat ratio
δ_{ij}	Kronecker delta
ε	Energy dissipation rate
κ	Turbulence kinetic energy
μ	Laminar viscosity
μ_t	Turbulent viscosity
ρ	Density

σ_k	Turbulent Prandtl number for k
σ_ϵ	Turbulent Prandtl number for ϵ
η_{is}	Isentropic efficiency
η_m	Mechanical efficiency
COP	Coefficient of performance
W_{is}	Isentropic work of compressor per cycle
W_c	Actual work of compressor
π_s	Pressure ratio of single compression stage
χ	Mass flow function
r	Speed ratio between rotor and counter rotor wheels
h	Enthalpy
\dot{m}	Mass flow rate
P	Pressure

SUBSCRIPT

1	Longitudinal direction
2	Transverse direction
f	fiber
m	Matrix
ref	Reference point

CHAPTER 1 Introduction

1.1 Background

This dissertation focuses on investigation of a novel composite turbo impeller used to compress water vapor as a refrigerant, where investigation related with composite impeller manufacturing, material mechanical properties, impeller fatigue, thermodynamic and aerodynamic properties will be conducted. Technology involving the use of this novel composite impeller to compress water vapor as refrigerant is new to turbomachinery area. The objective of this section is to provide the basic background of the use of water vapor refrigeration in turbomachinery.

Water is a chemically stable, non-toxic, non-flammable and easily recyclable substance, with no ozone depletion or global warming potential, which is freely available in nature [1]. It also has a performance comparable to conventional refrigerants when it is used in similar operating conditions for cooling applications above its freezing point [2]. Water is the most commonly used heat transfer fluid. Combining both duties of a refrigerant and a heat transfer media, the use of water as refrigerant can facilitate replacement of indirect heat exchange condensers and evaporators by direct contact condensers and evaporators, which contribute to the improvement of the overall performance of the system. Even though water is an ideal refrigerant for moderate temperature cooling, it has a very low vapor pressure and specific volume with a relative steep pressure rise in the application temperature range of common refrigerants used in air conditioning systems [3]. As a result, the compressor has to handle huge volume flow rates and relatively high pressure ratios. Hence, the water vapor compressor is a turbo compressor that has to be of larger diameter and higher speed than those for conventional refrigerants.

As one main category of turbomachinery, a turbo compressor usually contains several essential elements such as rotor and casing. Rotor is the rotating part and the most important component, through which energy transfers. After the rotor there typically follows stationary impellers, or guide vanes, where dynamic pressure is converted into static pressure. Casing provides a fluid boundary as guides to direct the flow. According to discharge flow's direction, turbo compressors can be classified as axial, mixed flow and centrifugal (or radial) compressors. The inlet and outlet flow directions of axial, mixed flow and centrifugal compressors can be demonstrated in Fig. 1-1. Usually an axial compressor has the benefit of compressing fluids at large volume flow rates while compression ratio per single stage is low; on the other hand, a centrifugal compressor is able to produce larger pressure ratios while the volume flow rate is typically smaller.

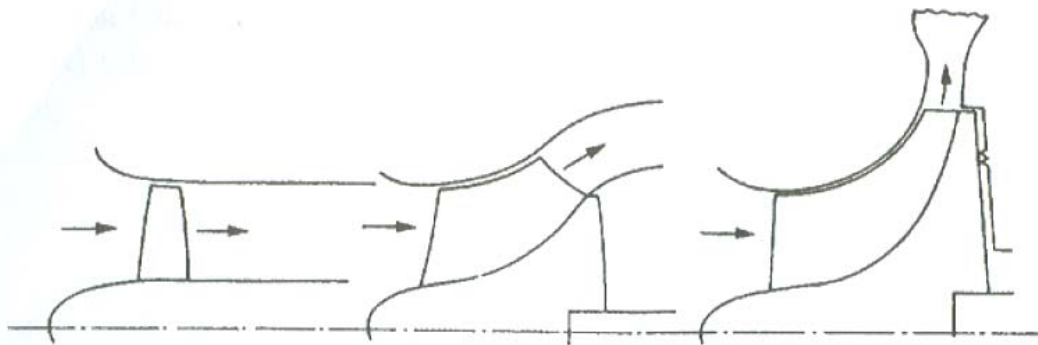


Figure 1-1 Demonstration of inlet and outlet for axial, mixed flow, and centrifugal compressor [4]

The application of the turbo compressor has a wide range including aerospace, automotive, refrigeration and air conditioning, etc. In refrigeration area, to achieve water vapor compression capacity through rotors, however the high cost of the compressor, due to production of blades made from high strength materials such as titanium and fiber composites to overcome radial

stresses due to high tip speed, has been the major obstacle for utilizing water as a refrigerant in significant scale in air conditioning systems [5].

1.2 Previous Work

In order to realize the goal of compressing water vapor as refrigerant in stead of conventional refrigerants such as R134a, several main work have been done related with turbo compressors.

The relevant previous work involved in compressing water vapor as refrigerant using turbo impeller is summarized below in four areas:

1. The thermodynamic cycle analysis of water vapor refrigerant
2. The technology of turbo compressor for refrigeration
3. The manufacturing of composite impeller
4. Woven wheel technology

1.2.1 Water Vapor Refrigerant Cycle

Kilicarslan and Müller showed that water has ideal properties as a refrigerant and a comparable efficiency with some refrigerants for a given range of evaporator temperature and temperature differences between the evaporator and condenser with single stage compression. Considering its environmental friendliness and availability, they stressed the need to develop suitable multistage turbo compressors for wider application [2]. Orshovn et al. explored potentials and limitations of water as a refrigerant for refrigeration and heat pump application above its freezing point and showed integration of the functions of water as refrigerant and heat transfer media; such as the case in ice production, which can make the application viable. Noting the large diameter of a centrifugal compressor required to handle the huge volume flow rate, they concluded that innovation is required in vacuum compression technology to use water as the working fluid in vapor compression refrigeration cycles [6]. Lachner et al. investigated the economic feasibility of a water-based vapor compression chiller with a nominal cooling capacity

of 1000 tons using component-level modeling to determine the system performance by simulating various cycle configurations. The capital cost and operating costs of the system were estimated, as was the payback period predicted for a system that utilizes turbo compressors. Though, it was concluded that the use of water as refrigerant at that time was not feasible, measures that may have an economic impact on the feasibility of water such as using integration of duties of refrigerant and heat transfer fluid and direct contact condensers were recommended [3]. Kuhn discussed the realization of chillers using water as refrigerant by employing flash cooling, a direct-contact type of condenser, and chilled water circulation from the evaporator to the cooling points. Kuhn concluded that due to the small temperature difference required between the inlet and outlet of direct contact condensers, that the system can have a better performance than systems employing other refrigerants. The disadvantages that were mentioned were the huge size of the compressor and its high cost as compared to conventional systems [7].

1.2.2 Refrigeration Turbo Compressor

In order to solve problems of the compression of water vapor, investigation on centrifugal and axial turbo compressor was sponsored by ARTI for determining optimal compressor size for 1000 tons of refrigeration capacity with evaporator temperature of 6.6 °C, pressure ratio of 6.8 and mass flow rate 1.8 kg/s. The results of the investigation showed that two-stage centrifugal compressor with 5490 rpm speed, 2.49 m impeller diameter, 5.4 m housing diameter and 77.4% efficiency was the first option. The second option was a seven stage axial compressor, 1.3m diameter and 3.2 m length, 6600 rpm and 82.6 % efficiency. The study made it clear that multi stage axial compressors are better candidates for water vapor compression due to smaller overall dimensions and a lower tip speed [8]. However as Lachner discussed, saying that the main disadvantage of using axial impellers as compressors is expensive comparing with centrifugal compressors. The use of the axial compressor is generally limited to high unit cost devices such

as jet engines and stationary gas turbines for power production. In addition, in order to reach high pressure ratio rotating impeller itself has to endure a large centrifugal stress which imposes strict requirements to impeller material and structure's design. It is therefore the impeller should be made of light-weight materials. Combinations of composites and materials such as titanium have already been used to fulfill such high performance requirements [9, 10], but the manufacturing approach involves a lot of labor and hence high costs. Attempts have been made to automate the composite manufacturing; ABB Corporation has explored robotic manufacturing of thermoplastic impellers [11], but handwork is still required to join individual subcomponents, which inherently raises accuracy issues and high laboring costs. Thus the reduction in cost of the production of an axial impeller to compress water vapor as refrigerant is the main challenge.

1.2.3 Woven Impeller

To manufacture a low cost and high performance composite impeller, Müller proposed a novel manufacturing concept to weave axial composite impeller with integrated motor on the shroud [12]; the whole manufacturing platform is based on a multiple axis winding machine where composite impeller can be wound automatically and a lot of laboring work thus was supposed to diminish resulting an extremely decrease of manufacturing cost. A brief demonstration can be shown to Fig. 1-2.

Since this method is to produce impeller through weaving process, it thus brings extra space to design a variety of impeller patterns, such as impeller blade goes through wheel's center just like conventional ones, impeller blade cross each other to form special patterns, etc. To realize the concept, Allen not only simulated weaving process in computer, but also produced the first woven wheel with different patterns on hands [13]. As it is shown in Fig.1-3, these are two main patterns which are able to manufacture in this method and patterns can be varied according to different blade number and blade angle requirements. Fig.1-4 demonstrates how the wheel can

be manufacture on hands and it is easily seen that the manufacturing process is still not matured to make impeller blade surface smooth enough for high Reynolds number fluid rotating environment.

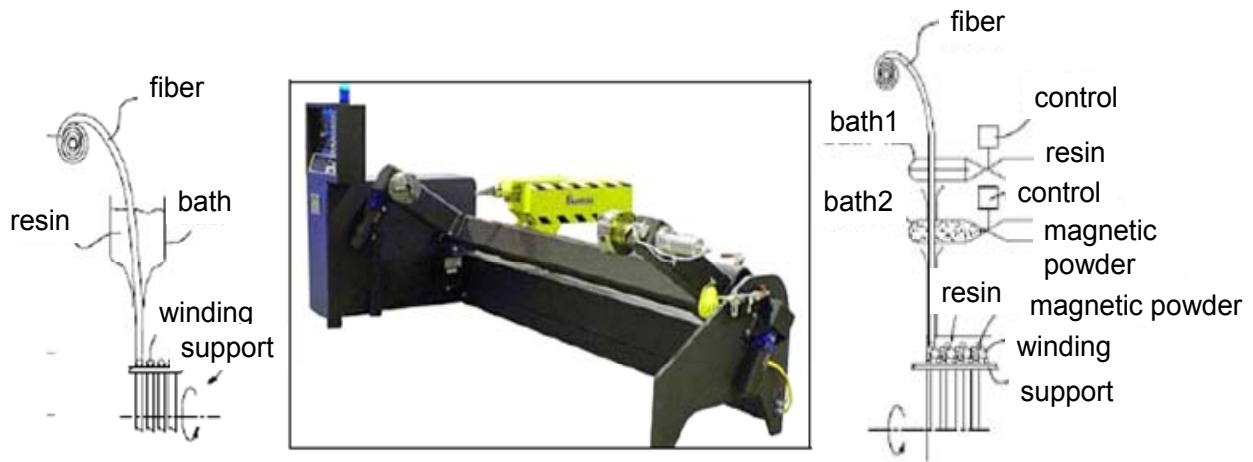


Figure 1-2 Multiple axis winding machine, left: Fiber wetting with one bath, right: controlled alternative fiber wetting with two paths [12]

For interpretation of the references to color in this and all other figures, the reader is referred to the electronic version of this dissertation

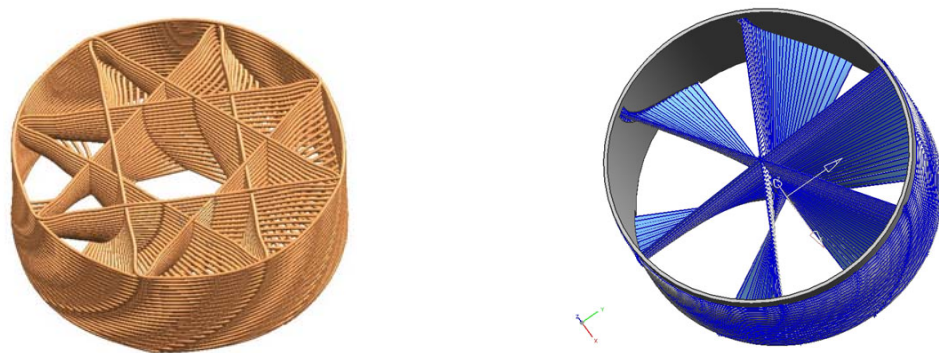


Figure 1-3 Simulated patterns from endless winding [13]



Figure 1-4 Weaving composite impeller on hands [13]

However, if hands can be replaced by machine motors, manufacturing costs for the impeller can be drastically less than conventional axial impellers and it is promising that the economic issues in the manufacture of composite impellers for water chillers can be solved. Yet as far as how well these impellers can perform in a refrigeration role, or if these impellers have thermodynamic potentials to compress water vapor as refrigerant, these are still unknown.

1.3 Research Objectives

The primary goal of this research is to investigate this novel composite impeller to compress water vapor as refrigerant. The work starts from Müller's proposal and Allen's initial work, through automatic manufacturing discussion, mechanical characterization of composite materials, refrigeration cycle modification analysis, fatigue study of woven wheel, to thermodynamic and aerodynamic analysis of water vapor flow inside of impeller channels.

The specific technical objectives of this research are to:

- 1) Develop an automatic manufacturing platform to produce composite impeller and experimentally characterize its mechanical properties for water chillers
- 2) Develop water vapor refrigeration cycle process and obtain cooling capacity requirements to the compressor
- 3) Identify woven wheel pattern's thermo-aerodynamic effect

- 4) Develop fatigue life evaluation method to predict woven wheel's fatigue failure
- 5) Design and numerically demonstrate flow structure inside of single counter rotating stage

1.4 Technical Approach

To achieve the primary objective of this research, experimental tests were used firstly to characterize impeller composite material's mechanical properties and through comparison between experimental results and proposed analytical method, conclusions were made. CAD models and finite element method were used to evaluate novel impeller's rotor dynamic properties such as stress strain behavior and fatigue life during different loading stages. Three dimensional and steady CFD tools were also used to simulate the flow field of different impeller patterns as well as flow structure inside of specific impeller channels. The data was processed to compare pattern's affect to impeller performance and understand flow behavior inside of the channel.

1.5 Thesis Organization

The modified refrigeration cycle to compress water vapor as refrigerant is discussed in Chapter 2. A new configuration advanced at Michigan State University is introduced: multi-stage counter rotating axial impellers consist of compressor stage and flash intercooling strategy is used to cool down superheated discharge gas into saturated temperature. Requirements to compress water vapor at specific air conditioning are advanced. Chapter 3 introduces the automatic manufacturing process and mechanical characterization of produced composite impeller is conducted. A discussion on the manufacturing cost comparing with traditional impeller manufacturing approaches is also presented. Chapter 4 compares several available impeller patterns thermo-aerodynamically using computational fluid dynamics approach. Based on the mechanical properties characterized in Chapter 3, Chapter 5 proposed a new methodology to evaluate composite impeller's fatigue life. Recommendations on how to evaluate fatigue life

more accurately for complex impeller geometry are proposed. Chapter 6 analyzes flow structure inside of novel impeller's channel and suggestions were made to enhance its performance.

1.6 Thesis Contribution

The major contributions of the research documented in this dissertation are:

- A new platform to automatic manufacturing composite impeller and characterize its mechanical properties
- Modified water cycle to improve coefficient of performance
- A new method to evaluate fatigue life of composite impeller
- Understanding woven wheel pattern's aerodynamic effect
- Understanding flow structure inside of complex impeller channels

CHAPTER 2 Refrigeration Cycle for Water Vapor Refrigerant

2.1 Introduction

An application of the investigated preliminary compressor design is in mechanical compression refrigeration units that utilize water (R718) as refrigerant. The use of water as refrigerant in vapor compression system offers several potentially significant advantages and fulfills most of the fundamental requirements of a refrigerant [14]. The first main advantage of using water as refrigerant is because it is a green refrigerant; it is environment friendly, non-toxic and non-flammable. Besides these, as a green refrigerant it has zero ozone depletion potential (ODP) and zero global warming potential, which means there are no risks using water as refrigerant in the future. The second main advantage of using water as refrigerant is because it's be a green energy: it can be obtained for free and readily available; it also has no disposal problem; what's more the most important characteristics is it has a potential to save energy about 20% to 30% than conventional refrigerants [15].

However, compressing water vapor as refrigerant imposes specific challenges for the compressor designer. Fig.2-1 illustrates in comparison to the traditional refrigerant R134a, that a R718 compressor needs to compress under vacuum environment and vacuum pressure varies between 900Pa and 1,800Pa; such a low pressure thus lower down density and produce a huge volume flow rate for compressors to handle [3]. In addition, pressure ratio for water vapor as refrigerant has to reach about five which is about two or three times higher than conventional ones [15]. To achieve such as high performance, it would be a big challenge for volume displacement compressors such as scroll compressors and turbo compressors are good candidates for the task.

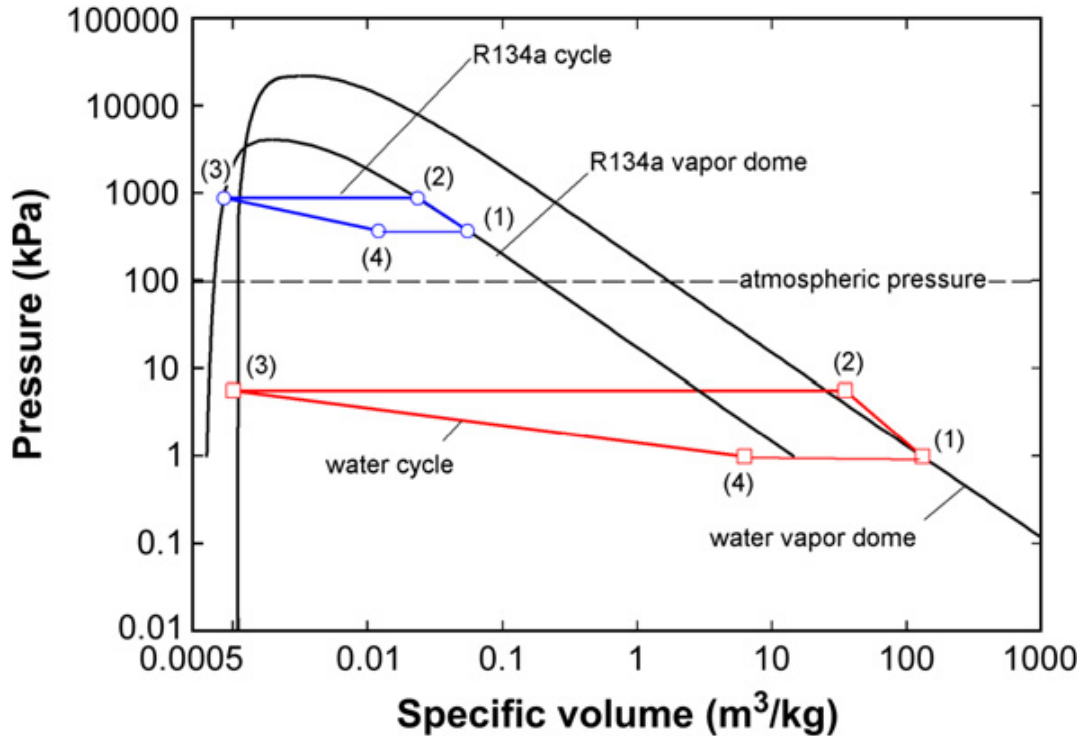


Figure 2-1 Pressure-specific volume diagrams of ideal water and R- 134a vapor compression refrigeration cycles [3]

2.2 Cycle Modification

An air conditioning system employing water as refrigerant can have the following two types of system configuration and these are hence presented:

A chiller employing water as refrigerant conceptualized at Michigan State University is shown in Fig.2-2. From the evaporator, chilled water at 6°C is supplied to the air handler cooling coil and returns at 12°C to the evaporator where it is expanded. As a result of the low pressure in the evaporator, the water flashes into vapor. The water vapor is compressed by a multi-stage turbo compressor to the condenser pressure. Between stages, cooling water from the evaporator is injected for flash cooling. In the condenser, the water vapor condenses either with direct mixing with cooling water or by indirect cooling. The condenser cooling water is continuously circulated through a cooling tower for heat rejection to the ambient.

In split air conditioning systems, the compressor feeds water vapor into an air cooled condenser placed in ambient conditions, where the vapor condenses while flowing inside tubes across which air is blown by a thermostatically controlled fan. The cooled water then enters the evaporator or indoor unit after the pressure is reduced by passing through an expansion valve. To complete the cycle, the water evaporates absorbing the room heat and flows due to the suction of the compressor. The differences in these two types of system configurations are given as follows: The first system circulates chilled water for providing sensible cooling. The chilled water system uses direct contact evaporation and condensation where almost no temperature difference is required for heat exchange. In the second system, the cooling effect is obtained due to phase change or evaporation of the refrigerant in the indoor unit.

2.2.1 Single Stage Vapor Compression Cycle

A vapor compression cycle with single stage compression and p-h diagram are given in Fig. 2-3.

The cooling capacity of an air conditioning system and the heat removal rate by the evaporator from the space to be cooled is given by:

$$\dot{Q}_{evap} = \dot{m}(h_1 - h_4) \quad (2-1)$$

The heat removed by the evaporator per unit mass of the refrigerant becomes:

$$q_{evap} = h_1 - h_4 \quad (2-2)$$

The specific work of compression assuming saturated vapor at the inlet for an ideal compression cycle is given by:

$$W_{c,is} = h_{2is}(p_{cond}) - h_1(p_{evap}) \quad (2-3)$$

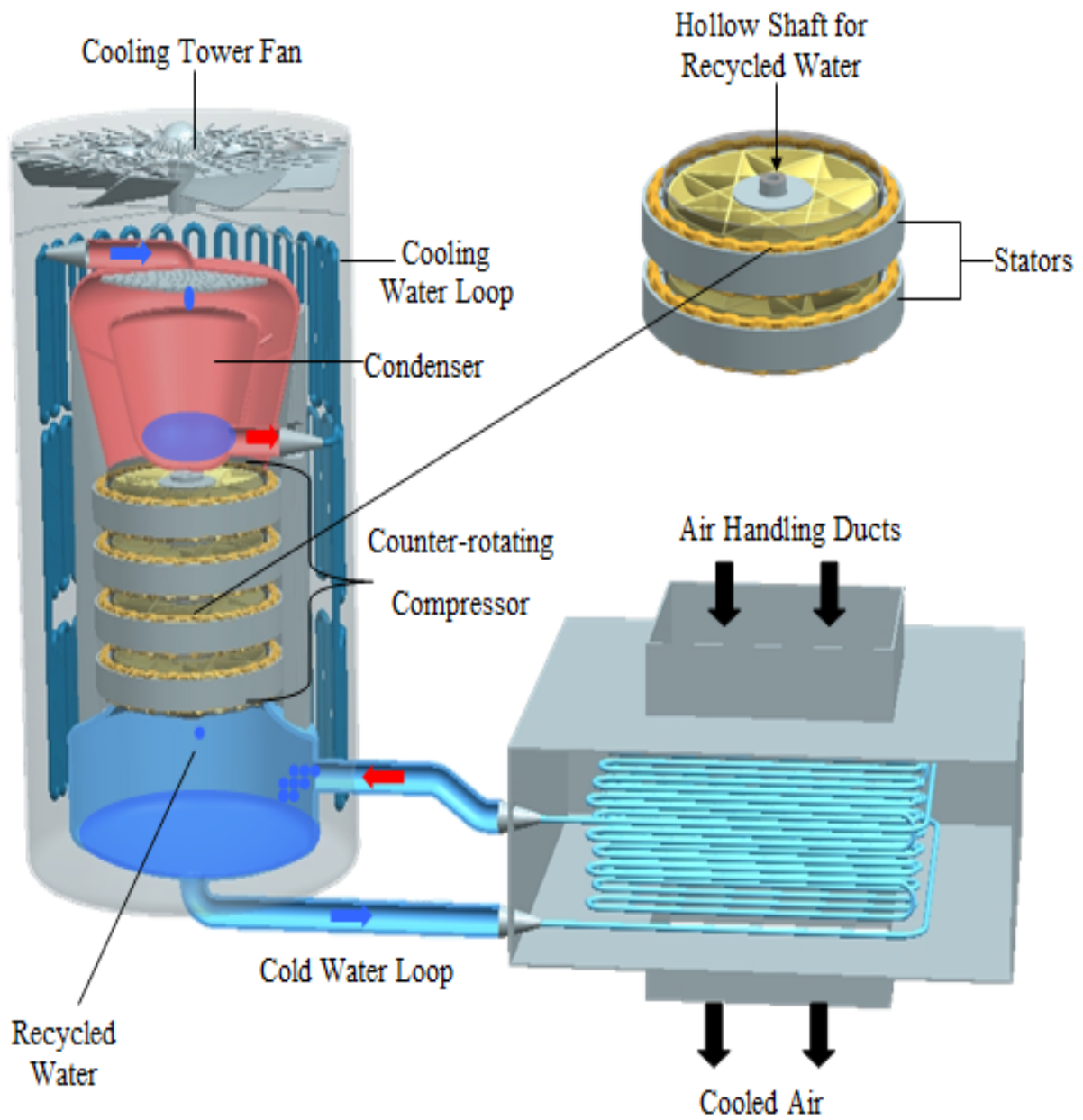


Figure 2-2 Turbo chiller employing R718 Refrigeration cycle

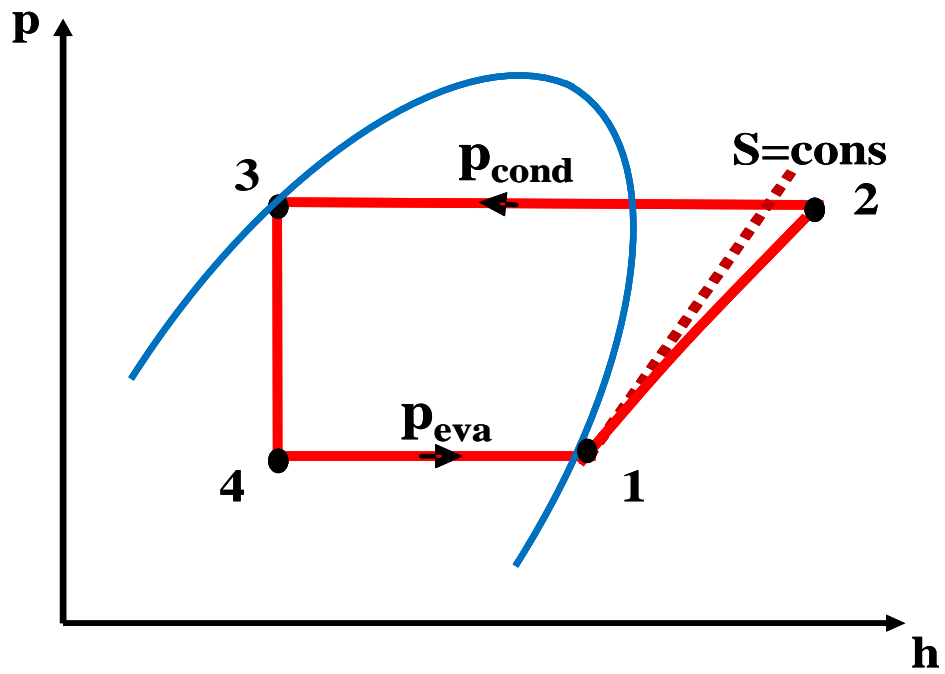
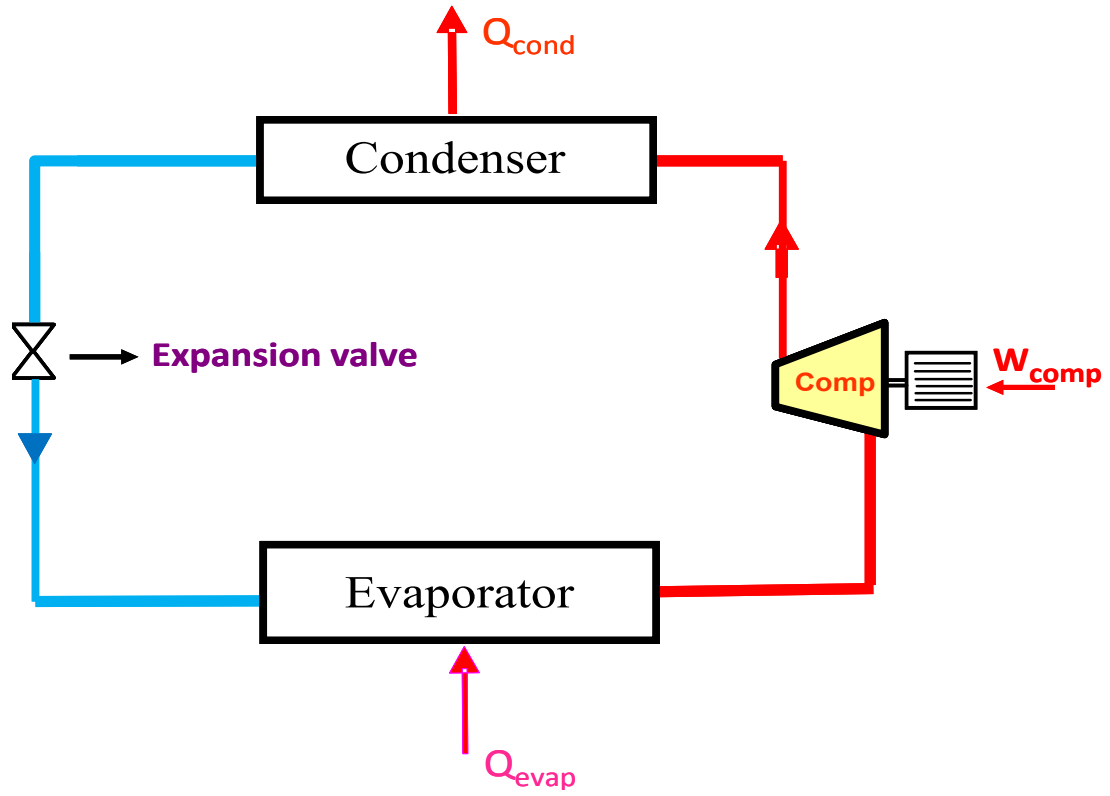


Figure 2-3 Vapor compression cycle with single stage compression

From the definition of isentropic efficiency, the enthalpy of the refrigerant at outlet of the compressor is obtained as

$$h_2(p_{cond}) = h_1 + \frac{h_{2,is} - h_1}{\eta_{is}} \quad (2-4)$$

The temperature and entropy of the vapor at the outlet of the compressor are determined by defining the state using the enthalpy and pressure. In the condenser, the superheated refrigerant vapor condenses to saturated liquid and might be subcooled. Hence, the heat that is to be rejected by the condenser per unit mass of the refrigerant assuming saturated liquid at outlet is

$$q_{cond} = h_2 - h_3 \quad (2-5)$$

The saturated liquid from condenser expands to the evaporator pressure and enters the evaporator as a mixture of vapor and liquid. This throttling process in the expansion valve occurs without change in enthalpy. As a result, the enthalpy at the inlet of the evaporator is given by

$$h_4 = h_3 \quad (2-6)$$

The specific work of compression is determined as:

$$W_c = \frac{h_{2,is} - h_1}{\eta_{is}} \quad (2-7)$$

The coefficient of performance (COP) is given as follows.

$$COP = \frac{q_{evap}}{W_c} \quad (2-8)$$

2.2.2 Multi Stage Vapor Compression Cycle

While the thermodynamic analysis of the system with a single stage compression is shown above, the multistage compression cycle in Fig. 2-4 requires following additional steps.

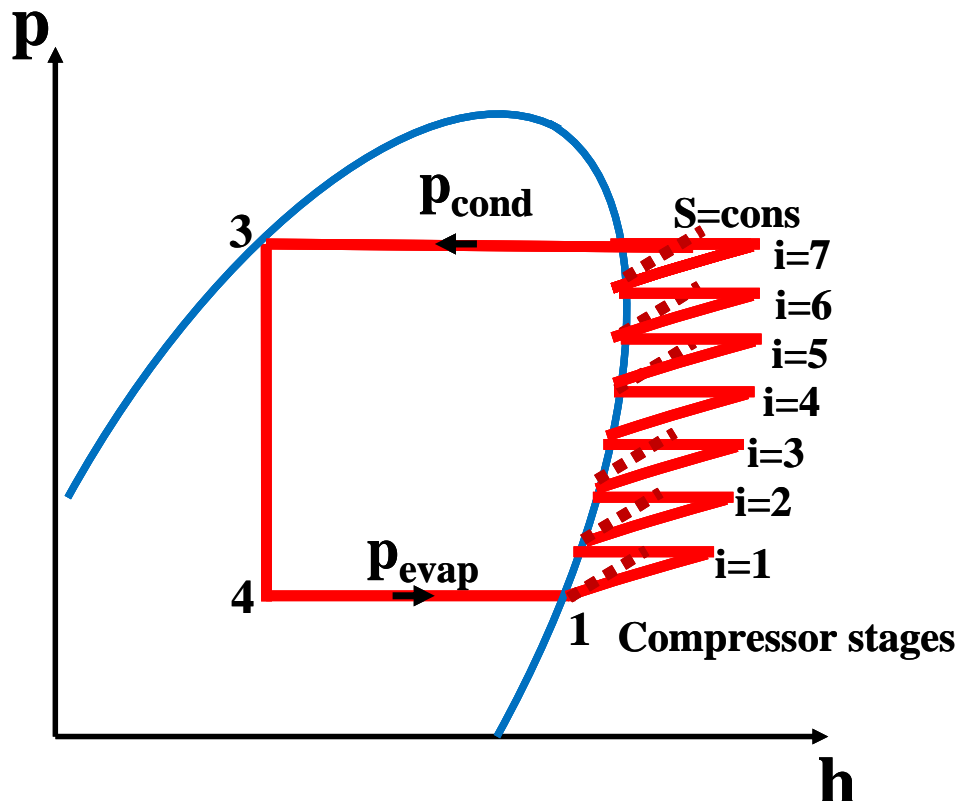
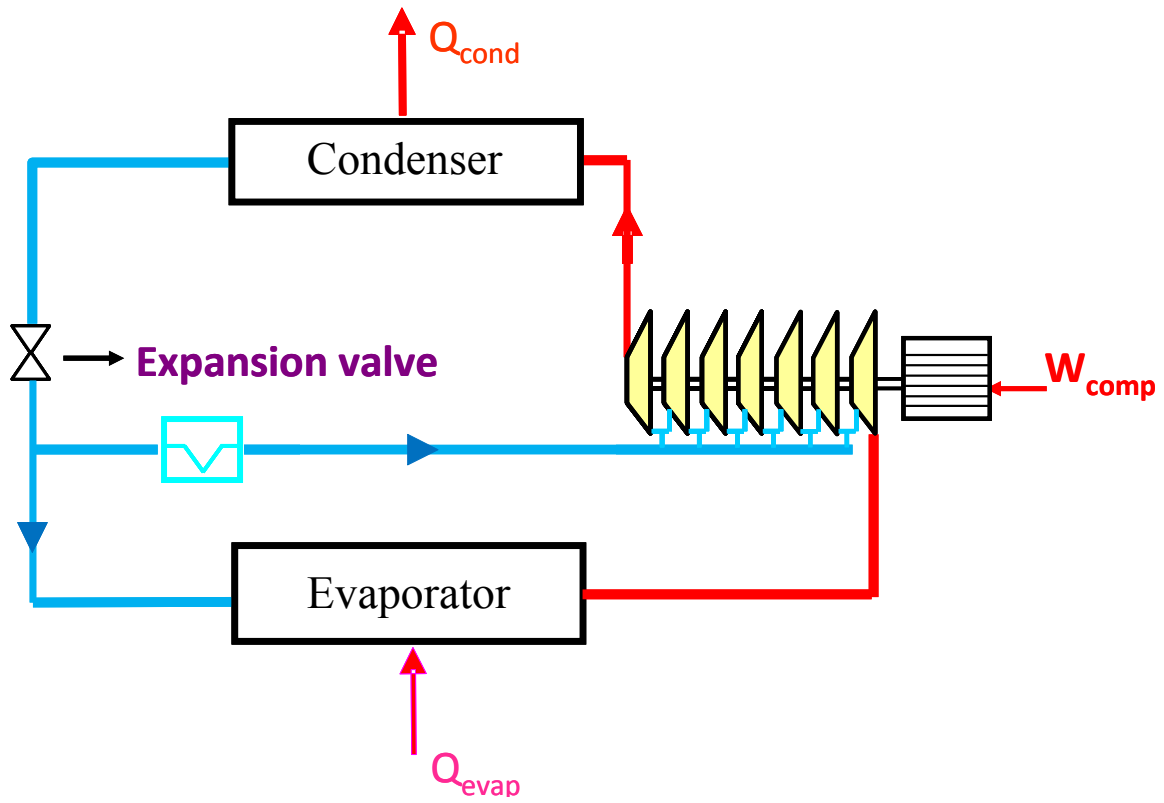


Figure 2-4 R 718 Vapor compression cycle with seven stage compression

The pressure ratio of each compression stage of the multi stage compression cycle is expressed in Eq.2-9 where ‘n’ is determined assuming the same pressure ratio in each stage. It can be adjusted according to compressor performance as well as size requirements. Different stages would, in practice, have different pressure ratios and efficiency requirements to compress in our system since intercooling would decrease specific speed considerably [16]. However, in the case of seven stages an average single stage pressure ratio needs to reach 1.288.

$$\pi_s = n \sqrt[n]{\frac{P_{cond}}{P_{evap}}} \quad (2-9)$$

The enthalpy and properties at the outlet of compressor are obtained stage by stage beginning from saturated vapor state at the outlet of the evaporator assuming isentropic compression efficiency. The vapor at the outlet of each compression stage is brought to saturated state by flash cooling (injecting water droplets) which is a special feature of using water as a refrigerant.

The enthalpy at inlet for the i^{th} stage of compression is determined as a function of the pressure assuming saturated vapor such that

$$h_{1i} = h(\pi_s^{i-1} \times p_{evap}, x = 1) \quad (2-10)$$

The enthalpy at the outlet of the i^{th} stage of compression is given by

$$h_{2i}(pr^i \times p_{evap}) = h_{1i} + \frac{h_{2i,is} - h_{1i}}{\eta_{is}} \quad (2-11)$$

The specific work of the i^{th} stage of compression of the flash intercooled multistage cycle is determined by considering the flashed water up to the i^{th} stage.

$$W_i = \frac{(1 + \sum_{j=1}^{i-1} mfw_j)(h_{2i,is} - h_{1i})}{\eta_{is}} \quad (2-12)$$

In the above equation, $\sum_{j=1}^{i-1} mfw_j$ indicates the mass of cooling water injected at end of each stage up to the i^{th} stage. The work of compression of each cycle is determined as the sum of the work of each stage.

$$W_c = \sum_{i=1}^n w_i \left(1 + \sum_{j=1}^{i-1} mfw_j \right) \quad (2-13)$$

The coefficient of performance can then be calculated using Eq. 2-8. Fig. 2-5 shows that the COP of the flash intercooled cycle for R718 is significantly improved relative to the non-intercooled cycle using R134a refrigerant. The degree of improvement diminishes with the number of compression stages but a large increase is evident especially if stage number is more than two. If seven stages are selected to compress water vapor, COP will be increased around 30% comparing with single stage compressing R134a as refrigerant. However, as it is discussed by Lachner [3] that the main drawback of the flash intercooled cycle is that the mass flow rate passing through subsequent compressor stages increases, it will easily shift compressor's working conditions off design points thus resulting in lower pressure ratio and efficiency. If the amount of mass flow is too much, the turbo compressor would also reach choke limit easily which means the mass flow cannot further increase; if the first stage's mass flow rate is reduced too much to prevent choke condition in latter stages, the flow will separate from the vanes and surge occurs. A surge means that the compressor pressure rise lapses, causing flow fluctuations and possibly damaging the compressor. Both choke and surge conditions should be highly regarded and considered when designing a turbo impeller, especially in refrigeration where flash intercooling is used.

To predict the mass of water needed to be sprayed for the cooling of the compressor's superheated temperature, calculations were conducted. Given that isentropic efficiency for the

whole stage can reach 70% and polytropic compression efficiency for each stage (assuming seven stages) is thus 71%. Polytropic efficiency will be used for performance measure at the outlet of each stage, which ensures that the overall performance of the compression process was not influenced by the number of compression stages [17]. Operating conditions for the analysis can be referred to in Table 2-1. Assuming liquid water has been fully evaporated into saturated vapor and static pressure does not change during the evaporation process, temperature and percentage of water amount to spray at each stage's outlet is shown in Fig. 2-6. In case of seven stages, mass flow rate at the last stage's inlet will increase for about 10% which will impose challenges to subsequent rotating impellers. Temperature at the outlet is about 35°C and it is a bearable temperature to impeller blades from material science views.

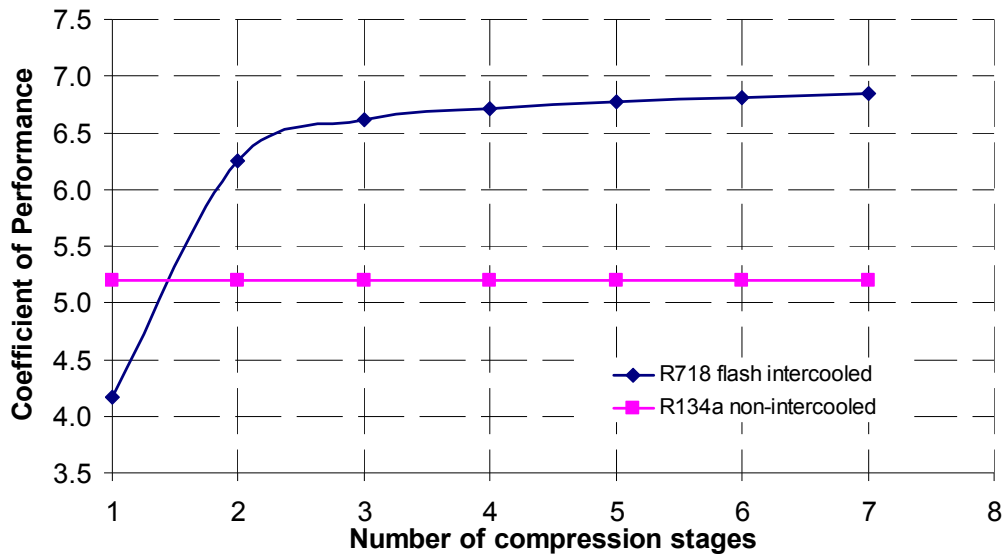


Figure 2-5 Comparison of COP between water and R134a

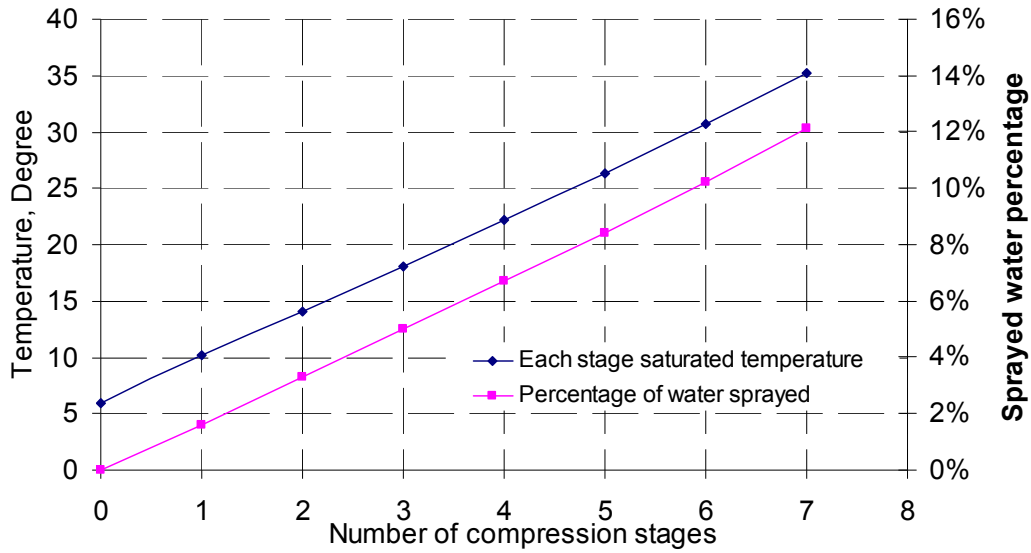


Figure 2-6 Temperature at each stage's outlet after intercooling and mass percentage of flash water sprayed

Table 2-1 Operating conditions used for analysis

Compressor inlet temperature	6.5°C
Evaporator pressure	0.97kPa
Evaporator temperature	35.2°C
Condenser pressure	5.7kPa
Pressure ratio	5.88
Sprayed liquid water temperature	7 °C
Refrigeration capacity (kW)	2500 (670ton)

2.3 Summary

A modified cycle with intercooling strategy for multi-stage compressor used to compress water vapor as refrigerant is studied and coefficient of performance is compared with conventional refrigerant R134a.

Comparing with conventional refrigerant R134a, multi-stage compressor with flash intercooling is able to improve COP by at least 30%. The use of flash intercooler delivers cooler flow to the second stage inlet with a higher pressure ratio and increases the isentropic efficiency. However, pressure ratio to single compressor stage on the average is required to be as high as 1.288 with 70% isentropic efficiency if seven stages were used.

CHAPTER 3 Manufacturing and Mechanical Characterization of Woven Wheel

3.1 Manufacturing of Composite Impeller

3.1.1 Description of Facility

The facility to manufacture the composite impeller is similar to one used for traditional filament winding, which is basically centered around four core pieces of equipment:

- i) A PC with CNC controlling software
- ii) The winding device (4-axis CNC machine)
- iii) The computer-controlled, custom-designed epoxy syringe system
- iv) The fiber tensioning control system

The CNC machine is the base of the entire system; the other subcomponents are integrated on top of it. The facility layout is designed to fit into a limited workspace of approximately 1m by 1m with the ability to weave a maximum 0.15m diameter impeller. Referring to Fig. 3-1, the spool are mounted with a tensioning unit; together with the force added on the fiber, this provides tension before and after the fiber passes through the epoxy static mixer tip. The fiber tensioning unit consists of a DC motor controlled through the computer, which provides constant torque to the fiber by counter rotating from its feeding direction. Fiber from the spool then passes onto the mandrel motor. From start to finish at the rotating mandrel, there are no significant turning angles for the fiber, making sure the added force from the motor is approximately equal to the constant tension added on the fiber during the winding process.

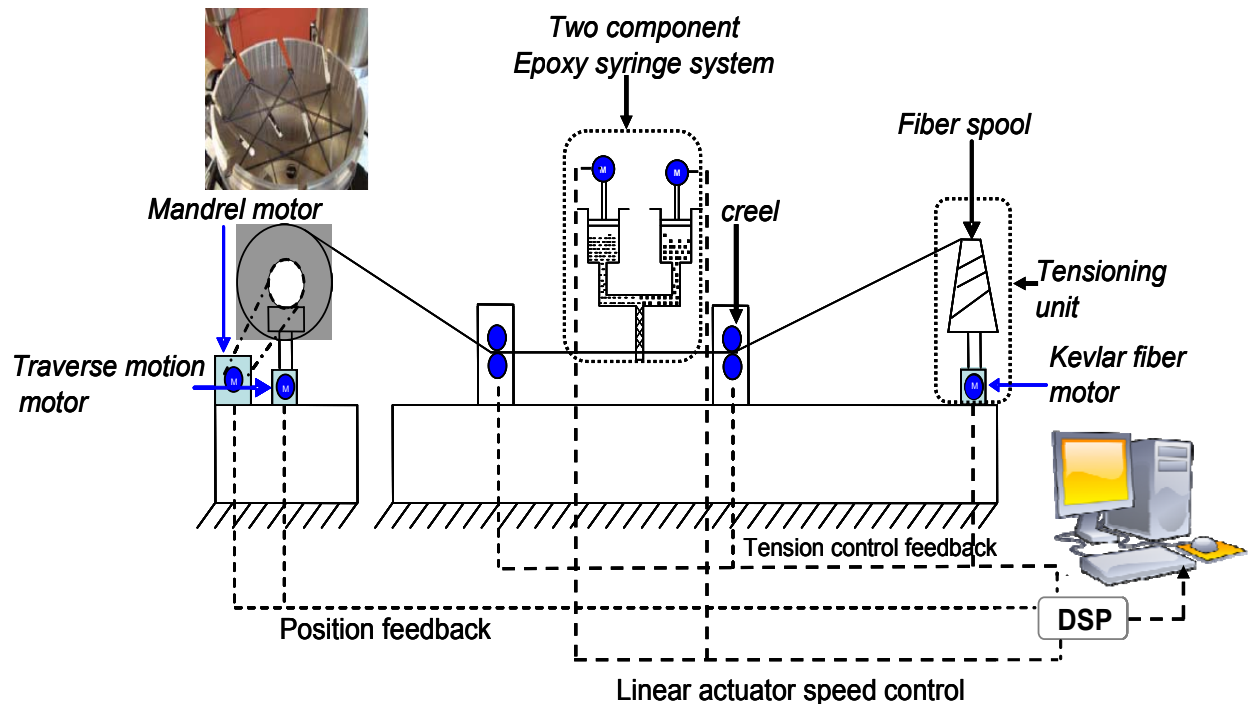


Figure 3-1 Layout of filament winding facility

In the figure, the two component epoxy syringe system plays the role of the resin bath in traditional filament winding machines. The disadvantage of traditional resin bath is the curing time relentlessly passes by while filament winding is performed, meaning that different sections of the fiber will encounter the bath at different curing conditions resulting in inhomogeneous final properties. Thus, in place of the traditional resin bath, a custom design two component syringe system is designed to mix resin and hardener in small batches, overcoming this problem and producing a woven wheel with homogeneous properties. During the winding process, when the mixed epoxy at the tip of syringe system is nears depletion, the computer controlled linear actuators push the syringes to inject the desired amount ($\sim 0.1\text{ml}$) into the static mixer at the tip. By using this approach, the passing fiber is always impregnated with freshly mixed epoxy, ensuring the quality of the woven composite structure.

3.1.2 Material Selection

As reinforcement for the composite structure, there are several choices listed in Table 3-1, with steel wire being the cheapest choice among the four. However, the specific strength may not reach the requirement of this research, as this property is the main design issue relative to centrifugal force. The chosen Kevlar29 sewing fiber from DuPont was selected considering from its low cost mainly and relative high modulus properties (tensile modulus $E=70.5\text{GPa}$, transverse modulus 7GPa , Poisson's ratio 0.33).

Table 3-1 Strength properties for some typical materials [18]

Material	Ultimate strength (MN/m ²)	Specific strength (KJ/kg)
Steel wires(DP.38)	3000	380
E-glass fiber	3500	1400
Carbon fiber	2800	1400
Kevlar 29/49 fiber	2700	1700

For the epoxy matrix, a two component resin, SC-15, made by Applied Poleramic Inc. is used. SC-15 was chosen for its low viscosity (300cP during mixing) and resulting low shear force while the fiber is being fed through the tip of static mixer in the epoxy syringe system. Another benefit is that low viscosity resin is more likely to permeate the fiber bundle providing better saturation.

Low epoxy viscosity also reduces the amount of excess epoxy adhered to the passing fiber, in turn lowering the amount of surplus resin in the final part and resin waste. The woven matrix does not require special post-winding treatment and can be cured at room temperature within 24 hours, all while still being able to maintain acceptable mechanical properties: tensile modulus $E=26.2\text{GPa}$, transverse modulus 2.69GPa Poisson's ratio of 0.35.

3.1.3 Design and Manufacturing Process

The slotted mandrel made from aluminum tubing is milled using the CNC machine. As per the requirement of different impeller designs of blade angles and patterns, the mandrel's shape differs in terms of the number of slots and shape of those slot curves. The number of slots determines the number of blade's to be woven and the shape of radial or elliptical curve contains the information for impeller inlet and outlet angle which is important for turbo-impeller's design. One example of 8-slot curved mandrel is shown in Fig. 3-2. Due to the fiber's movements during the weaving process around and across the mandrel, the winding patterns are different. Different wheel patterns, such as a traditional axial impeller which has blades cross the center, have been discussed by previous researchers [19].

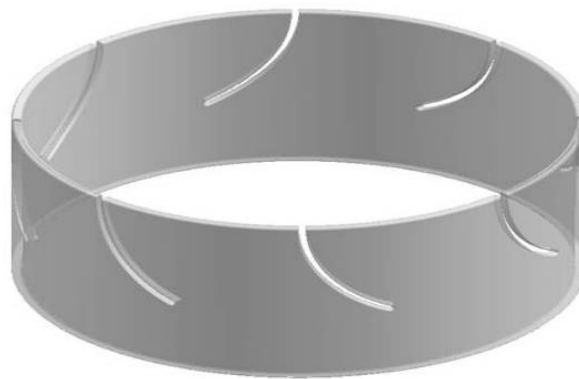


Figure 3-2 Mandrel picture of an 8-slot pattern

As the basis of the entire system, the CNC machine operates via computer control within the confines of four axes: rotation, traversing carriage, longitudinal movement, and height

adjustment. With the help of these movements, the winding path to create the one basic layer of the desired pattern can be completed; this is also visualized below in Fig. 3-3 (left). The computer-generated impeller model created with the chosen pattern is observed in Fig. 3-3 (center) and an actual filament woven impeller based on this pattern is shown on the Fig. 3-3 (right). In order to use the filament winding process automatically, the wheel's pattern can be generated offline using specialized CAD software and by converting into code, the pattern can be recognized by the CNC machine; thus the machine is highly automated and all input for the winding of impeller wheels can be done from the easy-to-use computer user panel.

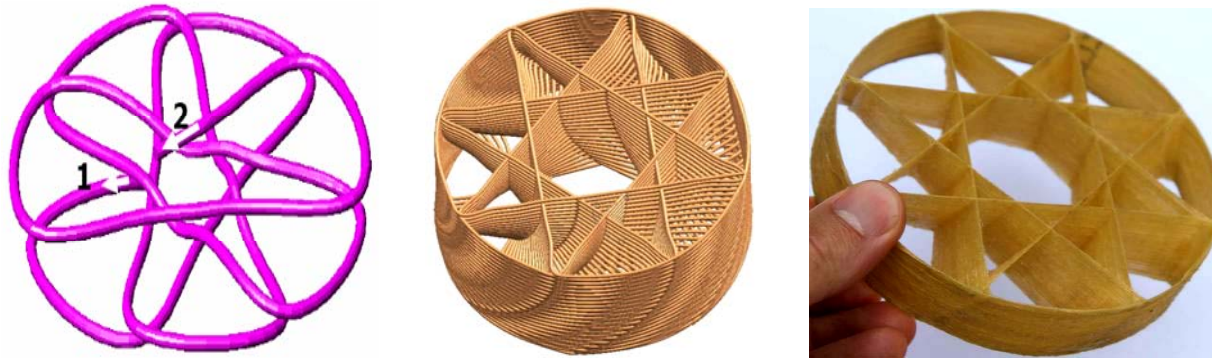


Figure 3-3 One complete layer for endless fiber winding (left) Computer model wound with single endless fibers (center) Filament wound composite impeller (right)

During the manufacturing process, the wheel was wound at a tension of about 1N, regulated through the DC motor controller by adjusting the motor torque given the spool radius. Studies show that increasing winding tension would raise the fiber volume fraction slightly and thus may have a large effect on strength [20]. However, tension in this approach is limited as to avoid damaging the Kevlar fiber which results in a lower fiber volume fraction than composite structures manufactured through conventional approaches. This in turn yields slightly lower specific weight for the structure, which might be beneficial in return.

The filament wound composite wheels were cured at room temperature overnight and were kept rotating during the entire curing process to prevent dripping and sagging. The cured composite impeller was then separated from the mandrel by cutting off the slots. The resulting wheels were measured and found to have an average internal diameter of 130.3mm and an average external diameter equal to 131.2mm, which included the external resin rich layer outside of the laminate layer.

When integrated with the filament wound impeller, the mandrel itself can be used as a rotating motor. One finished woven impeller integrated with an aluminum mandrel is shown in Fig.3-4 left with a demonstration in the motor rotating at 10,000RPM on the right.

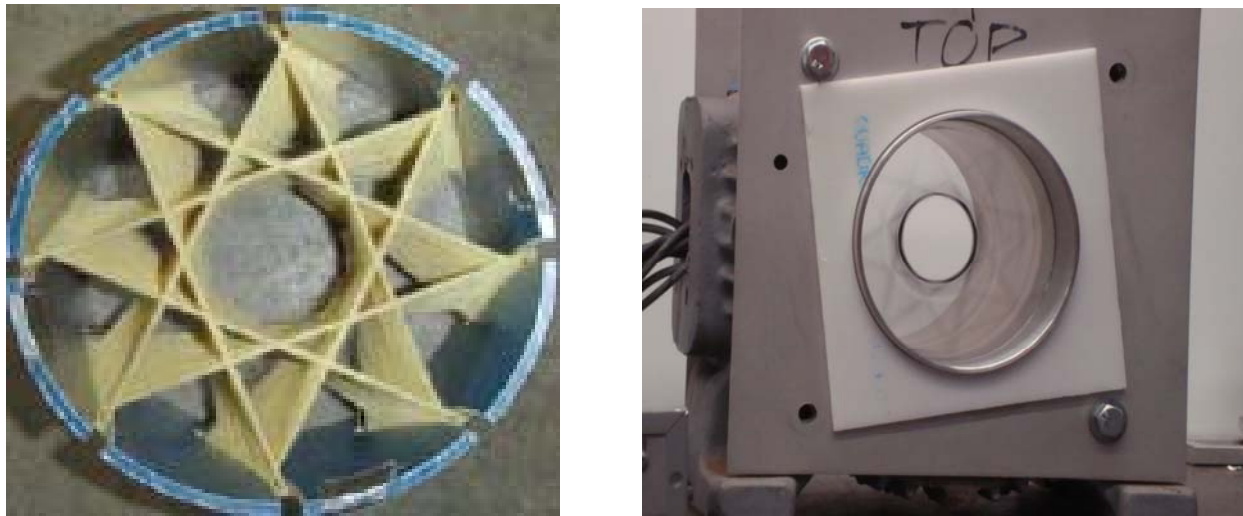


Figure 3-4 Composite impeller wheel integrated with mandrel (left) Demonstrate with frequency inverter drive @10,000RPM (right)

3.2 Mechanical Characterization

3.2.1 Determination of Composite Density and Volume Fraction Measurement

Considering the blade cross over each other, a batch of 14 single blades was prepared using the same method and materials as described for characterization purpose. During the winding, due to the applied tow tension from Kevlar fiber motor, excess resin were squeezed out and they

are able to diffuse through the fiber bed resulting in the resin rich outside layer in the whole manufacturing process. They were not removed from the surface of the wet part after winding as it is often considered a protective layer, which is supposed to benefit the blade. This excess resin also increases surface smoothness, which is useful to reduce Reynolds's number's effect to compression efficiency while compressing water vapor refrigerant.

The measurements of specific gravities and densities taken for the sample resin matrix and composite blades were conducted using the displacement and submersion technique in distilled water according to ASTM D792 [21].

Before and after manufacturing, weight difference of each constituent was measured. Knowing the weight of each section and the densities of the constituents, an average fiber/matrix volume fraction was determined for each manufactured composite impeller. Hence, the void fraction was obtained.

Based on the above method, the mean volume fraction of reinforcement was found to be 29.3% with a standard deviation of 1%. Similarly the mean volume fraction of voids was 1.2% with a standard deviation of 0.3%. This is a relatively low fiber fraction ratio compared with normal composite materials. This may be due in part to the fact that there is only one composite layer, where excessive resin layer has higher relative influence on the overall epoxy volume fraction than the case of normal multiple-layer laminated composite materials; at the same time, when the fiber is laid up over the previous layer; considering that a strong compacting force might damage the fiber, the compacting force is not too strong to push neighboring fibers close enough and it resulted excessive epoxy filled between them and formed a low fiber volume fraction.

3.2.2 Specimen Blade Theoretical Properties

The theoretical mechanical properties of the individual specimen blade were determined in order to provide a comparison with the experimental result which will be given in a later section. The ply properties E_1 and ν_{12} in the material principal directions were derived from the micromechanics model in Eq (1) and (2) [22]. Considering low fiber volume fraction in this study, equations (3) and (4) derived by Spencer are used for a better accuracy in transverse and shear modulus [23].

These four elastic modules are necessary for future finite element analyses to determine the stresses and strains in the wheel. The results of finite element analysis will also be compared with the ultimate strengths to determine if the wheel will safely withstand the load.

$$E_1 = E_f V_f + E_m V_m \quad (3-1)$$

$$\nu_{12} = \nu_f V_f + \nu_m V_m \quad (3-2)$$

$$\frac{M_c}{M_E} = \frac{\Gamma - 1}{\Gamma} + \frac{1}{k} \left[\frac{\pi}{2} + \frac{2\Gamma}{\sqrt{\Gamma^2 - k^2}} \tan^{-1} \sqrt{\frac{\Gamma + k}{\Gamma - k}} \right], \quad (3-3)$$

$$\text{where } M_c = E_2, k = 1 - \frac{E_m}{E_f}; \quad M_c = G_{12}, k = 1 - \frac{G_m}{G_{12}}$$

$$\Gamma = \frac{1}{\sqrt{V_f (1.1V_f^2 - 2.1V_f + 2.2)}} \quad (3-4)$$

3.2.3 Effective Specimen Blade Thickness

To get basic information about the thickness of the specimen blade, there are several methods available. Banerjee et al.[24] mentioned complex models based on the measurement, but an analytical determination of the composite specimen thickness is preferred for two reasons:

- i) It is not easy to obtain the distance using caliper type devices (the resin cover falsifies any measurements);
- ii) It is often necessary to section the specimen blade and analyze its cross-section using optical means (e.g. micrographs); this is generally time-consuming, especially if a large number of samples need to be investigated.

Thus an analytical method becomes necessary to calculate the thickness. Together with basic geometrical information, the thickness of the effective specimen blade can be approximated from fiber volume fraction.

As the total area in cross-section can be given by the sum of total fiber cross sectional areas (one single layer) and resin area, the average thickness of the blade (t) is calculated by the number of fiber thread (N), fiber diameter (d), blade width (w), and fiber volume fraction (V_f) as in Eq (5). It is assumed that the properties through the blade thickness are constant, and the volume fraction of fiber is the same as that determined from calculation. Thus, the mean thickness is 0.78mm.

$$t = \frac{N \times \pi d^2}{4 \times w \times V_f} \quad (3-5)$$

During filament winding, there are some inherent crossover points that not only lead to fiber path undulation but also cause large variations in local volume fraction. Overlap of neighboring fibers may also cause irregular laminate thickness that is not considered here.

To verify the proposed method, the effective specimen thickness was measured at several points around both the blades and circumference (angle increments of 10°) using an optical microscope. Based on the measurements, it was found that the calculations produce a slightly bigger thickness value than was experimentally measured, with a relative error of less than 10%.

This error might come from the accuracy of model proposed, where uniform properties are assumed throughout specimen thickness direction.

3.2.4 Experimental Procedures for the Determination of Mechanical Properties

Considering that the main purpose of this research is to weave light weight composite impellers which are able to endure high centrifugal forces under high rpm, it is important to evaluate the maximum tensile stress of the specimen blade in order to determine the whole impeller structure's mechanical properties. Higher moduli are also desired in that they ensure only small displacements occur, thereby reducing the dynamic problems originated by asymmetrical deformations and simplifying some problems related to the connection of the composite impeller to the shaft for certain patterns.

Blade specimens were fitted with aluminum end tabs resulting in a 92mm gauge section to be used with an Instron 5567 testing device; the picture of measurement setup is shown in Fig. 3-5. Because the grips on this machine are on swivel heads, bending was considered to be negligible, thus only one strain gage rosette was applied to the specimens. Temperature was also neglected since the room temperature was held constant and no significant direct contact with the gages was made that could affect their temperature during testing.



Figure 3-5 Photograph of static strain-stress measurement

On the strain gauge rosette, one perpendicular grid was aligned with the axial direction and transverse direction of the blade and bonded at the mid-point of the specimen. By using the specimen's average thickness, and data acquired from the previous section, force on the head was converted into stress. As force is only provided in the x-direction, tensile stress σ_y and shear stress τ_{xy} are set to equal zero. Young's modulus E_1 and Poisson ratio ν_{12} in longitudinal direction can be computed through Eq (3-6). To obtain the shear modulus, a second specimen with the material axis offset from the specimen axis (x-y) by 10° (θ) is used and a detailed discussion towards strain-gage orientation angle for shear modulus can be referred to the work done by Tuttle [25]. Stress and strain values in principal material direction (axis 1-2) were determined through Eq (3-7) and Eq (3-8). Together with the calculated stresses σ_2 , τ_{12} strain ε_2 and γ_{12} , moduli E_2 and G_{12} were then obtained with Eq (3-9) and (3-10).

$$E_1 = \frac{\sigma_1}{\varepsilon_1}; \nu_{12} = \frac{-\varepsilon_2 E_1}{\sigma_1} \quad (3-6)$$

$$\begin{bmatrix} \sigma_1 \\ \sigma_2 \\ \tau_{12} \end{bmatrix} = [T] \times \begin{bmatrix} \sigma_x \\ \sigma_y \\ \tau_{xy} \end{bmatrix}, \quad (3-7)$$

$$\begin{bmatrix} \varepsilon_1 \\ \varepsilon_2 \\ \gamma_{12}/2 \end{bmatrix} = [T] \times \begin{bmatrix} \varepsilon_x \\ \varepsilon_y \\ \gamma_{xy}/2 \end{bmatrix} \quad (3-8)$$

$$E_2 = \frac{\sigma_2}{\varepsilon_2} - \nu_{21} \frac{\sigma_1}{\varepsilon_2} = \frac{\sigma_2 E_1}{E_1 \varepsilon_2 + \nu_{12} \sigma_1} \quad (3-9)$$

$$G_{12} = \frac{\tau_{12}}{\gamma_{12}} \quad (3-10)$$

$$[T] = \begin{bmatrix} \cos^2 \theta & \sin^2 \theta & 2\sin\theta\cos\theta \\ \sin^2 \theta & \cos^2 \theta & -2\sin\theta\cos\theta \\ -\sin\theta\cos\theta & \sin\theta\cos\theta & \cos^2 \theta - \sin^2 \theta \end{bmatrix} \quad (3-11)$$

3.2.5 Specimen Blade Strain and Stress Characteristic

The laminate properties provided in Table 3-2 were calculated based on the ply properties found using the micromechanical approach that was mentioned in the previous section. Again, none of the excess resin-rich layer was removed from the outside surface of the filament wound impeller. Theoretically this resin layer is supposed to distribute evenly along with fiber. Due to the tension added during the winding process, this epoxy layer is squeezed out and forms an additional pure epoxy layer outside of the specimen, which consequently results in a decrease in the experimental results.

Table 3-2 Kevlar fiber reinforced epoxy laminate properties from micromechanical theory and experimental results

Property	Theoretical Value	Experimental value
Tensile modulus	39.19GPa	31.10GPa
Shear modulus	11.20GPa	8.50GPa
Poisson's ratio	0.34	0.31
Traverse modulus	32.25GPa	20.45GPa
Density	1.19g/cm ³	0.98g/cm ³
Maximum tensile stress	---	192 MPa

When the fiber volume ratio is far less than that of the resin, the resin overall contributes more to the mechanical properties in both the tensile and transverse directions. It explains why the values for tensile modulus and transverse modulus do not substantially differ. For a low fiber fraction in this research, micromechanical strength of material approach is a good approach to predict composite material's properties rather than measuring the property experimentally when impeller wheel's geometrical properties vary in patterns and diameters.

3.3 Discussion

3.3.1 Manufacturing Cost

Depending on the filament winding motor speed, the time required for the whole process varies from half an hour to one hour. By comparing with traditional steel impeller, resin transfer molding (RTM) as well as thermoplastic composite based method [26] in Fig. 3-6, the automation process enables manufacturing fast and inexpensive for composite impeller with desired properties. The benefits mainly come from the utilization of mature filament winding technology, which makes automatic manufacturing of a composite structure into reality. The weaving process saves time over the conventional approach by omitting the cumbersome blade welding process and the alignment of layers by hands. Additionally, since the setup of the whole system is based on commercially available CNC machines, development cost is not excessive. Clearly, this novel technology is promising for mass manufacturing of composite impeller.

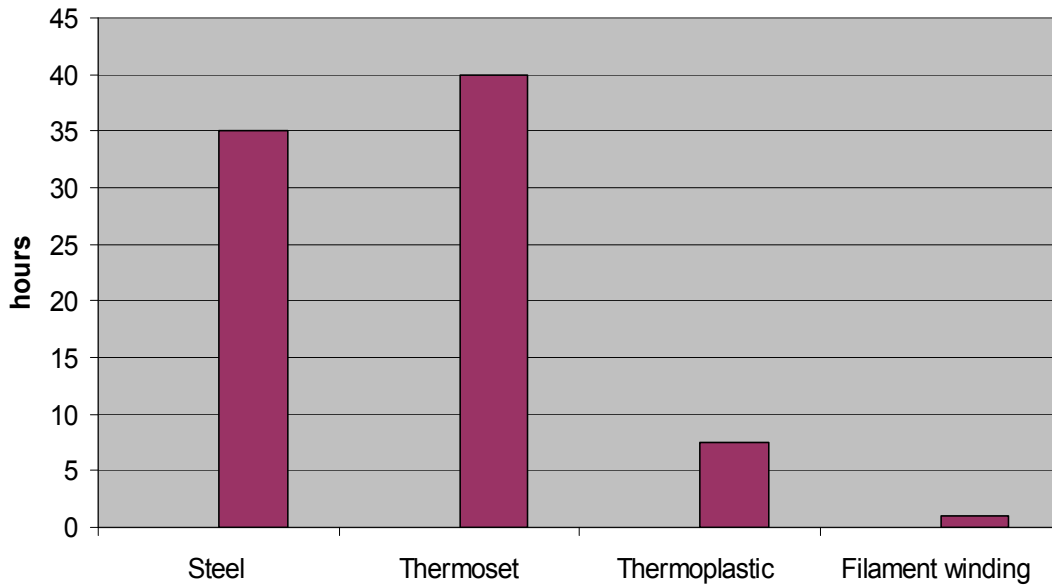


Figure 3-6 Comparison of manufacturing hours for steel, thermoset and thermoplastic-composite versions of impeller

3.3.2 Mechanical Properties

Modern impeller tip speeds of about 500m/s are close to material limits and manufacturing ability. Of the various parameters that limit the tip speed, material density is key as it directly influences the centrifugal force [27]. Density obtained from experimental approach in Table 3-2 is less than that calculated from micromechanical method; it can be proved that void fraction of about 1.2% decreases composite properties for about 12% in this matrix dominated structure [28]. However, relative similarities between experimental and analytical properties illustrate that constituents in the composite structure manufactured in this approach are performing their own function, which shows that this approach is able to produce qualified composite.

A preliminary finite element analysis was done based on the properties obtained in Table 3-2. It was discovered that the composite impeller can reach a maximum tip speed of about 840m/s before structural failure occurs. Interested readers can find more details in reference [29].

3.3.3 Manufacturing Issues

Even though this novel manufacturing approach makes the utilization of a composite impeller to compress water vapor refrigerant promising, there are several challenges associated with manufacturing process. These challenges include having only one single fiber layer weaving the wheel instead of multiple layers in traditional filament winding technology as well as low compacting mechanism between fibers, which result in low moduli. A relative low modulus means a potential maximum stress failure risk in the transverse direction. However, this drawback may be overcome by using several fibers weaving together simultaneously to form a laminated structure, or using larger diameter fibers which may enable bigger compacting force possible for a higher fiber volume fraction.

In turbomachinery, a smooth blade surface of the impeller is essential to lower fluid friction losses thus higher compression efficiency. Even though excessive resin layer formed outside of the impeller benefit a smooth surface, yet it is not as smooth as those produced through traditional filament winding technology. In traditional filament winding technology, after the resin bath, the fiber goes to additional stage where excessive resin is removed and a smooth surface is then created. This novel manufacturing approach lacks this stage which might be the reason for a less ideal blade surface. A further improvement to this approach could be achieved through the addition of a similar stage to improve blade surface quality.

3.4 Summary

The use of water as a refrigerant (R718) in the refrigeration application shows promise in vapor compressor plants as water has distinct advantages over traditional refrigerants. However, some of the difficulties that arise during manufacturing low cost but high performance compressor impellers to compress this natural refrigerant still need to be addressed.


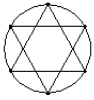
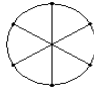

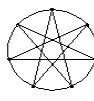
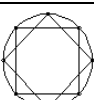

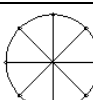
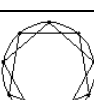
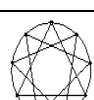
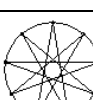
This chapter has illustrated that a novel manufacturing method similar to filament winding technology is able to manufacture composite impeller for compressing water-vapor refrigerant at a remarkable low cost. By comparing with other traditional composite manufacturing methods, this novel approach is highly competitive. To confirm manufactured impeller material properties, specimen blade's mechanical properties are measured through static strain stress experiments. The match between experimental data and calculation from micromechanical strength theory shows that this approach is able to manufacture the quality of composite impeller as desired. It is therefore concluded that the serial production cost and ultimate performance are no longer barriers to the refrigeration application of advanced composite materials.

CHAPTER 4 Pattern Aerodynamic Comparison

4.1 Investigated Impeller Geometries

As it is discussed in the last chapter that this filament winding similar technology is able to manufacture various impeller patterns, Table 4-1 summaries typical pattern shapes to weave.

Table 4-1 Typical winding patterns for endless fibers

Number of points in the mandrel	Shape -A	Shape -B	Shape -C
5		---	---
6			---
7			---
8			
9			

Two different initial rotor patterns 8B and 8C are selected for pattern aerodynamic comparison and its impeller geometries can be shown in Fig. 4-1 and Fig. 4-2 respectively. Aerodynamic comparison results will be seen as an approach to understand aerodynamic flow through these complex axial impellers. Different hub/tip ratios are also going to provide us a further understanding how to apply these novel impellers in a multi-stage figuration to compress water vapor as refrigerant. Table 4-2 gives all six cases to compare in next sections. To make comparison consistent, blade angle at shroud maintains the same when pattern and hub/tip ratio

change. It is therefore the main goal of this chapter is to investigate the feasibility of the various impeller designs accommodating different hub sizes. Further numerical simulations with more stringent convergent criteria shall be carried out before actually building the compressor and testing its performance and a better pattern can be selected.

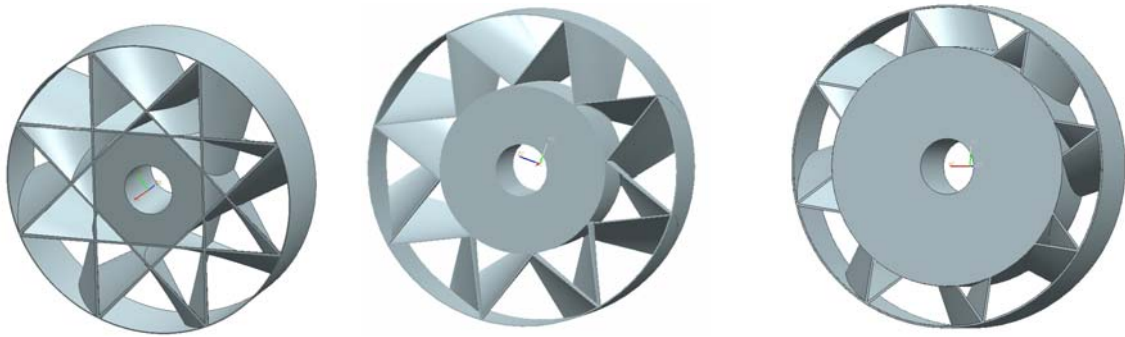


Figure 4-1 8B pattern rotor for different ratios: 0.43 (left), 0.54(middle) and 0.75(right)

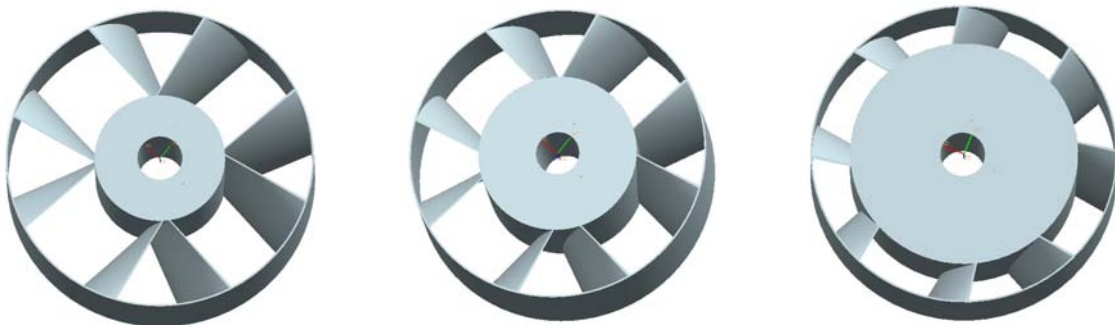


Figure 4-2 8C pattern rotor for different ratios: 0.43 (left), 0.54(middle) and 0.75(right)

Table 4-2 Six cases studied for the axial compressors

Case No	Rotor	Hub/Shroud radius ratio
1	8B	0.75
2	8B	0.54
3	8B	0.43
4	8C	0.75
5	8C	0.54
6	8C	0.43

4.2 Blade angle comparison

It is typically expected that the angle should change with the radius as the optimal angle's change in conventional axial impeller. Comparison of blade angles relative to tangential direction is shown in Fig.4-3. Due to geometrical restrictions the actual angles differ from optimal angle. It means that it may be expected that only on some specific radius the expected angle of attack is realized. At higher radius it is lower and for smaller radius is greater than expected. The differences depend on the diameter of the hub. For $r/R = 0.43$ and $r/R=0.54$ the difference can reach 15 degrees and at $r/R=0.75$ 10 degrees. The leading edge of the blade is not radial. It is oblique, generating additional radial components of the flow velocity. Typically, such blading does not exist in common axial compressors and the aerodynamic characteristics of the rotor can be expected to be different than commonly known.

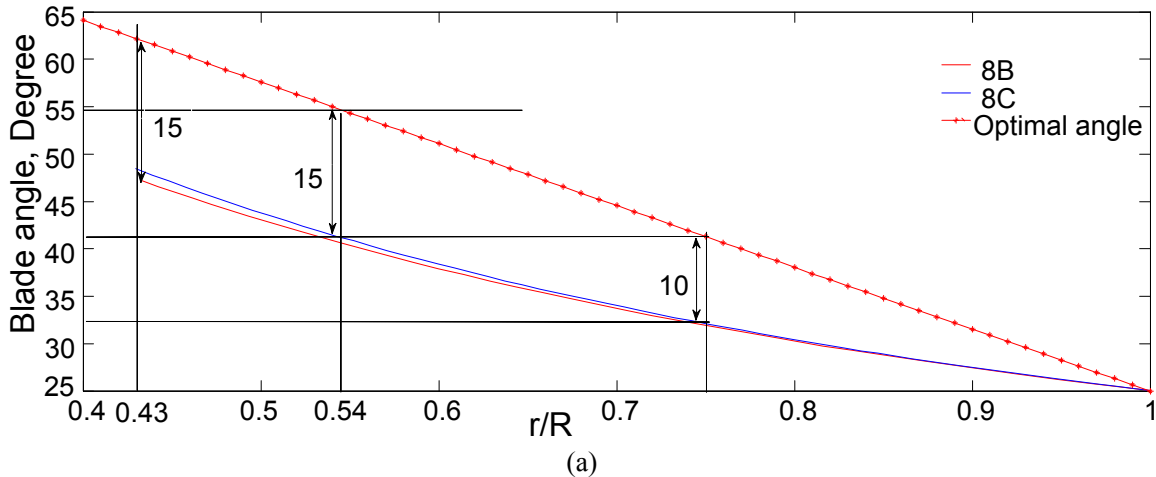


Figure 4-3 Blade angle distribution: leading edge (a) and trailing edge (b)

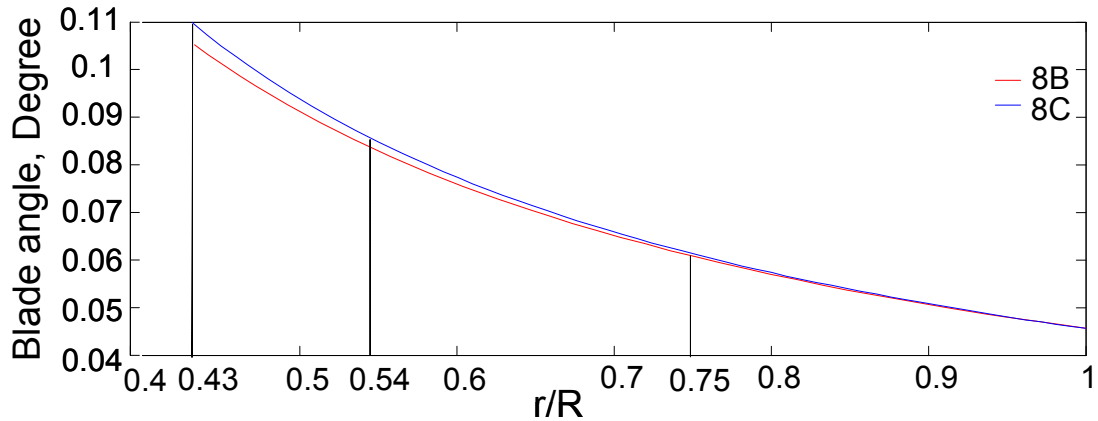


Figure 4-3 (cont'd)

4.3 Numerical Model Setup

4.3.1 Assumptions

Steady state conditions are simulated and water vapor is assumed to be ideal gas (compressible medium) for all of the simulations since a local Mach number can reach the value of one. Oscillations of the flow parameters with iterations indicate (in some of simulations) that the compressor is at an operating point close to stall at the left side of characteristic maps. Even though the surge point cannot be accurately predicted using steady state CFD, at least the simulation is consistent in terms of onset of stall. Right end of characteristic maps is defined as the maximum relative Mach number reaches one. Based on the same criteria, both the performance in terms of pressure ratio and efficiency and width of stable operating range of different cases can be compared consistently.

4.3.2 Conservation Equations

The domain where the mixture fluid flows through the wheel has been modeled at a reference frame and a rotary speed is given the same as impeller wheel's rotating rpm. FLUENT is able to solve this kind of rotating reference frame problem using either relative velocity or absolute velocity [30]. The mass and momentum conservation equations are given as follows:

$$\frac{\partial}{\partial x_i}(\rho u_i) = 0 \quad (4-1)$$

$$\frac{\partial}{\partial x_j}(\rho u_i u_j) = -\frac{\partial p}{\partial x_i} + \frac{\partial}{\partial x_j} \left[\mu \left(\frac{\partial u_i}{\partial x_j} + \frac{\partial u_j}{\partial x_i} - \frac{2}{3} \delta_{ij} \right) \right] + \frac{\partial}{\partial x_j} \left[\mu_t \left(\frac{\partial u_i}{\partial x_j} + \frac{\partial u_j}{\partial x_i} \right) - \frac{2}{3} \left(\rho k + \mu_t \frac{\partial u_l}{\partial x_l} \right) \delta_{ij} \right] \quad (4-2)$$

In order to model turbulent kinetic energy of κ and its dissipation rate ε , conservation equations are expressed as following:

$$\frac{\partial}{\partial t}(\rho k) + \frac{\partial}{\partial x_i}(\rho k u_i) = \frac{\partial}{\partial x_j} \left[\left(\mu + \frac{\mu_t}{\sigma_k} \right) \frac{\partial k}{\partial x_j} \right] + G_k - \rho \varepsilon - Y_M \quad (4-3)$$

$$\frac{\partial}{\partial t}(\rho \varepsilon) + \frac{\partial}{\partial x_i}(\rho \varepsilon u_i) = \frac{\partial}{\partial x_j} \left[\left(\mu + \frac{\mu_t}{\sigma_\varepsilon} \right) \frac{\partial \varepsilon}{\partial x_j} \right] + G_k C_{1\varepsilon} \frac{\varepsilon}{k} - \rho C_{2\varepsilon} \frac{\varepsilon^2}{k} \quad (4-4)$$

Values of σ_k σ_ε are setup as FLUENT default values, where turbulence kinetic energy generation from mean velocity gradients G_k and contribution of the fluctuating dilatation in compressible turbulence to the overall dissipation rate Y_M can be expressed as:

$$G_k = \left[\mu_t \left(\frac{\partial u_i}{\partial x_j} + \frac{\partial u_j}{\partial x_i} \right) - \frac{2}{3} \left(\rho k + \mu_t \frac{\partial u_l}{\partial x_l} \right) \delta_{ij} \right] \frac{\partial u_j}{\partial x_i} \quad (4-5)$$

$$Y_M = 2\rho\varepsilon \frac{k}{\gamma RT} \quad (4-6)$$

with turbulent viscosity μ_t

$$\mu_t = \rho C_\mu \frac{k^2}{\varepsilon} \quad (4-7)$$

where $C_{1\varepsilon}$ $C_{2\varepsilon}$ C_μ are set as default values of 1.44, 1.92 and 0.09 respectively.

The energy conservation equation is:

$$\frac{\partial}{\partial x_i} [u_i (\rho E + p)] = \frac{\partial}{\partial x_j} \left(k_{eff} \frac{\partial T}{\partial x_j} + u_i (\tau_{ij})_{eff} \right) \quad (4-8)$$

where viscous heating $(\tau_{ij})_{eff}$ is defined as:

$$(\tau_{ij})_{eff} = (\mu + \mu_t) \left(\frac{\partial u_i}{\partial x_j} + \frac{\partial u_j}{\partial x_i} - \frac{2}{3} \delta_{ij} \frac{\partial u_l}{\partial x_l} \right) \quad (4-9)$$

4.3.3 Boundary Conditions

For this compressible flow, inlet mass flow rate is set at the surface of front chamber with total temperature of 300K. At the inlet, turbulence level equal 10% and turbulent length scale equal 0.5 m are used. At the outlet, which is the surface of back chamber, static pressure is defined. Domains where fluid flows through the wheel are set as a reference frame model and they are rotating at the same RPM for all six cases. Interface boundary conditions are set for each coupled surface between impeller upstream and downstream sections. Near solid walls, the standard wall function is used. During all calculations the range of turbulence y^+ value between 31 and 290 was obtained, which is acceptable for the standard wall function 10. Blade wheels are treated as walls. All chamber walls are adiabatic.

4.3.4 Grid Generation

The total number of grid for each case and for all of computational domains is about one million. The 3D mesh of the flow channels is meshed automatically in GAMBIT in Tetrahedral /Hybrid elements. A grid dependency study was also carried out by locally refining the grids of the whole impeller. The total number of grid increases up to 50%, while less than 1% difference has been found in results. Such small difference in terms of pressure ratio and temperature can be considered negligible.

4.3.5 Model Parameter

For turbulence modeling, the standard κ - ϵ model without realizable modifications was employed for its robustness and lesser demand on computing resources compared to the other turbulence models available in FLUENT [31-33]. The second-order accurate upwind differencing for the convection terms of each governing equation is used to minimize the cross-stream numerical diffusion. The second order accuracy is also maintained for the viscous terms.

The pressure-velocity coupling is handled by the SIMPLE algorithm. The convergence criterion requires that the scaled residuals decrease to 10^{-3} for all of equations except energy equation to 10^{-6} . To achieve convergence criterion, under relaxation factor for pressure is about 0.4 to avoid the correction diverge.

4.4 Results and Discussion

4.4.1 Overall Performance Comparison at the Same Rotating Speed

The comparison of pressure ratio between different hub size designs for both patterns is given in Fig.4-3 and Fig.4-4. The compressor speeds and the numerical procedure were the same. The pressure ratio (Π_C) and isentropic efficiency (η_C) of the compressor are calculated based on the total pressures (P_{total}) and total temperatures (T_{total}) at both inlet and outlet of the compressors, as defined below:

$$\Pi_C = \frac{P_{total,outlet}}{P_{total,inlet}} \quad (4-10)$$

$$\eta_C = \frac{(\Pi_C)^{0.254} - 1}{\frac{T_{total,outlet}}{T_{total,inlet}} - 1} \quad (4-11)$$

It is thus total-to-total pressure ratio and efficiency. For temperature and pressure, mass averaged values are used at the outlet.

Table 4-3 Summary of performance for each case

Case No	Rotor	Hub/Shroud radius ratio	Peak Π_C	Peak η_C	Stable working range (kg/s)
1	8B	0.75	1.162	68%	0.45
2	8B	0.54	1.121	65%	0.75
3	8B	0.43	1.107	64%	0.95
4	8C	0.75	1.163	73%	0.30
5	8C	0.54	1.124	65%	0.70
6	8C	0.43	1.115	66%	0.80

As we can observe from Fig.4-4, 4-5 and summary in Table 4-3 that for pattern B the biggest hub has the narrowest stable operating range but the compression is evidently higher; for pattern C in Fig.4-5, pressure ratio performance is similar to pattern B: the bigger the hub, the better performance. The only difference between these two patterns lies in that efficiency for ratio of 0.54 and 0.43 are almost the same while ratio 0.54 has a little higher pressure ratio than 0.43. Since stators are the same for each comparison and similar pressure and efficiency losses are observed for different cases, thus its effect to stage difference between cases can be neglected. Around the phenomenon observed from these results, there are several main questions needed to explain, such as:

- 1) How bigger hub size enhances aerodynamic performance in both patterns?
- 2) How bigger hub size shifts characteristic maps to the left?
- 3) Which pattern would bring better aerodynamic performance when the hub size changes?

And what's the reason behind it?

- 4) How to optimize the best setting?

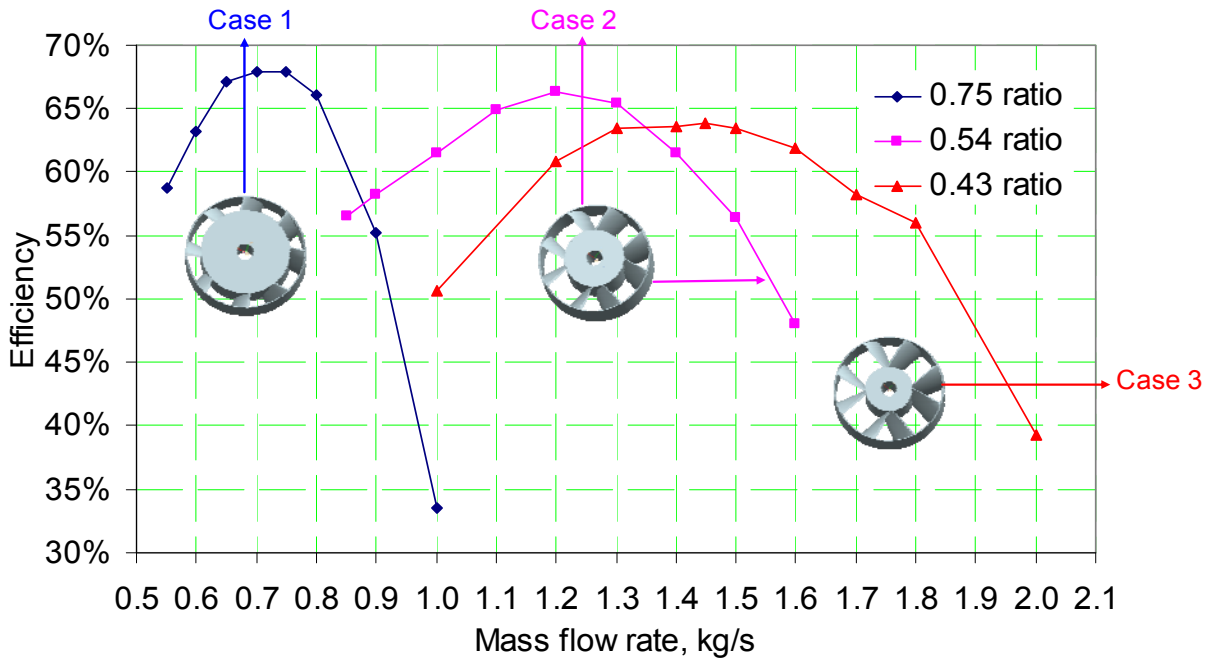
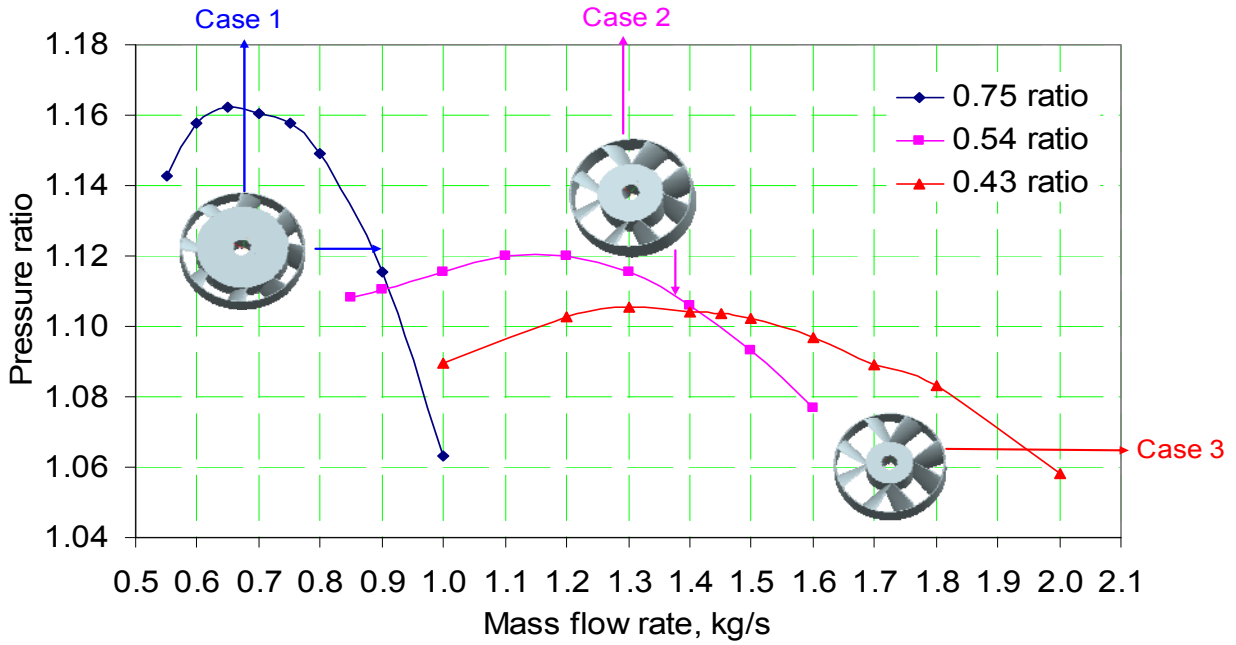


Figure 4-4 Comparison of performance between different hub sizes for pattern 8C

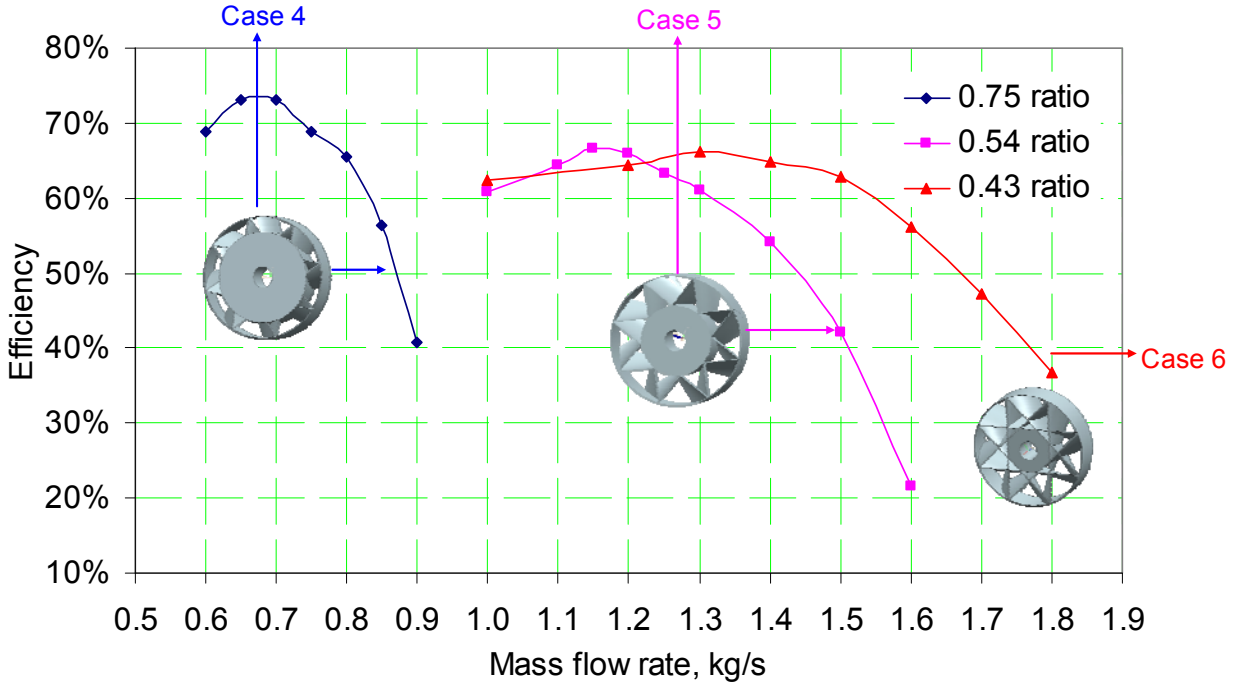
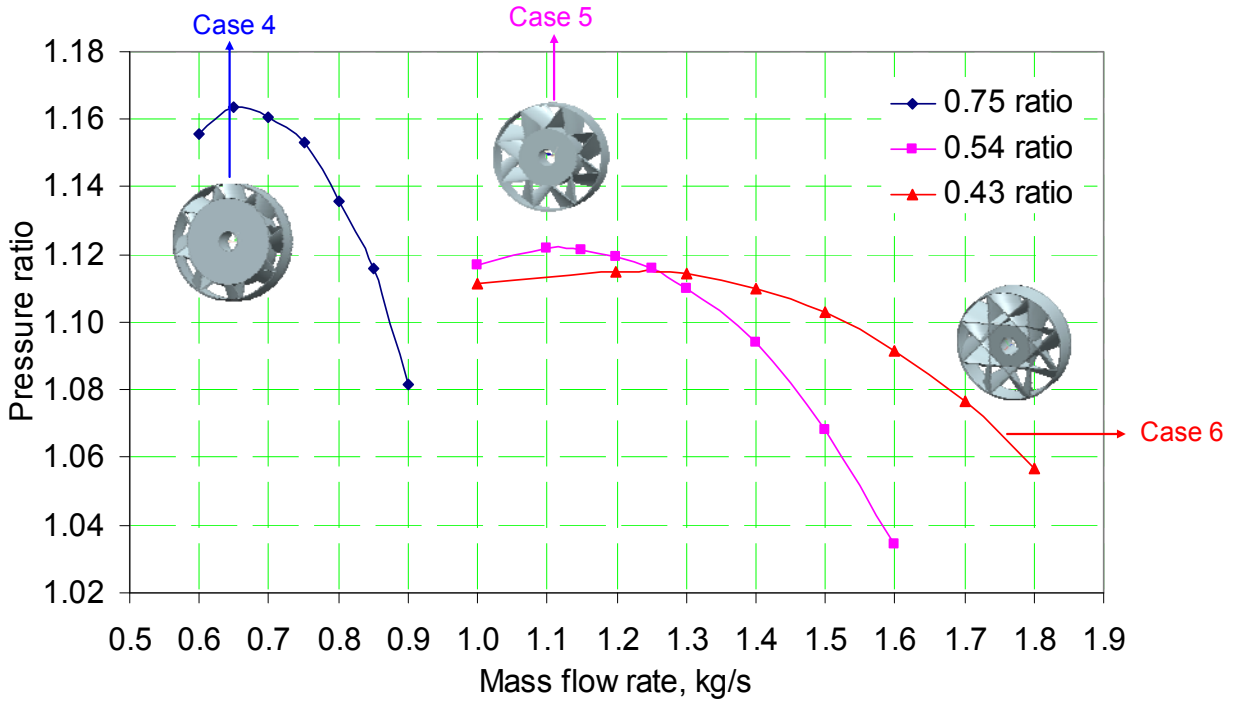


Figure 4-5 Comparison of performance between different hub sizes for pattern 8B

4.4.2 Hub's Effect

As mentioned in the previous section that the bigger of hub size, the better aerodynamic performance in terms of pressure ratio and isentropic efficiency and both of these two patterns present the same trend. The radial blade angle distribution shown in Fig. 4-3 could help explain the mechanism behind such characteristics. The bigger of hub size, the bigger of turning angle of blade thus the bigger of momentum transferred from blade to fluid. Tangential velocity contours at middle planes of pattern C for the biggest and smallest hubs are compared in Fig.4-6, it is clear that because of larger turning angle, tangential velocity becomes higher and more uniform in bigger hub case and it benefits a later kinematic energy transferring into pressure energy through the stator.

By comparing hub's effect for both patterns, the stable operating range of Case 1 and Case 4 are narrower with similar peak pressure ratio. This is due to the contraction of flow area. Since flow from blade channel inlet belongs to subsonic flow, when flow cross section contracts to near critical area, it is accelerating the fluid and easy to get choked in fluid mechanics. Fig 4-7 presents the Mach number contour on the middle planes of pattern B at three different hub sizes for the same mass flow rate of 1kg/s (Case 1-3). Maximum Mach number in Fig 4-7a reaches about 0.54 which is comparable with 0.62 in Fig 4-7b and this explains hub's ratio enlarging from 0.54 to 0.62 shifts choking area to the left a little bit but not as much as Case 3, where maximum Mach number already reaches over one. When the turning angle increases with hub size, boundary separation also increases which induces the beginning of stall and this may explain stall or surge line also shift to the left.

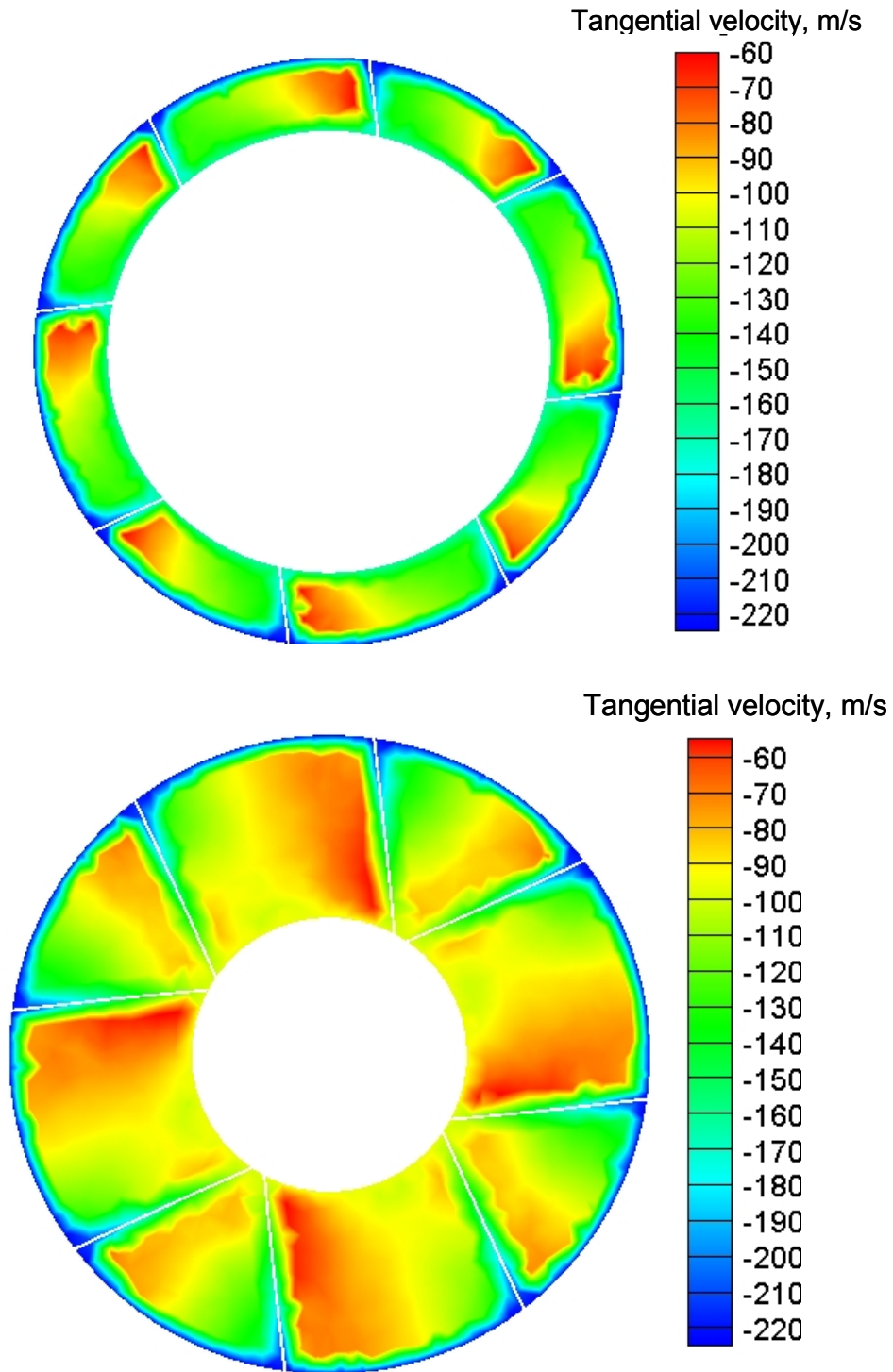
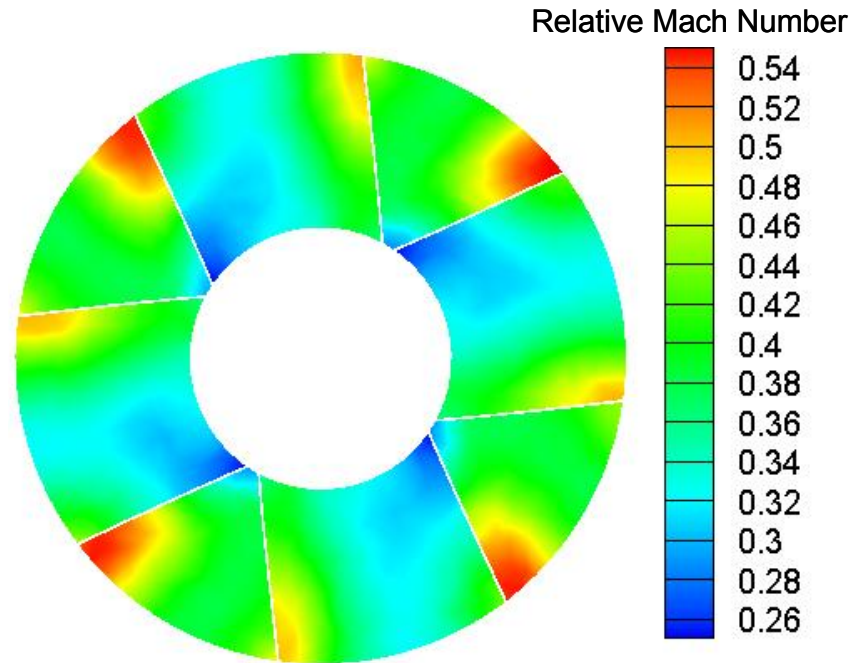
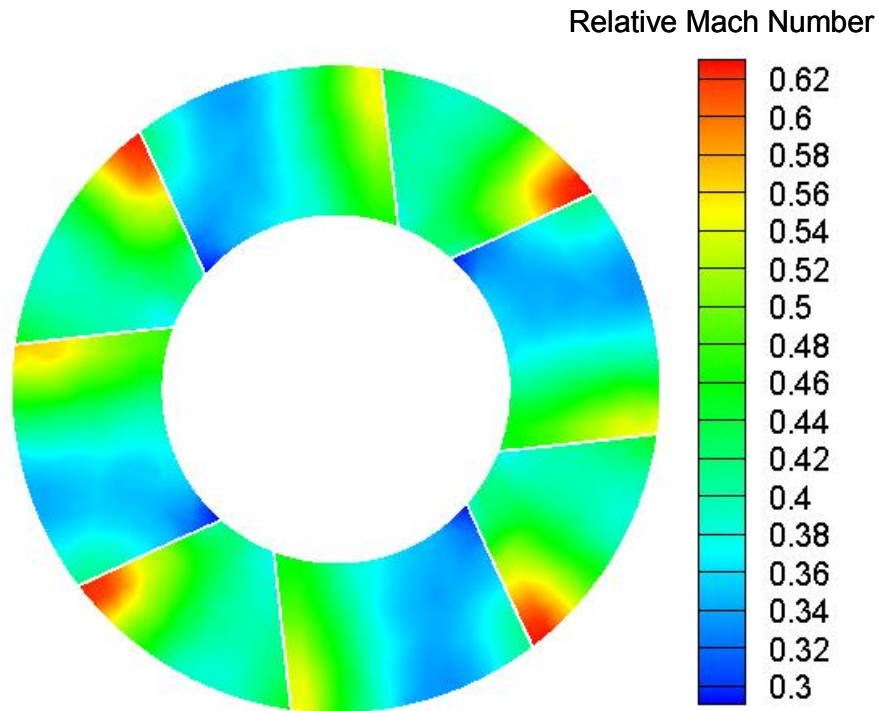


Figure 4-6 Velocity field on the middle planes of pattern C at peak performance point (a) Case 1 and (b) Case 3

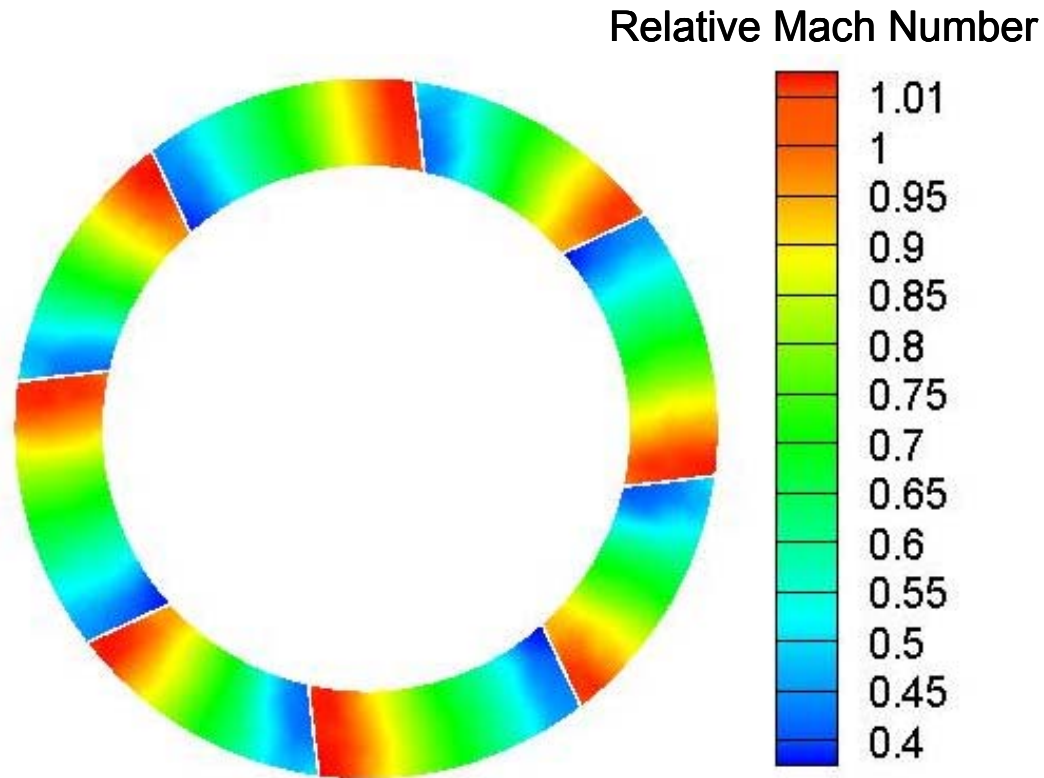


(a)



(b)

Figure 4-7 Mach number contour on the middle planes of pattern C at the mass flow rate of 1kg/s (a) 0.43ratio (b) 0.54 ratio (c) 0.75 ratio



(c)

Figure 4-7 (cont'd)

Similar phenomenon also exists in pattern C from Case 4 to Case 6. However, when hub size increases pattern B's geometry is not changing the same as pattern C that not only flow area is contracted. Pattern B has complicated geometries than pattern C and its pattern's effect is going to address later. Because of the complicated geometry, pattern B's peak isentropic efficiencies do not vary too much when the hub increases from 0.43 to 0.54. Still benefits from a further hub size's increasing to 0.75 can be observed, which are similar to pattern C.

4.4.3 Patterns Effect

In order to compare pattern's affect, performance for two patterns at the same hub/shroud radius ratio are compared. At first, when blade angles are compared in Fig.4-3 one can find that minor difference exists between two patterns at the same hub/tip ratio; however comparing

geometry shown in Fig 4-1 and Fig 4-2 one can notice a main difference between the pattern B and C: in pattern C, eight blades exist and when the hub size increases channel's shape and number maintain the same; while in pattern B, it has sixteen blades and blades are not distributed uniformly and sometimes they are crossing; when the hub size increases, channel's shape and number changes.

Cases for 0.43ratio

In Fig.4-8 the ratio is 0.43 where the hub is small not covering any triangle shapes in 8B, it is observed that peak performance points almost happens at the same mass flow rate (1.3kg/s) for two patterns and 8B yields a higher pressure ratio and isentropic efficiency than 8C. Blade configuration at 8B forms twenty four channels of different shape in comparison of only eight channels for 8C. Therefore two counteracting physical phenomena exist, on one hand wetted surface of all blades in 8B is two times bigger; however, on the other hand the flow control by three time more channels is better and more blades are compressing the fluid which means a possible higher efficiency because of lower deviation angle at outlet. It seems that the last process prevails. Fig 4-9 corresponds to peak point in Fig 4-8 at the same mass flow rate 1.3kg/s for two patterns and it shows that double blade number in 8B results higher pressure ratio. In addition, total temperatures at the outlet of rotors have little difference and they are both about 312K. Therefore, the similar total temperature and significant higher total pressure at outlet reveal a significant higher isentropic efficiency.

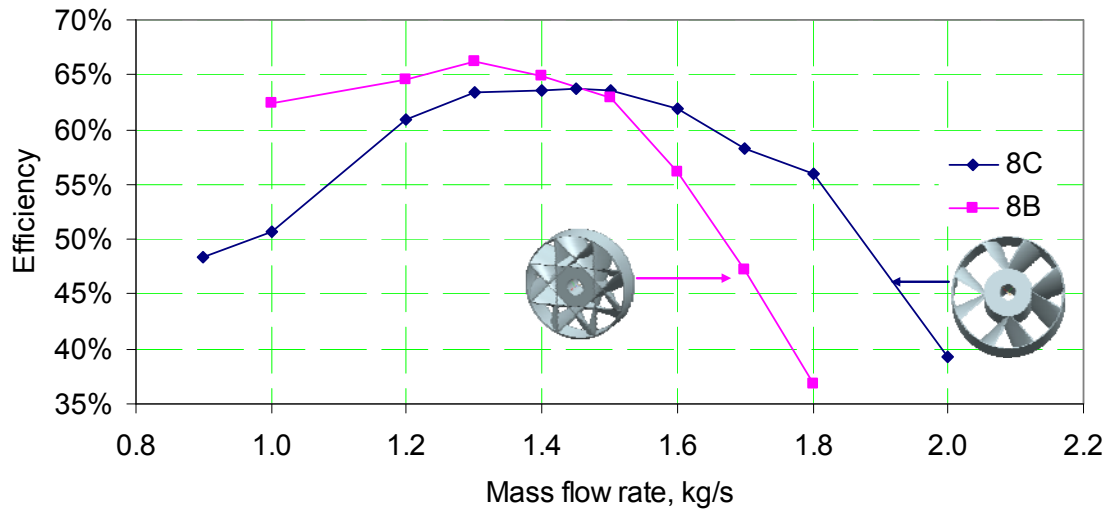
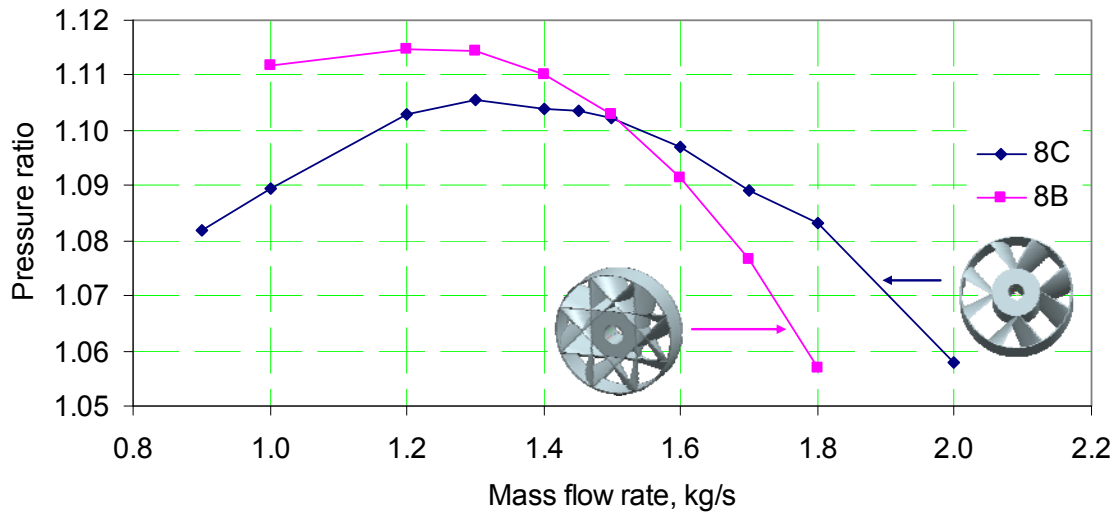


Figure 4-8 Performance comparison between two patterns at the same hub/shroud ratio of 0.43

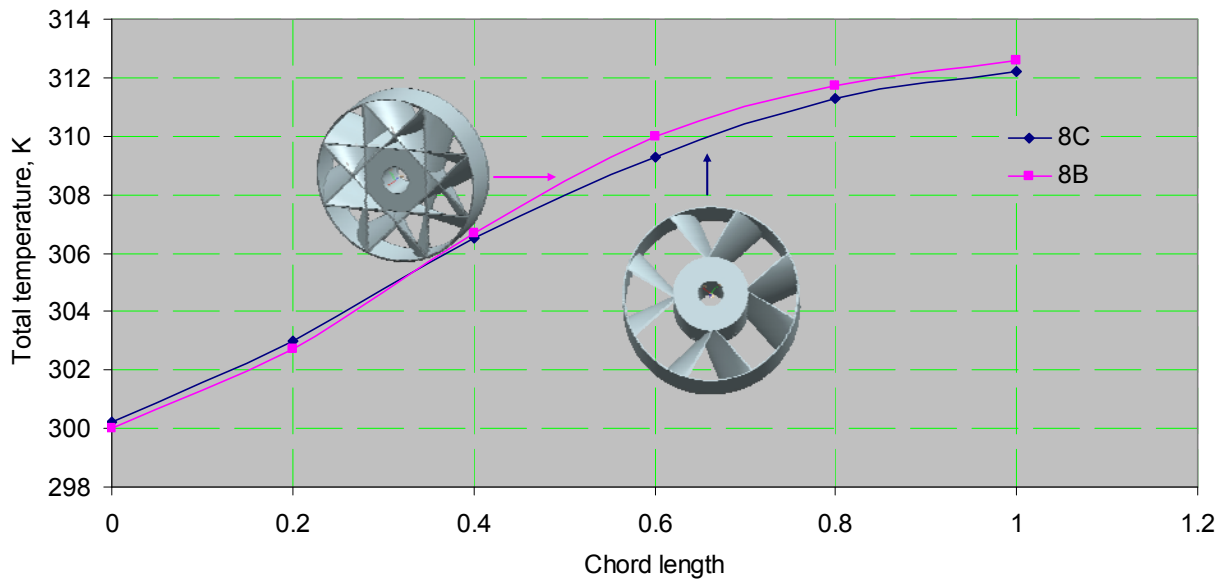
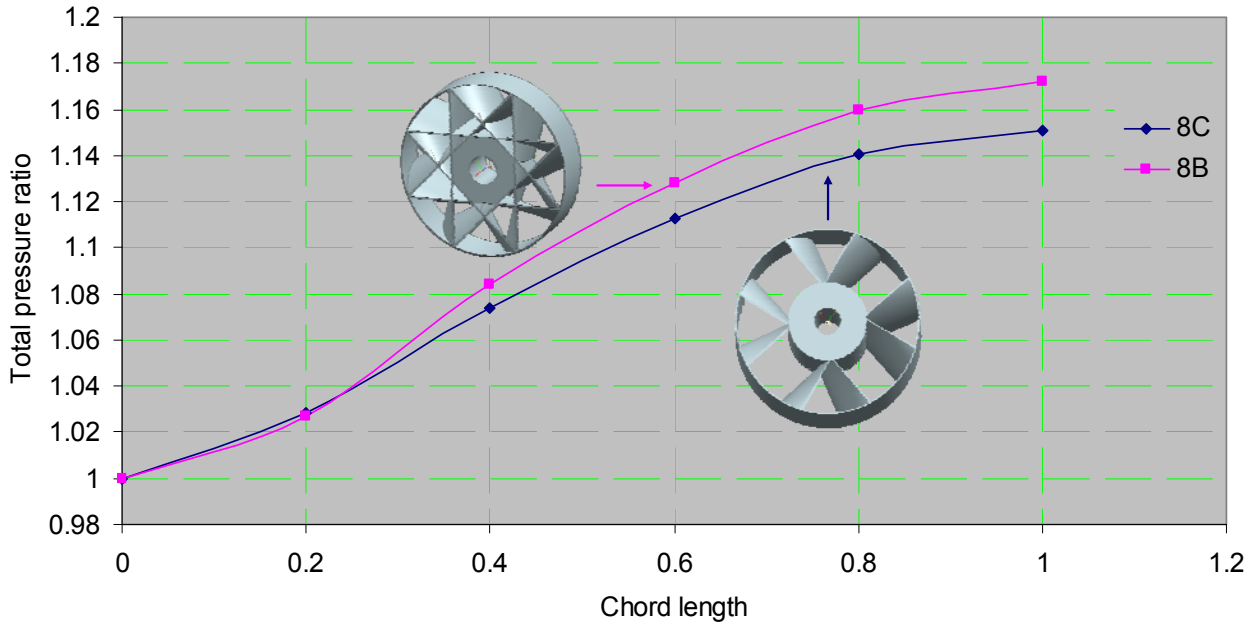
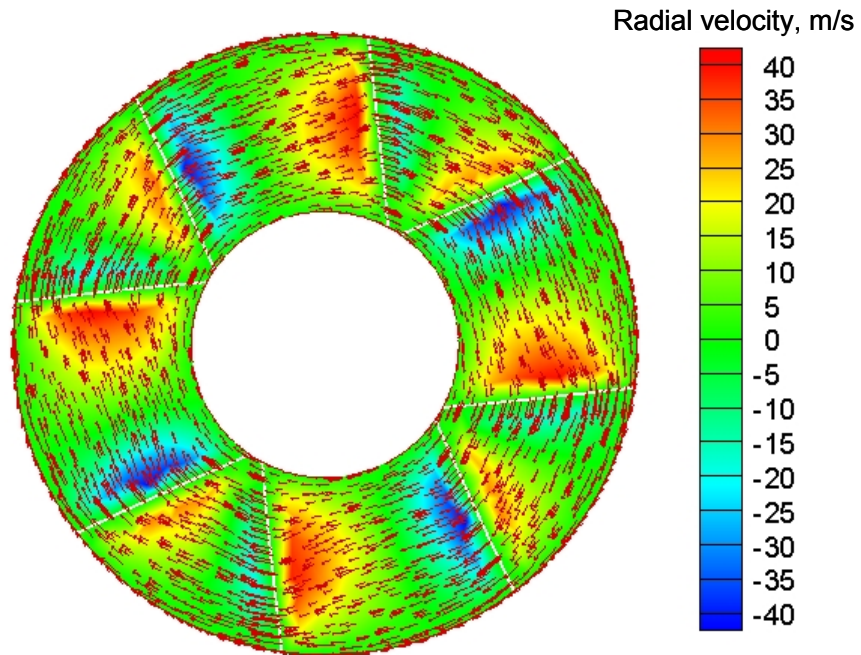


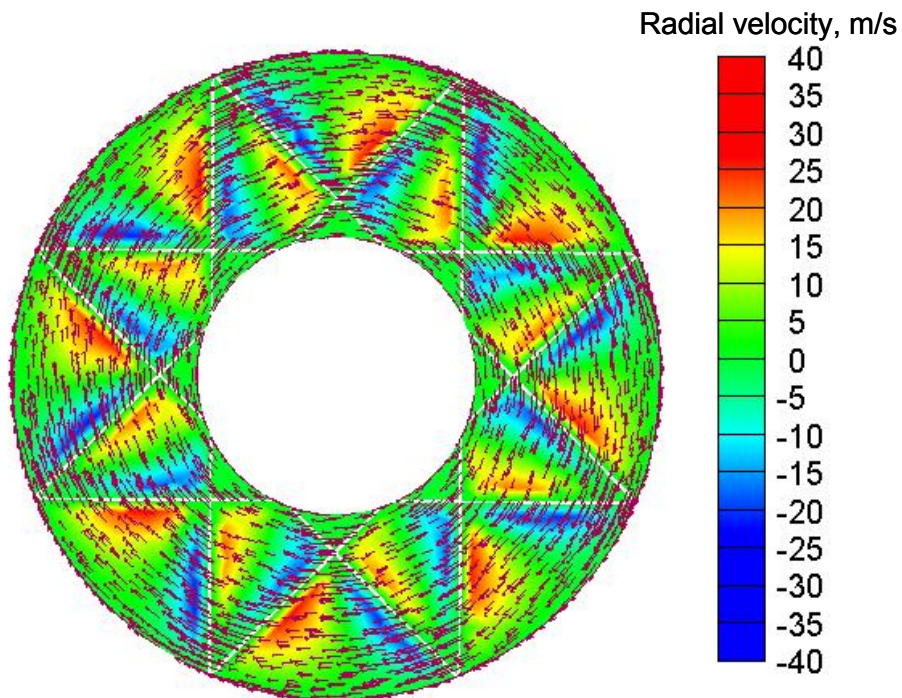
Figure 4-9 Streamwise variation at 1.3kg/s mass flow rate, (a) total pressure ratio (b) total temperature

As it has been discussed in the previous section because of the existence of big blade angle difference between forefront of the blade and inner hub, pressure at blade forefront is higher than inner hub thus pressure gradient forms in the channel and it easily results a considerable secondary flow occurs in the cross section. Channels formed by blade crossing in pattern 8C

helps to reduce this effect because of its blocking effect which in turn benefits a higher tangential velocity. As the blades rotate (clock direction in Fig.4-6), the highest tangential velocity is observed at the forefront of the blades; at the same rotating speed, the same maximum tangential velocity is found for two patterns but the minimum tangential velocity for pattern 8B is 20m/s higher than 8C at the same inlet mass flow rate, it can be explained that because of crossing blade's blocking effect minimum tangential velocity varies. In addition, Fig.4-10 indicates that a larger radial velocity exists in 8C especially in larger rectangular channels, magnitude of maximum value reaches 40m/s while only 22m/s in 8B. The comparison of velocity vectors reveals that the fluid at 8B tends to rotate in the channel rather forming secondary flow, due to the blocking effect and strong tangential flow; because the tangential flow is weaker and radial flow is stronger, flow vector is relatively non-uniform at 8C. By mass weighted averaging on the plane, tangential velocity is 10m/s higher at 8B than 8C and this further illustrates that these novel channels block secondary flow and enhance tangential velocity for same hub ratio of 0.43. Such high tangential velocity potentially increases pressure energy transferred through the stator afterwards and the same flow characteristics are observed for 0.43ratio until mass flow rate becomes larger than 1.5kg/s.



(a)



(b)

Figure 4-10 Velocity field on the middle planes of two patterns at the same mass flow rate 1.3kg/s (a) pattern C (b)pattern B

Cases for 0.54 ratio

In Fig 4-11 at ratio of 0.54, both pressure ratio and isentropic efficiency at peak points are comparable between two patterns. Due to the bigger hub geometry of the pattern B, number of channels decreases to sixteen while blade number of sixteen is the same as 0.54ratio. Flow control is not so good like in the previous case. Comparing geometries in Fig. 4-1 and Fig. 4-2, small triangle's secondary flow blocking effect vanishes and at the same time because of double surface area of pattern B over pattern C, drag force creates friction between blade and fluid which would decrease performance. Effects from both of larger surface area and disappeared fluid guidance from small triangle shapes are supposed to result in comparable performance between these two patters at hub/shroud ratio of 0.54. Therefore 8B is not behaving as good as before and its performance is comparable as 8C.

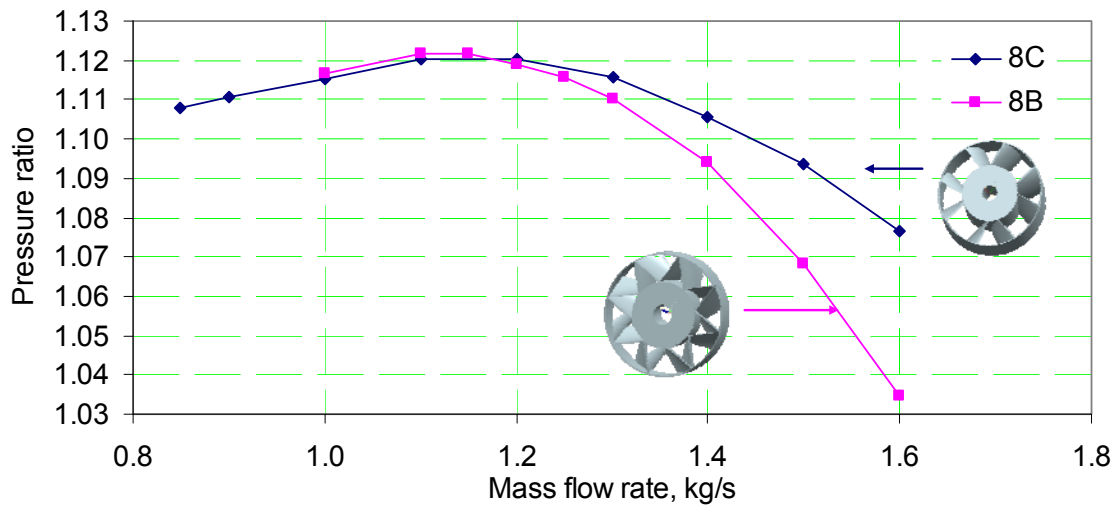


Figure 4-11 Performance comparison between two patterns at the same hub/shroud ratio of 0.54

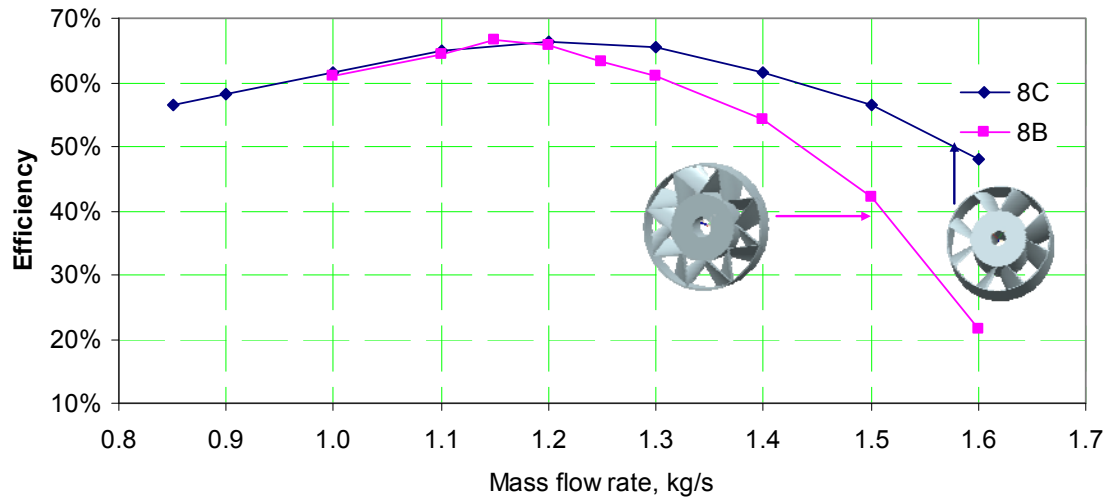


Figure 4-11 (cont'd)

Cases for 0.75 ratio

Similarly Fig. 4-12 can be explained. The peak pressure ratios are comparable but because of small triangle shapes in pattern 8B, peak efficiency is higher for 8B pattern than 8C pattern. The total pressures under the same mass flow rate of 0.7kg/s at exits of Case 1 and Case 4 are both 9162Pa, however total temperature at outlet of 8B is 316K which is about two degree lower than 8C, which reveals that the left small triangle in 8B decreases secondary flow and decreases some amount of kinetic energy transfer to thermal energy. For the biggest hub, when the blades in pattern B form a double blade form, it seems that effect of increased friction is prevailing over the increased flow control.

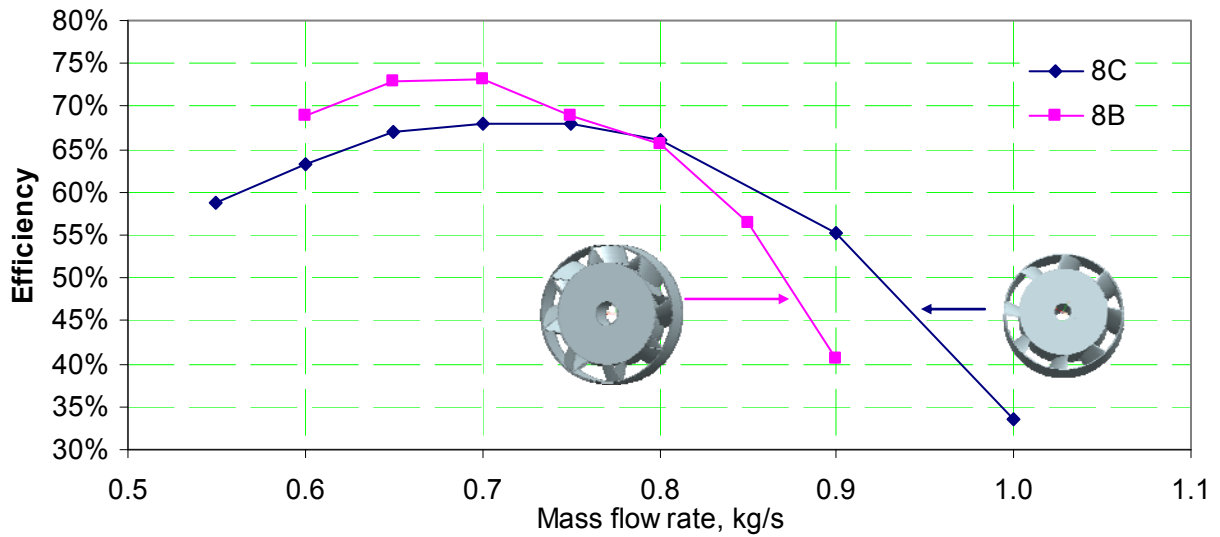
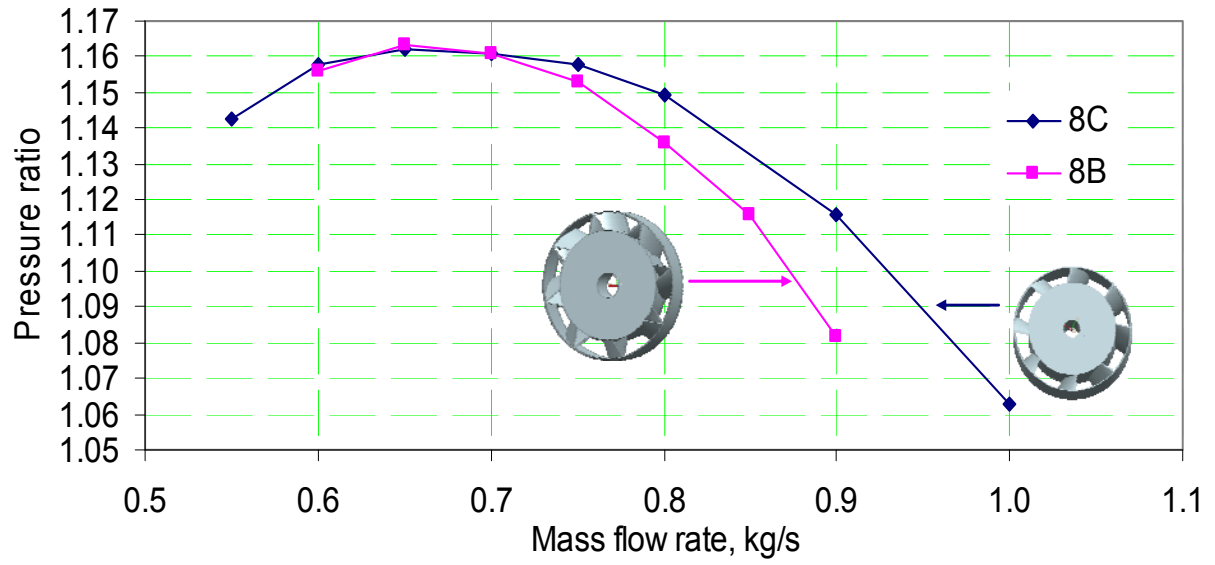


Figure 4-12 Performance comparison between two patterns at the same hub/shroud ratio of 0.75

4.5 Summary

Steady state CFD simulations have been conducted in order to study the characteristics of different axial impeller patterns with different hub sizes. An untypical geometry of an axial compressor is analyzed to obtain its aerodynamic characteristics. Taking into account application for compression of the water vapor in refrigeration installation very specific medium features had to be considered. The calculations are performed on 3-D domains that reproduce the real geometry of the compressor to obtain a virtual performance map at constant tip speed of 220 m/s. Corresponding to different patterns and hub sizes, six cases are studied and the analysis of the flow characteristics is also performed to obtain a better understanding of these novel axial compressor behaviors. Based on the comparison, it was found that pressure ratio and efficiency increase with hub size for the investigated patterns, while a wider stable operating range was found for the smaller hub for the same shroud diameter in all six cases. In addition, by comparing with different patterns it was concluded that because of small triangle shape's secondary flow blockage and flow guidance effects, 8B pattern performs better than 8C patterns especially in combination with a larger hub. All of these results show the potential for these novel axial impellers to compress water vapor as refrigerant. However, further investigations are needed for increased performance and possible optimization that for the best multi-stage performance, different patterns with different hub sizes will be employed at different stages.

CHAPTER 5 Fatigue Life Evaluation to Composite Impeller

5.1 Introduction

Of all the statistical data regarding fracture failure, the study of these events in rotating parts and structures account for more than 80% of the cases [34]. This relates to the high degree of interest in the failure of complicated rotating and moving systems. The root causes behind these failures vary a lot based on different operating conditions, such as high rotational speed and elevated temperature. In general, compressor blade failures can be grouped into two categories: (a) fatigue, including both high cycle fatigue (HCF) and low cycle fatigue (LCF) [35-39] and (b) creep rupture [40]. Blade fatigue failures are often related to anomalies in mechanical behaviors and manufacturing defects. Because the mechanical performance requirements of compressor blades have high theoretical significance and application value, a precise life prediction is very important. Fig.5-1 shows a comparison between different industrial components and their expected life cycles.

Considering centrifugal stresses for the life prediction of impeller blade components, we examine the non-steady-state usage. Typically there is a high accelerating stage during every start-up, where low-cycle fatigue problems exist. The same problem happens at every shut-down period where the deceleration effects cause large LCF problems. In this case, because of large loading changes from centrifugal forces within a short time, low cycle fatigue approaches are suitable to calculate damage in these two periods.

From an aerodynamic viewpoint, when rotor blades rotate, the pressure difference from the suction side and pressure side changes periodically due to the aerodynamic impact from stator. These pressure differences change periodically which produce cyclic loads on rotor blades. Since

this aerodynamic force is typically small compared with centrifugal force, it is usually neglected by investigators [41].

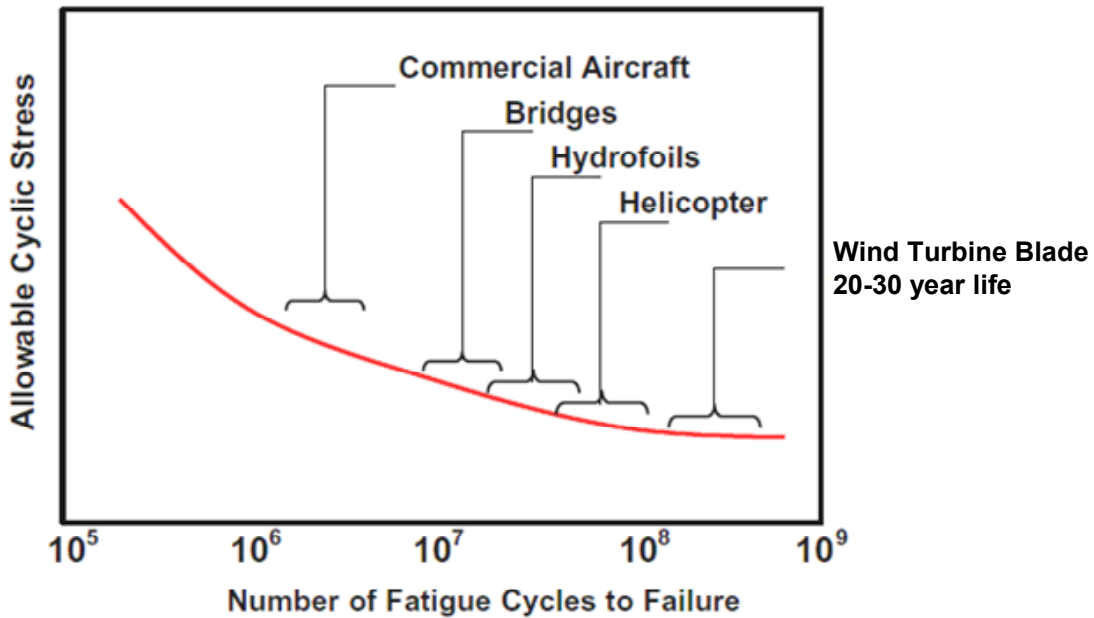


Figure 5-1 Schematic S-N curve for different industrial components [42]

A relative small pressure stress coming from blade’s suction side and pressure side would generate dynamic pressure force changes along the blade’s rotating angle. This force is far less than many materials’ elastic force limit, and investigation of damage accumulation in this period can be done via high-cycle fatigue approaches. Under high temperature and high rpm conditions, this relatively small oscillating force coupled with a high centrifugal force would impact the impeller blades fatigue life, and possibly shorten the service life significantly. In published research, aerodynamic force has been obtained from calculation [42], yet its discussion is typically just limited to the case of steady-state. Dynamic forces from the oscillating pressure forces were not included to evaluate fatigue behavior of impeller blades. To the author’s knowledge, there are few studies that have been conducted considering influence of both oscillating aerodynamic forces and centrifugal forces on a compressor blade’s fatigue life study.

In order to evaluate fatigue life to these two novel axial composite impellers, an investigation was conducted to calculate damage accumulated from an impeller during different working periods. During the first and last period, which are startup and shut down period respectively, large angular acceleration and deceleration caused the centrifugal force to dominate in the structure loadings. Crack initiation or growth is mainly from this stress and it is calculated from ANSYS static analysis. During the standby period, centrifugal force does not significantly vary with time, however oscillating aerodynamic stresses at the critical zone act as the main damage source. These oscillating stresses act to increase damage propagation and crack size; this force is calculated from FLUENT analysis. During these periods, the S-N curve approach is used to calculate fatigue resistance and the accumulation of them is then used to evaluate fatigue life of composite impeller blades.

5.2 Modeling

Impeller geometric patterns have significant influence on the performance of both compressing capacity and structural stability. Fig. 5-2 presents two impeller patterns with the same shroud and hub diameters: 8B and 8C. These two impeller patterns can be manufactured in the same mandrel; thus they share the same blade angles at the shroud. Angle at the leading edge is set at 25 degrees, and 90 degrees at trailing edge (relative to the radial direction). Since the wheel is weaved by crossing slots, different patterns mean different weaving routes for manufacturing. Therefore, blade angles at shroud tip for different patterns are the same, though the distribution of angles on the blade in radial direction is different for different patterns. Considering that there are 8 points on the outer shroud, and from manufacturing view, when the second point of weaving is going to surpass two points, it is named B; and if it is going to

surpass three points, it is named C. Interested readers can refer to detailed manufacturing process and naming method in related publications [43-46].

To make these 3D impeller geometries, IGES data was modeled in Unigraphics NX and the data was then imported into ANSYS to create the finite element model required in the analyses. In the meshing process, a higher order three dimensional solid element SOLID187 was employed to increase accuracy of the modeling. The element is defined by 10 nodes having three degrees of freedom at each node: translations in the nodal x, y and z directions [47]. In order to accurately evaluate the results, convergence analysis was performed. A suitable number of elements were obtained after step-by-step improving mesh density. The stabilization of deflection at a location from the applied loads will be the criteria of convergence.

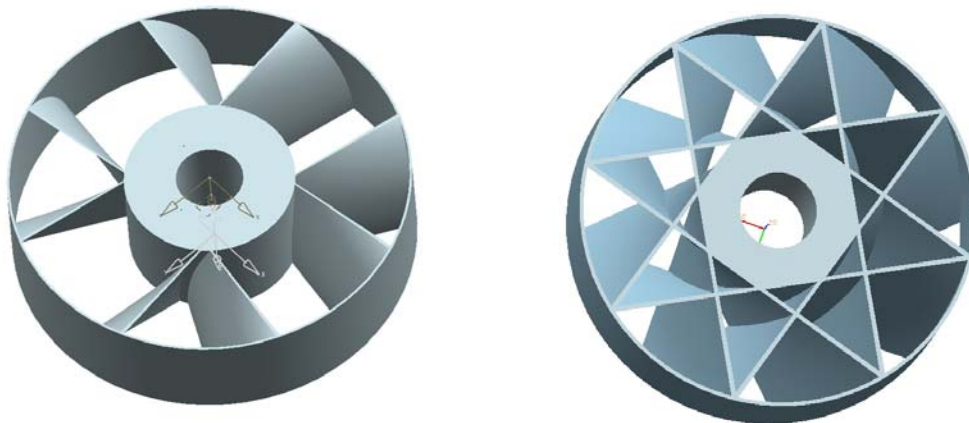


Figure 5-2 Rotor 3D 8C(left) and 8B(right) patterns

In Fig. 5-3, the results of convergence analysis are shown and from this figure it is evident that at least 140,000 elements are required for the convergence. Similar trends are also found for case of 8C where at least 240,000 elements are needed considering convergence issue.

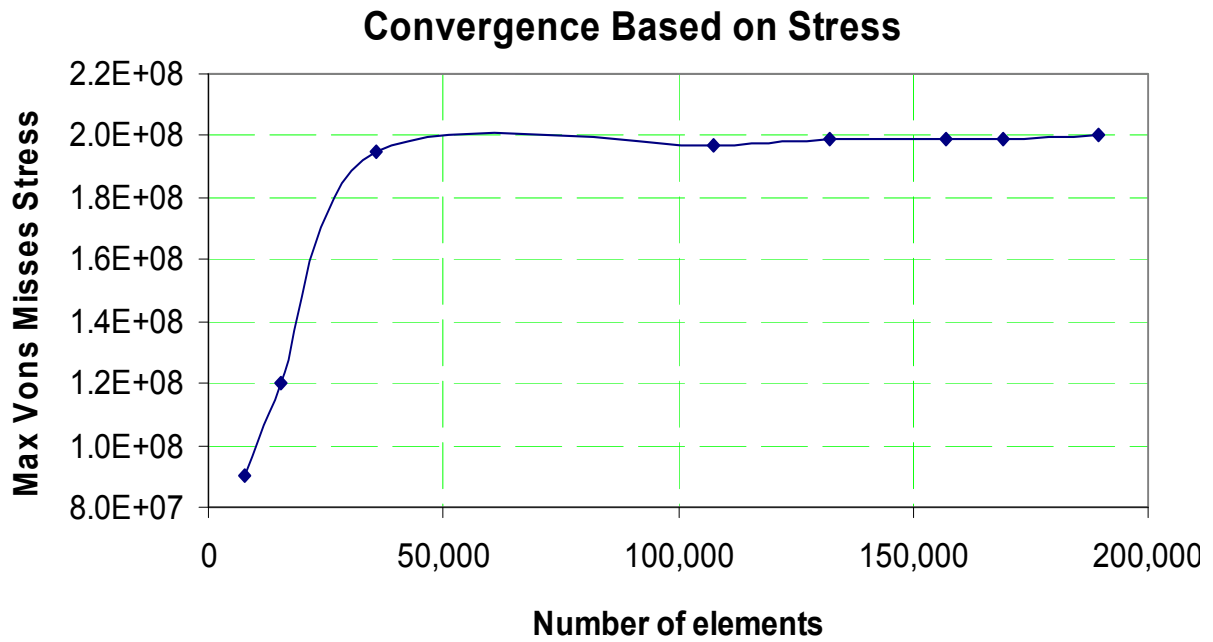
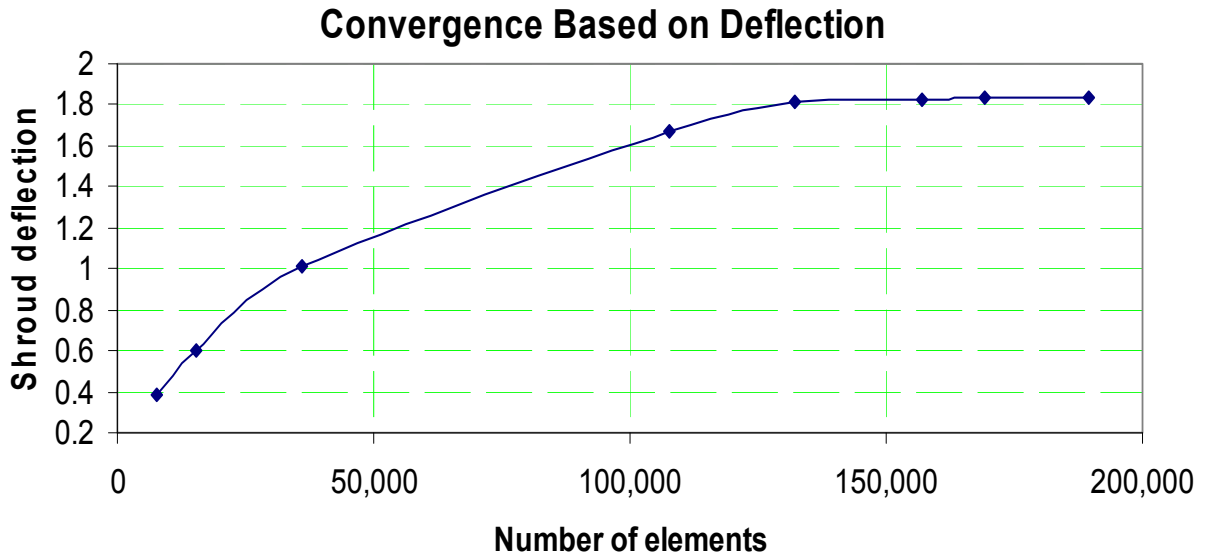


Figure 5-3 Convergence graphs of FE model

5.3 Loading

The loading cases were determined by inspection of the different operating conditions. There are four main operating conditions according to different impeller working periods: 1) Start-up,

2) steady state, 3) standby compression, and 4) shut down. These loading cases were used for fatigue analysis and were treated inter-connectedly since damage accumulated from a previous working period is able to initiate or enlarge crack growth rate for the next one. All of the load cases that occur during the aforementioned events can be categorized as follows:

- 1) Aerodynamic loads on the blade
- 2) Weight of the blade
- 3) Centrifugal forces
- 4) Forces that arise from start/stop angular acceleration
- 5) Thermal effects

All of the above forces were considered as main load events which supposedly influence the impeller blade's fatigue life. However, because temperature changes along the flow channel would vary within 10°C, force coming from thermal effect can be neglected. Gravity's effect can also be neglected considering that the blade is made from composite material and the whole structure is light, and axis of rotation is positioned vertically during operation.

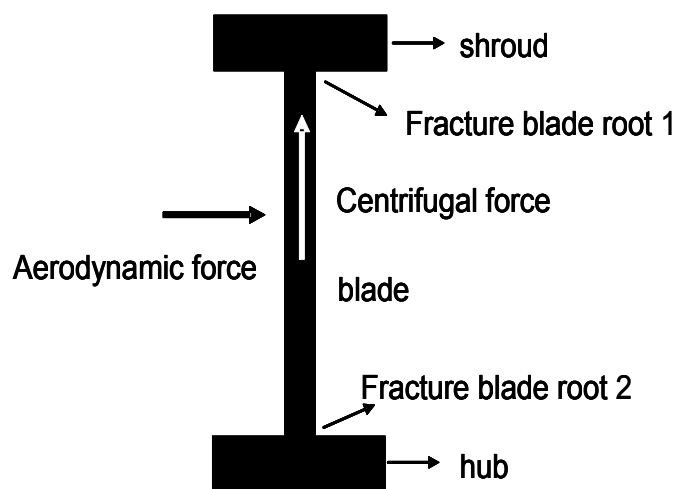


Figure 5-4 Forces acting on a 2D blade

5.4 Composite material's mechanical properties

The required properties for analyzing the structure are material's mechanical properties used for stress analysis, and strength properties used for failure analysis [48]. Through work done by Chapter 3 in manufacturing section, it has been verified that 30% of fiber volume fraction have been obtained through filament winding similar approach and material's mechanical properties barely match with ones calculated through micro-mechanical modeling theory within tolerated difference. In this work, carbon fiber AS-4 from Hexcel Inc (tensile modulus 231GPa, transverse modulus 15GPa, Poisson ratio 0.2) and epoxy SC-15 made by Applied Poleramic Inc. (tensile modulus 26.2GPa, shear modulus 9.17GPa, Poisson ratio 0.35) were used as composite constituents; a similar fiber volume fraction of 30% can be obtained using this novel manufacturing method. According to micro-mechanical modeling theory [22] unidirectional (U-D) composites mechanical properties can be determined from micromechanics. Mechanical properties for the composite materials are shown in Table 5-1.

These orthotropic material properties will be used as input for a further ANSYS simulation. With a fiber volume fraction 30% obtained through the filament winding method, composite density can reach about 1.31g/cm^3 with tensile strength of 1.40GPa.

Table 5-1 Material mechanical properties (GPa)

Material	E_{11}	$E_{22}=E_{33}$	$G_{12}=G_{13}$	G_{23}	$\nu_{12}=\nu_{13}=\nu_{23}$
Carbon fiber	231	15	15	7	0.2
Epoxy	26.2	26.2	9.17	9.17	0.35
U-D composite	87.64	22.84	14.52	8.52	0.31

5.5 Strength Analysis Under Centrifugal Force

The purpose of this section is to identify the weak position of the structure under centrifugal force loading only. Therefore, the temperature field is not considered here and the computations were performed under a temperature of 50°C, which is the testing rig's average testing temperature.

With the start of the compressor, surfaces connecting the shroud and blade body come into steady contact state very quickly. Therefore the FE problem is a nonlinear problem and surface to surface contact elements are used for this purpose. The results of these analyses are summarized in Table 5-2 for 8C and Table 5-3 for 8B; here the rated loads correspond to the speed of 9,000 revolutions per minute (steady-state operation speed). The safety factor results show that in all cases both structures are in a safe condition under rpm of 9,000. When the tip clearance is 4mm, for the maximum shroud deflection case the impeller shroud will not hit the cylinder wall.

Fig. 5-5 shows that the Von Mises stress distribution on the impeller blade 8C and it is shown that maximum Von Mises stress exists at the fracture blade root 1 between blade body and shroud which is supposed to be the critical zone. In addition, considering vibrations of blades, the connection root between blade body and shroud is also a dangerous area where an interaction of low cycle and high cycle fatigue exists. This critical surface results in most fracture failure in service mainly due to the influence of stress concentration factors. As it is illustrated in Fig. 5-6, positions at keypoints 114 and 121 have equal, and the largest, stress concentration factors. These positions are supposed to be weak points, where during start-up and shut down periods centrifugal force is only considered. Changes of aerodynamic force are negligible compared with changes of centrifugal force's change during these two periods. Similar phenomenon can also be observed for 8B pattern in Fig. 5-7. It can be seen that the critical zone locates at the corner

where blades meet together, and it will be the area where maximum damage accumulation occurs when centrifugal force is only considered as the main oscillating stress source.

Table 5-2 Strength analysis of blade under different events 8C

Events	Shroud deflection (mm)	Maximum longitudinal Stress (MPa) (safety factor)	Maximum transverse stress (MPa) (safety factor)	Maximum in-plane shear stress (MPa) (safety factor)
Start-up	1.95	240(5.85)	51.3(1.17)	22(3.64)
Compression	1.84	208 (6.75)	48.1(1.25)	20.3(3.94)
Shut down	2.10	253 (5.55)	53.2(1.13)	24.5(3.27)

Table 5-3 Strength analysis of blade under different events 8B

Events	Shroud deflection (mm)	Maximum longitudinal Stress (MPa) (safety factor)	Maximum transverse stress (MPa) (safety factor)	Maximum in-plane shear stress (MPa) (safety factor)
Start-up	1.23	320(4.38)	52.3(1.19)	28.7(4.75)
Compression	0.87	281 (4.99)	51.2(1.33)	25(4.85)
Shut down	1.35	341(4.11)	54.8(1.16)	30.3(4.04)

NODAL SOLUTION

DEC 12 2010

19:10:01

STEP=1
 SUB =1
 TIME=1
 SEQV (AVG)
 DMX =.001839
 SMN =581708
 SMX =.200E+09

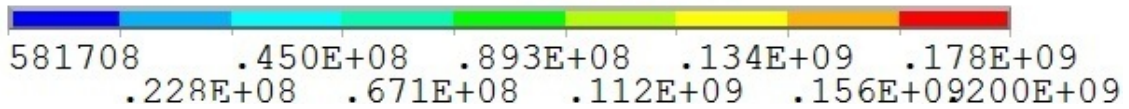
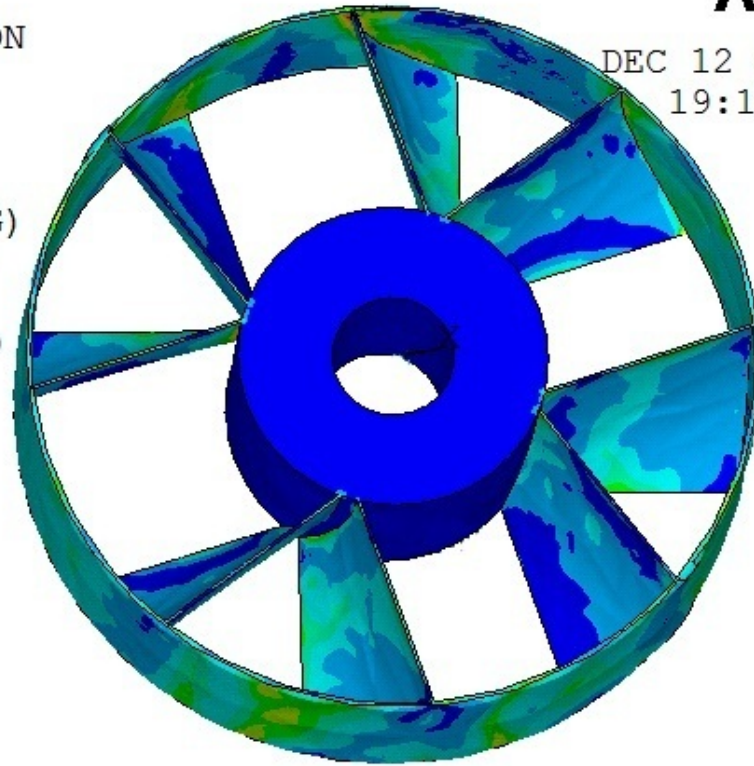


Figure 5-5 Von Mises equivalent stress distribution for pattern 8C

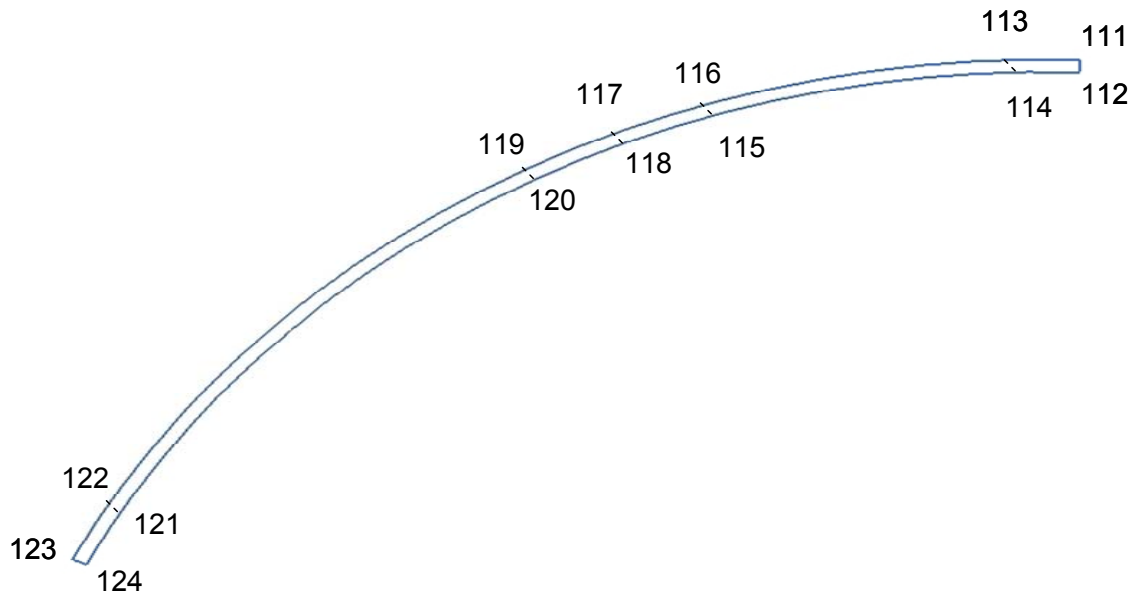


Figure 5-6 Keypoint location in the critical section

NODAL SOLUTION

DEC 12 2010

19:16:25

STEP=1

SUB =1

TIME=1

SEQV (AVG)

DMX =.873E-03

SMN =.101E+07

SMX =.278E+09

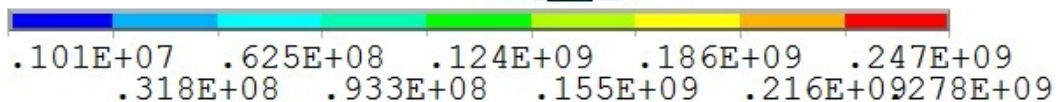
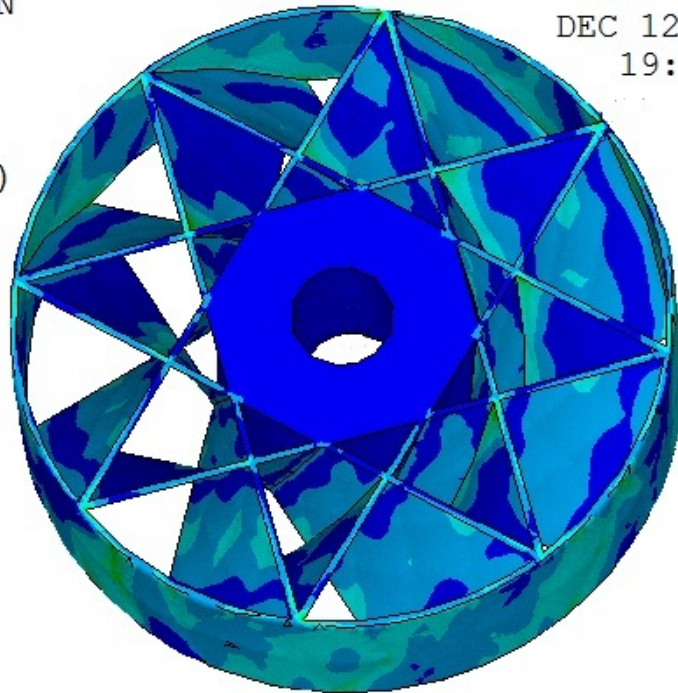


Figure 5-7 Von Mises equivalent stress distribution for pattern 8B

5.6 Strength Analysis Under Peak Aerodynamic Flow

The fluid analysis was carried out to estimate the aerodynamic force exerted on the blade. Simulation was made using the commercial fluid dynamic software FLUENT. One stationary wheel which is similar to rotor pattern and one rotating wheel (8B or 8C pattern) were considered in the model. In the fluid calculation, a moving mesh was used so that the rotor impeller's movement was relative to the rotating fluid's reference frame. The central part, which is mainly connected with a shaft to convert torque, has been ignored for aerodynamic performance calculation. The blade velocity was set to be $r\omega$, where ω is the rotating speed (9,000rpm) and r is the tip distance of the blade from wheel center. The fluid was assumed to be an ideal gas and viscous. The k - ϵ equation was used to model the turbulence where enhanced wall treatment was set up to make sure the y^+ value near the wall was between 20 and 500 [49].

The static pressure distributions around the rotor blade for 8C were calculated and are shown in Fig. 5-8. The maximum static pressure locations are found at the corner between trailing edge of the blade and shroud. This is where the blade imparts kinetic energy the most into pressure energy thus the highest static pressure. When the impeller wheel rotates, transient static pressure at both pressure and suction sides, were also traced and it was found that mean aerodynamic static pressure was about 4,000 Pascal; as seen in Fig. 5-10. A linear distribution of aerodynamic force can be assumed on the blade based on the observation in Fig. 5-8, and this mean stress loading is also the pressure difference between suction and pressure sides. A similar phenomenon can be also observed for 8B in Fig. 5-9. Mean aerodynamic stress from the bending effect at keypoint 114 is 27MPa which is nearly ten times less than centrifugal stress (200MPa). The critical zone of the structure from aerodynamic stress only is located at the fracture blade root 2 between blade body and hub.

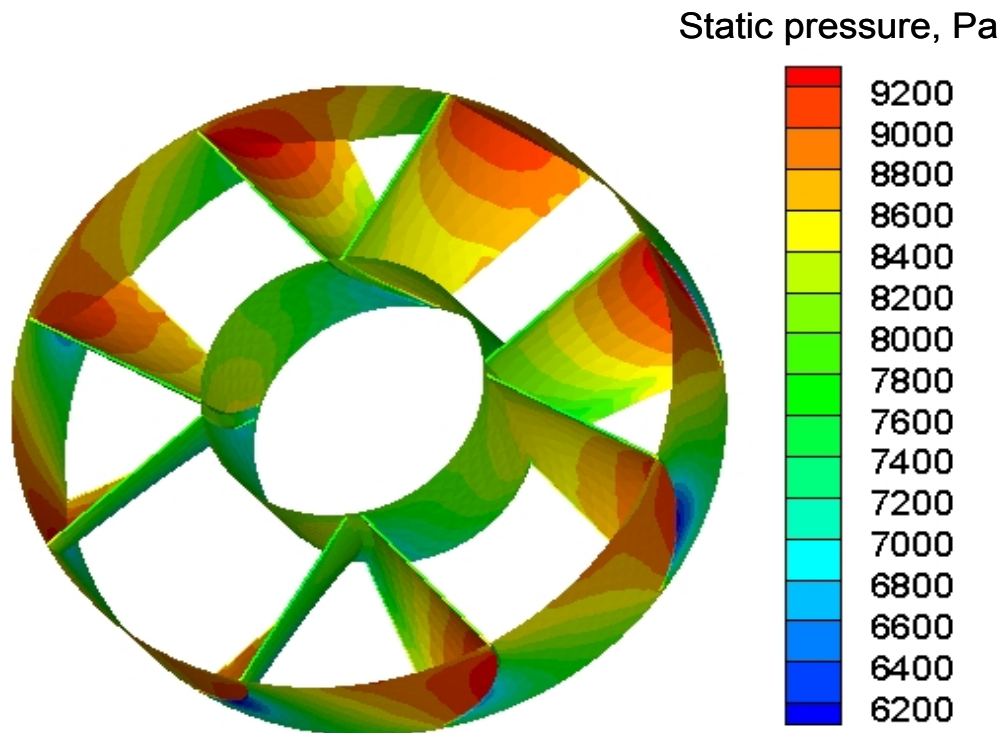


Figure 5-8 FLUENT static pressure distribution on the blade for 8C

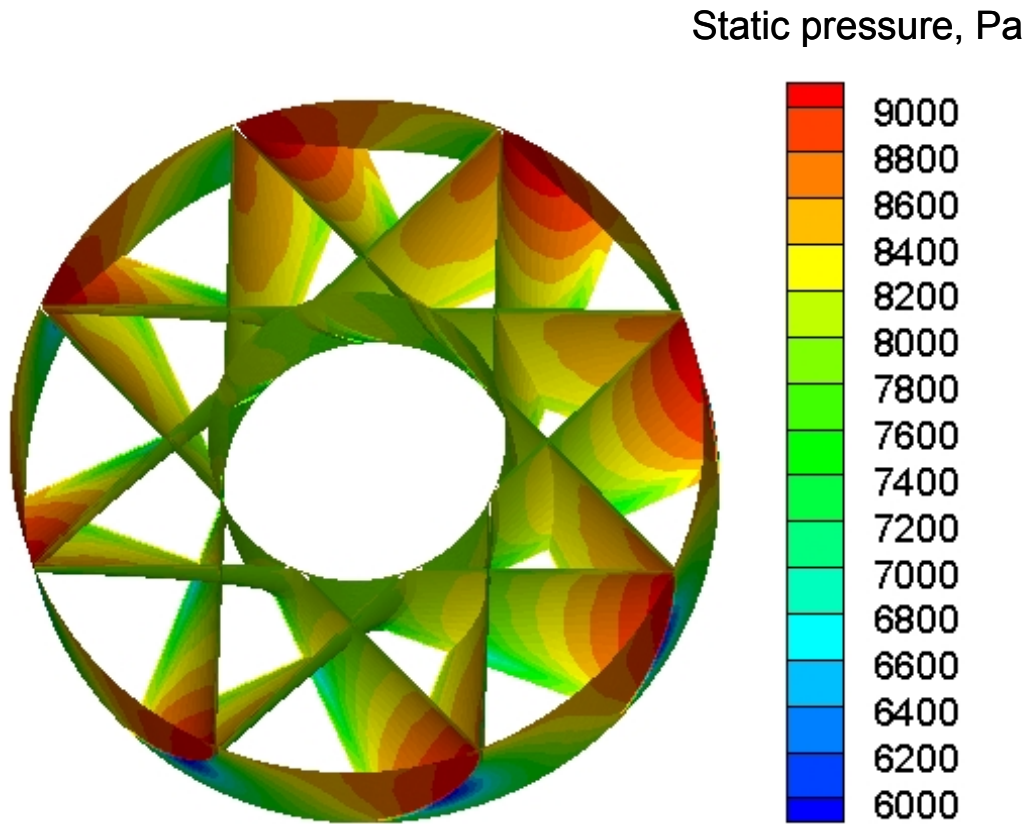


Figure 5-9 FLUENT static pressure distribution on the blade for 8B

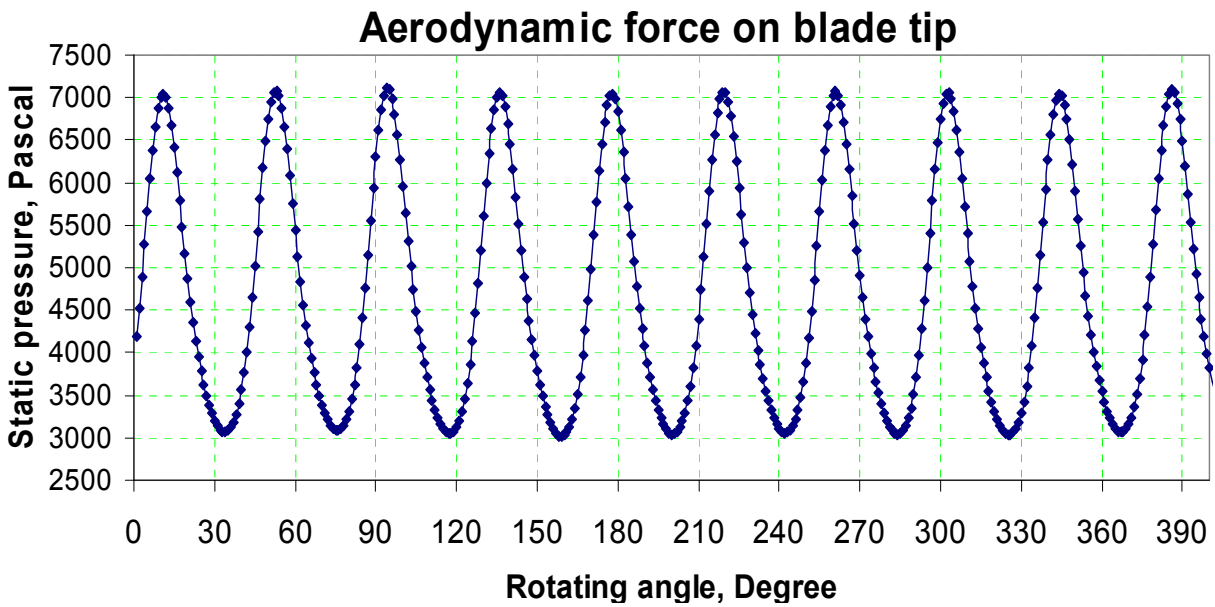


Figure 5-10 Transient static pressure trend at weak point under 9,000RPM for 8C

Linear elastic FEM results based on ANSYS calculation for 8C are listed in Table 5-4 for several critical zones. Where keypoint 114 is the critical zone during the start up period and the keypoint at fracture blade root 2 is the other critical zone when aerodynamic stress is the only load during compression stage.

Table 5-4 Linear elastic FEM analysis results for 8C

Key positions	Linear elastic analysis		
	A. Centrifugal stress (MPa)	B. Aerodynamic mean bending stress (MPa)	A+B
Key point 114 at fracture blade root 1	200	9.3	209.3
Key point at fracture blade root 2	158	27	185

Table 5-5 Linear elastic FEM analysis results for 8B

Key positions	Linear elastic analysis		
	A. Centrifugal stress (MPa)	B. Aerodynamic mean bending stress (MPa)	A+B
Key point 114 at fracture blade root 1	278	1.1	279.1
Key point at fracture blade root 2	162	5.3	167.3

By summing aerodynamic stress and centrifugal stress together, combined stress during compressor standby period which will be important for fatigue life investigation next can be expressed such as:

$$\sigma = \sigma_{centrifugal} + \sigma_{aerodynamic} \quad (5-1)$$

From values listed in Table 5-4, it is readily found that keypoint 114 would be the critical zone during standby stage since it has the biggest stress than other locations. Similar procedures were also taken for 8B pattern where FEM results are listed in Table 5-5.

During standby periods, centrifugal force acts as constant mean stress while aerodynamic bending stress acts in an oscillating manner. Since both weak points in these two patterns locate at the place around keypoint 114, and difference between maximum and minimum oscillating stress from bending effect is small comparing with the mean centrifugal stress, it is thus reasonable to have an R ratio in these two patterns equal to one. The value of this R ratio is considered an important influence factor for crack growth rates [19]. Interestingly in the pattern 8B where centrifugal stress as mean stress is higher than 8C, the magnitude of oscillating stress from aerodynamic mean bending effect is smaller; still distance between this pattern's maximum stress intensity factor and its material's critical stress state is smaller than 8B, and it is found that crack growth rate in 8B during this period will be higher than 8C. By comparing these two patterns, it is obvious that weak positions locate at the same place, where blades intercross with shroud, and the 8B pattern has higher stress intensity factor than 8C, even though a better aerodynamic performance has been found in this pattern [50].

5.7 Accumulated Fatigue Damage

To model damage accumulated for fatigue mechanics of composite material, Ye [51] proposed stiffness degradation technique as a single criteria and based Ye's model, Shookrieh improved it with several practical parameters which make the model more closed with experimental data [52].

Based on the model, a normalized S-N curve in a unidirectional carbon/epoxy composite material under longitudinal fatigue loading has been obtained in Fig. 5-11. The figure is also validated through available experimental data related with fatigue damage modeling of composite materials [53-55]. In order to model accumulated damage during different stages in this study, this figure is used to calculate fatigue cycles at specific stress condition.

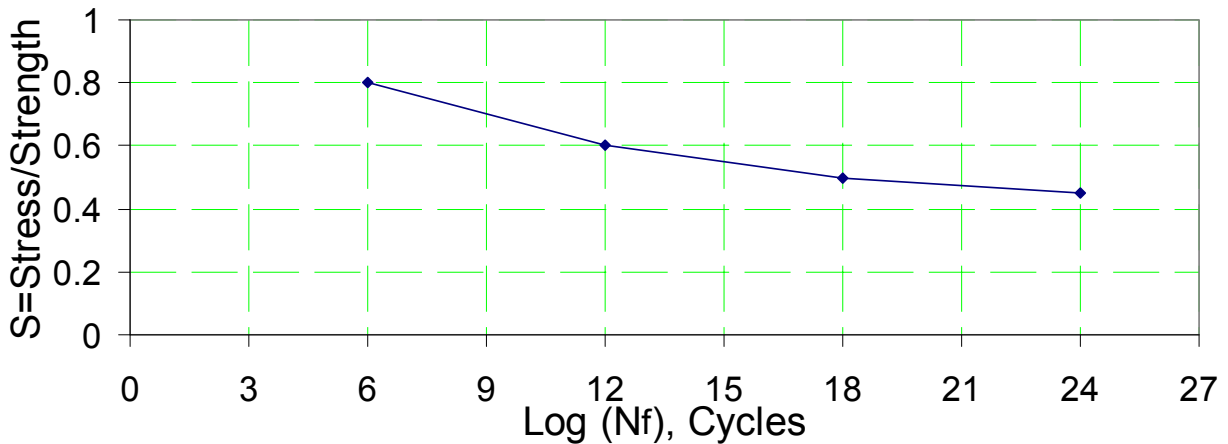


Figure 5-11 S-N for unidirectional carbon/epoxy composite material under longitudinal loading [52]

5.8 Life Prediction Results and Discussion

As it is mentioned at the beginning of this chapter, the main purpose of this chapter is to evaluate fatigue life of two patterns of composite impeller's. This is done by calculating damage accumulated during different impeller working stages. Since centrifugal and aerodynamic stresses are the main loadings considered, load procedures can be simplified as in Fig. 5-12. From stress analysis in previous sections, we have known that there exist stress concentration factors on the fracture blade roots and the critical zone in facture blade root 1 has the biggest dynamic stress changes. It is necessary to consider points such as Keypoint 114 as the weak points for structural life prediction. Similar conclusions have been reached by authors to investigate impeller blade's fatigue life [41, 52].

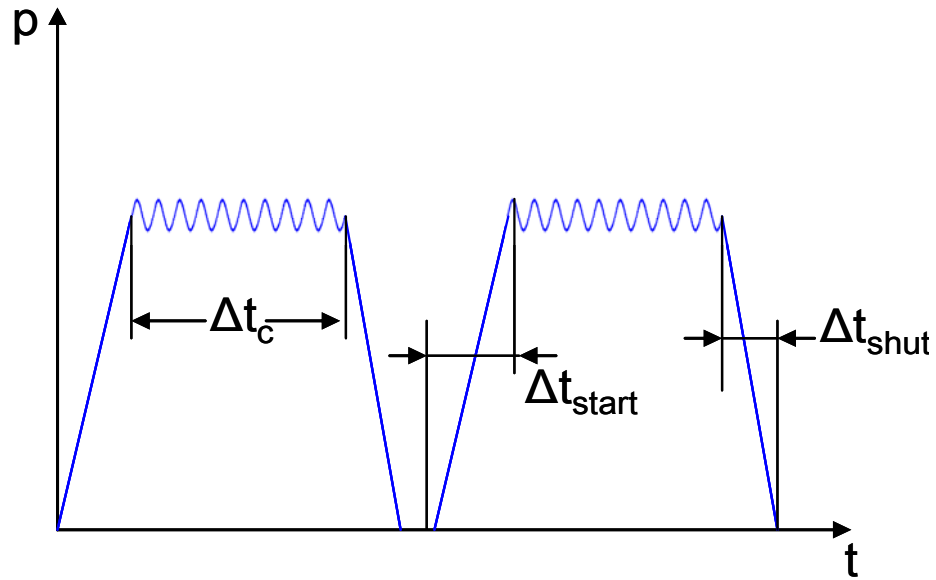


Figure 5-12 Loadings for blade life determination

During compressor start-up period, Δt_{start} , keypoint 114 in fracture blade root 1 is subjected to the heaviest tensile stress. Here this point also has the largest stress concentration factor compared to all other keypoints. Local damaging occurs as micro-crack nucleation occurs. Damage caused by the centrifugal stress is reciprocal to the fatigue resistance of the material at the same load range, $N_{f,i}$ according to Miner's linear rule [56].

$$d_i = \frac{1}{N_{f,i}} \quad (5-2)$$

The damage due to n_i load cycles of the load rang i during different working range, is given by

$$d_{i,n} = n_i \times d_i = \frac{n_i}{N_{f,i}} \quad (5-3)$$

And the total damage caused to the detail by the load cycles of different load levels is thus:

$$D_{tot} = \sum_i d_{i,n} = \sum \frac{n_i}{N_{f,i}} \quad (5-4)$$

In this case, the total fatigue life the impeller blade can be calculated through:

$$\frac{1}{N_f} = D_{tot} = \sum \frac{n_i}{N_{f,i}} = \frac{n_{start}}{N_{f,start}} + \frac{n_{comp}}{N_{f,comp}} + \frac{n_{shut-down}}{N_{f,shut-down}} \quad (5-5)$$

Taking Miner's linear law as above, this composite impeller can rotate 3.2×10^5 cycles with a converted 9455 hours before its catastrophic failure (for 8C) and 7390 hours for 8B. Since Miner's law is based on linear assumption, the law itself is overly conservative in fatigue life predictions, especially in the compression stage where stress change is low and variable amplitude loading in this study is considered. To improve the reliability of the predicted life, effects of vibrations and load variations should be considered. Here, we adopt a modified coefficient of 1.455 for the fracture blade root 1. The number of is based on a scatter factor of loads. From this consideration, we can draw a conclusion that fatigue life time of 6498 hours for 8C and 5077 for 8B is a safe and conservative value.

Following the same procedure, except omitting aerodynamic stress in conventional approaches where only start and stop procedures exist in Fig. 5-12, calculated results in Table 5-6 show that safe fatigue life time for 8C is about 9500 hours, for 8B is 8500 hours. It therefore indicates that by taking into account of the high frequency aerodynamic load with small amplitude, a prediction of safe fatigue life reduces about 32% for 8C and 40% for 8B. Presented results show the importance of proposed methodology taking account terms omitted in conventional approaches; in order to predict a better fatigue life in such complicated geometry,

more sophisticated and exact method integrated with aerodynamic and centrifugal loads should be proposed and applied.

Table 5-6 Life prediction results of patterns

Patterns	Life cycles	Life in hour	Modified life in hour (centrifugal + aero loads)	Modified life in hour (only centrifugal load)
8C	3.2×10^5	9455	6498	9500
8B	2.5×10^5	7390	5077	8500

5.9 Summary

The aim of this chapter was to numerically simulate two types of axial composite impellers' fatigue life using both finite element analysis (FEA) and computational fluid dynamic (CFD) method. This chapter presents first time the consideration of simultaneous influence on the predicted safe life of specific impeller, of two types of load having different features. The low frequency load component is characterized by high load amplitude in contrary to a high frequency aerodynamic load of small amplitude.

In this chapter, carbon fiber/epoxy composites with fiber volume fraction of 30% were used for blade structure. To simplify the modeling process, linear elastic stress strain relationship was assumed for finite element analysis and micro-mechanical modeling theory was used to predict composite's physical and mechanical properties. Convergence issues were discussed and addressed before various loading to the blade, and all load cases, were identified calculated and evaluated and negligible cases were ignored. By performing finite element modeling, the critical zone of the blade can be obtained at the tip of blade. The impeller rotates at the designed rpm of

7000 and safety factors for fatigue life have been calculated based on FE analysis results. In order to better evaluate impeller's fatigue life, this work considered aerodynamic force's effect to the blade beam. From FLUENT calculation, a transient static pressure trend was obtained which provided information for a further calculation of aerodynamic stress bending effect in ANSYS. Methodology of combining centrifugal stress and aerodynamic stress from bending effect would improve fatigue life's investigation accuracy. Based on this methodology and by using Miner's linear law, fatigue life evaluation was conducted based on the detailed simulation results. Considering vibration and load variation effects, the fatigue life was modified. 8C pattern has a fatigue life of 6498 hours and 8B pattern has shorter one 5077 hours. Compared with conventional approaches where aerodynamic loads are omitted, safe fatigue life has been reduced for 32% in case of 8C and 40% in case of 8B. It is thus concluded that aerodynamic loads is important especially when fatigue life is predicted in sophisticated impeller geometry.

CHAPTER 6 Aerodynamic Flow Structure Inside of Woven Wheel Channel

6.1 Investigated impeller blade angle

Similar to the study in Chapter 4 that angle at the leading edge is set at 25 degree and 90 degree at trailing edge relative to tangential direction. Since the wheel is weaved by crossing slots, different patterns mean different weaving route for manufacturing. Therefore, blade angles at shroud tip for different patterns are the same through, distribution of angles on the blade in radial direction are different for different patterns. Flow structure inside of 8B patterns with is going to be studied for its specific flow structure characteristics in this chapter. At it is mentioned in Chapter 4 that this pattern has its special characteristics which make it different from conventional rotors: constant thickness-to-chord ratio from leading edge to trailing edge; the camber line at shroud is a circular arc with one-dimensional optimized blade angle and angles of the blade between shroud and inner hub are determined from the pattern, which can be analytically calculated. Constant thickness-to-chord ratio has the potential to create serious boundary layer separation problems, considering from subsonic fluid mechanics. However, these novel impeller patterns which have small triangle shapes were supposed to guide and benefit the fluid flow as discussed in Chapter 4. In this chapter flow structure inside of two different hub/shroud tip ratios: 0.54 and 0.75 will be investigated.

The impeller has 16 non-radial blades. Since they are non-radial ones, and the blades are not meeting at the wheel's center but at the shroud, conventional design approaches such as one dimensional and two dimensional optimization methods are equipped to deal with this specific pattern. Three-dimensional CFD method was utilized to optimize the best blade angle for the

best performance in terms of pressure ratio and isentropic efficiency for all wheels. Designed rotating speed is 7,000RPM under vacuum pressure environment.

From specific manufacturing principles, the impeller is weaved by crossing slots on a mandrel, where circular arcs were evenly distributed. Therefore blade angle distribution is determined by arcs connected from slots on the mandrel.

Given the axial blade angle at leading and tailing edge β_{inlet} and β_{outlet} on the shroud and the axial length of the arc $L_{ax} = y_{outlet} - y_{inlet}$ determines the camber line at any axial height in Fig.6-1.

For four points marked in Fig.6-1, their coordinates can be expressed as:

$$\begin{aligned}
 x_1 &= R \times \cos\left(\frac{r \times \cos \beta_{inlet}}{R}\right) & x_2 &= R \times \cos\left(\frac{r \times \cos \beta_{inlet} + n \times l}{R}\right) \\
 y_1 &= R \times \sin\left(\frac{r \times \cos \beta_{inlet}}{R}\right) & y_2 &= R \times \sin\left(\frac{r \times \cos \beta_{inlet} + n \times l}{R}\right) \\
 z_1 &= r \times \sin \beta_{inlet} & z_2 &= r \times \sin \beta_{inlet} \\
 \\
 x_3 &= R & x_4 &= R \times \cos\left(\frac{n \times l}{R}\right) \\
 y_3 &= 0 & y_4 &= R \times \sin\left(\frac{n \times l}{R}\right) \\
 z_3 &= 0 & z_4 &= 0
 \end{aligned}$$

Therefore point 1 and 2 determine any point located at leading edge

$$f_{leading}(x,y,z)=f(\text{point1, point 2}) \quad (6-1)$$

and point 3 and 4 determine any point located at trailing edge

$$f_{trailing}(x,y,z)=f(\text{point3, point4}) \quad (6-2)$$

Blade angle connecting leading edge and trailing edge can thus be expressed as:

$$\theta = \arccos \left(\frac{z_{leading}(t) - z_{trailing}(t)}{\sqrt{(x_{leading}(t) - x_{trailing}(t))^2 + (y_{leading}(t) - y_{trailing}(t))^2 + (z_{leading}(t) - z_{trailing}(t))^2}} \right)$$

(6-3)

Where t changes from 0 to 1 it means the point on leading edge moves from point 1 to point 2, or on trailing edge: the point moves from 3 to 4. Parameter of 'n' determines weaving process for different patterns. In this study for the 8B pattern, 'n' here equals three.

Based on the equations above, blade angle, from inner hub to shroud, is plotted in Fig. 4. For the optimized blade angle this relationship is a curve, not a straight line like the one in conventional axial impellers where blade angle is optimized for a certain incidence angle. Blade 1 and blade 2 are symmetric to each other at its blade center (not at wheel's center), while blade 3 which meets blade 1 on the shroud has the same blade angle as blade 1. Therefore it was discussed that only on some specific radius the expected incidence angle can be realized, and this is another main difference from conventional impellers. For this special impeller, shroud has been integrated together with the wheel and end wall region which is characterized by very complex flow structures is also contained within rotating fluid area; therefore in this work, no attempt was made to evaluate clearance effect to the performance and it would only be an important issue considering from vibration and deflection from different loadings.

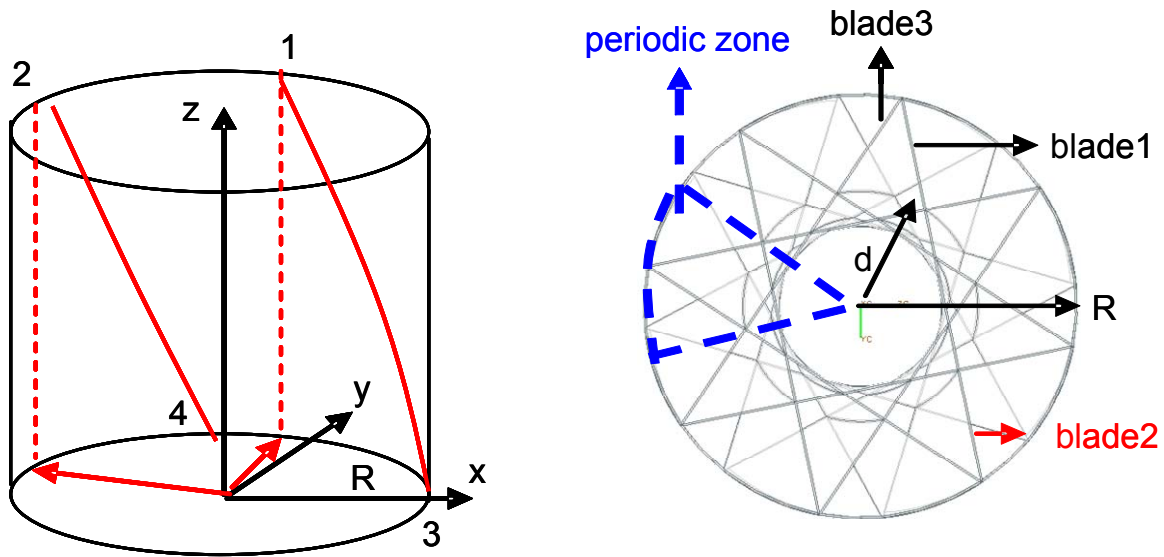
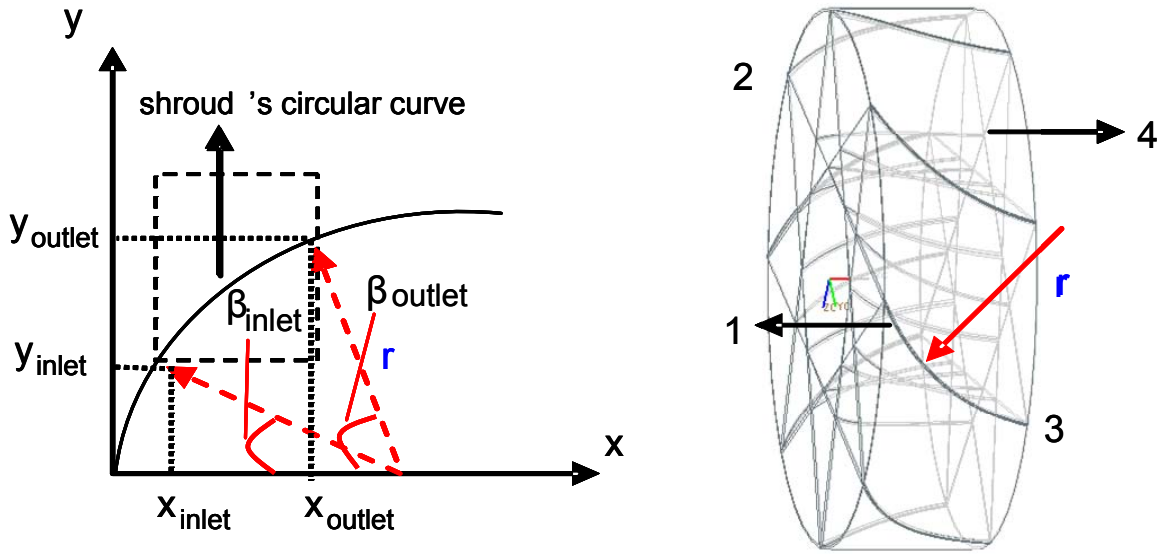


Figure 6-1 Axial-line blading without hub

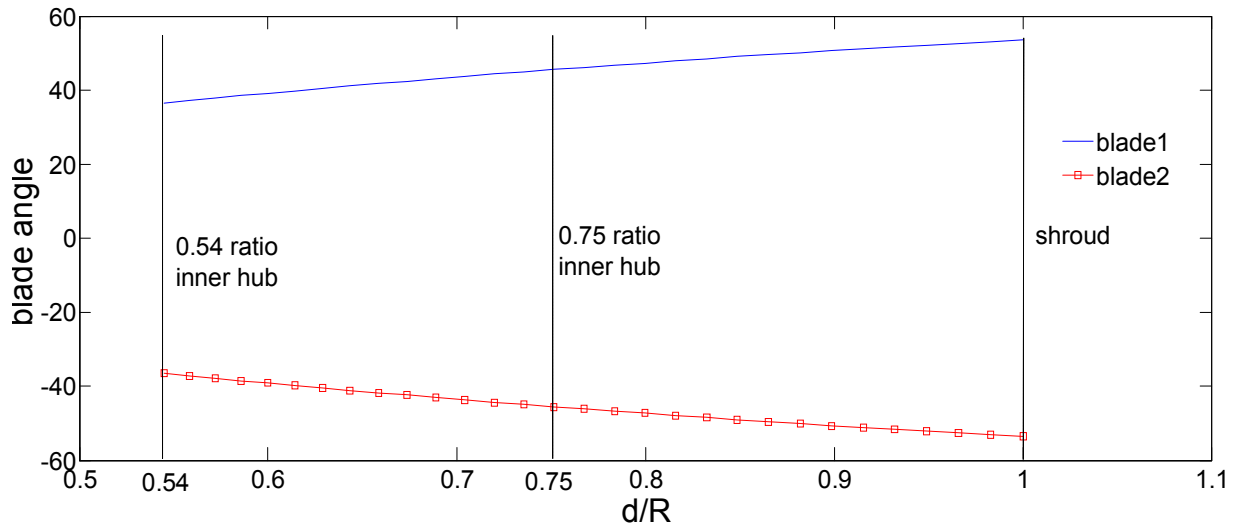


Figure 6-2 Blade angle along radial direction

6.2 Results and Discussion

The comparison of performance maps for two different hub/tip ratios is given in Fig.6-3, 6-4 and Fig. 6-9, 6-10. The calculation uses the dimensionless quantities of pressure ratio Π (equation (6-4)), isentropic efficiency η_C (equation (6-5)) and mass flow rate χ (equation (6-6)). Stage total pressure ratio (Π_C) and isentropic efficiency (η_C) of the compressor are calculated based on the total pressures (P_{total}) and total temperatures (T_{total}) at both inlet and outlet of the compressors.

$$\Pi_C = \frac{P_{total-outlet}}{P_{total-inlet}} \quad (6-4)$$

$$\eta_C = \frac{(\Pi_C)^{0.254} - 1}{\frac{T_{total-outlet}}{T_{total-inlet}} - 1} \quad (6-5)$$

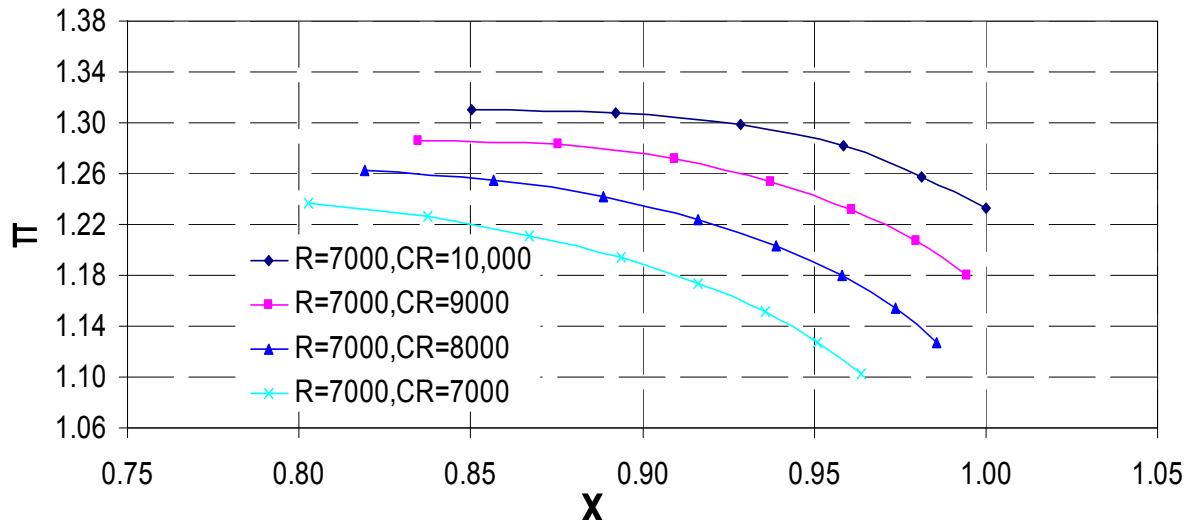
$$\chi = \frac{\dot{m}}{\dot{m}_{ref}} \frac{p_{t1-ref}}{p_{t1}} \sqrt{\frac{T_{t1}}{T_{t1-ref}}} \quad (6-6)$$

It is thus total-to-total pressure ratio and efficiency. For temperature and pressure, mass-averaged values are used at the outlet. The overall performance of the compressor with different speed ratio (r) is shown in Fig.6-3 and 6-4 for 0.54 hub/shroud tip ratio. When speed ratio is the biggest at $r > 1$, which means counter rotating wheel rotates the fastest, whole stage produces the highest pressure ratio; on the other hand peak efficiency and stable operating range are the lowest among different speed ratios. The same phenomenon has also been observed when $r < 1$. When hub/tip ratio increases to 0.75, the performance curves were illustrated in Fig. 6-9 and 6-10, where a significant pressure ratio increased comparing with 0.54 hub/shroud tip ratio. In order to understand the results shown, in the following sections two hub/tip ratio cases were investigated separately, and the flow characteristics are analyzed. Based on the analysis of the CFD results, the advantages of utilizing this novel axial counter rotating impellers setting and the optimization of stage configurations will be described.

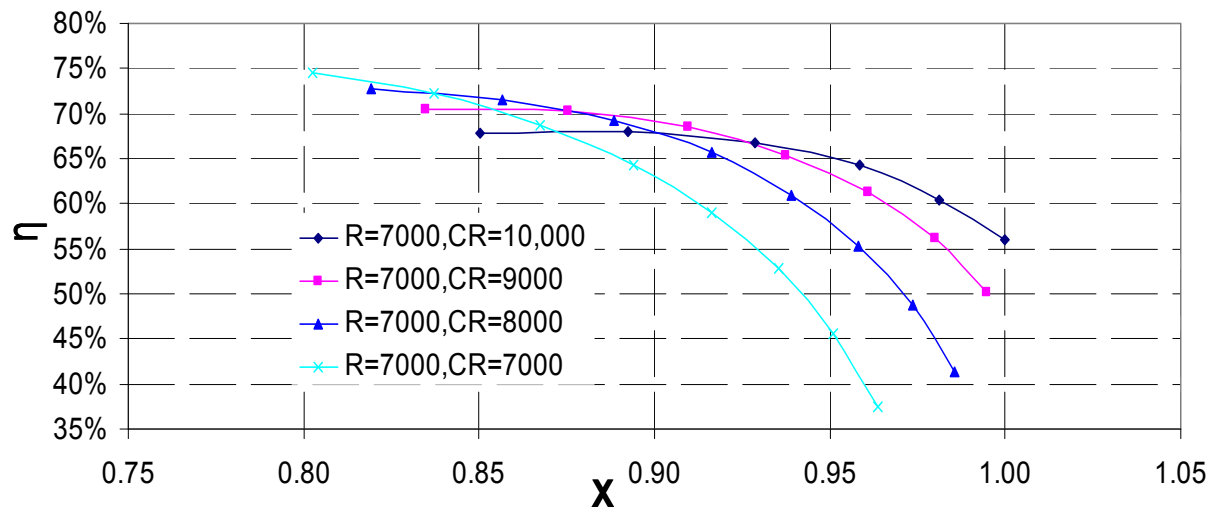
6.2.1 Case 1 0.54 hub/tip ratio

As it is shown in Fig.6-3 at the fastest counter rotating speed, the whole stage has the highest pressure ratio. The pressure ratio is high mainly because of higher tangential velocity which adds the largest kinetic energy thus improve pressure ratio after stator. When speed ratio r is less than one, as in Fig.6-3, however, efficiencies at the peak point decreases when counter rotating speed increases. In Fig.6-4, we can see that pressure ratio rises when counter rotating wheel's speed increases, while peak efficiency doesn't vary too much when speed ratio changes. In addition, stable working range narrows when the counter rotating wheel speeds up. This is because it

brings a rapid increase of Mach number. Mach numbers rapid increase easily results in choke conditions. Thus a shorter stable working range is available in comparison to others. This is one of challenges for counter rotating technology when a higher pressure ratio is desired, a wider stable working range is required.

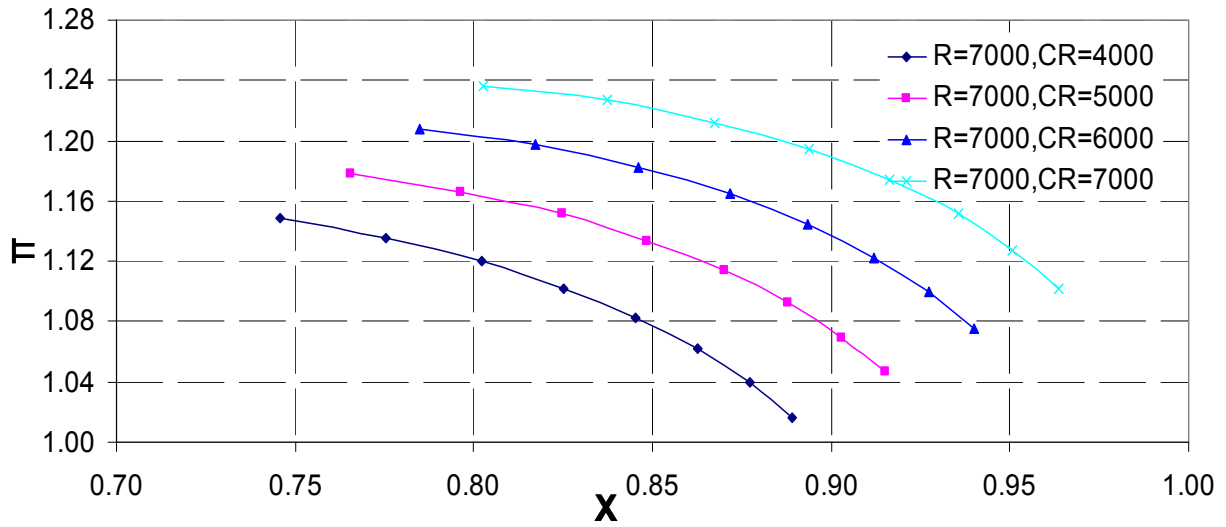


(a)

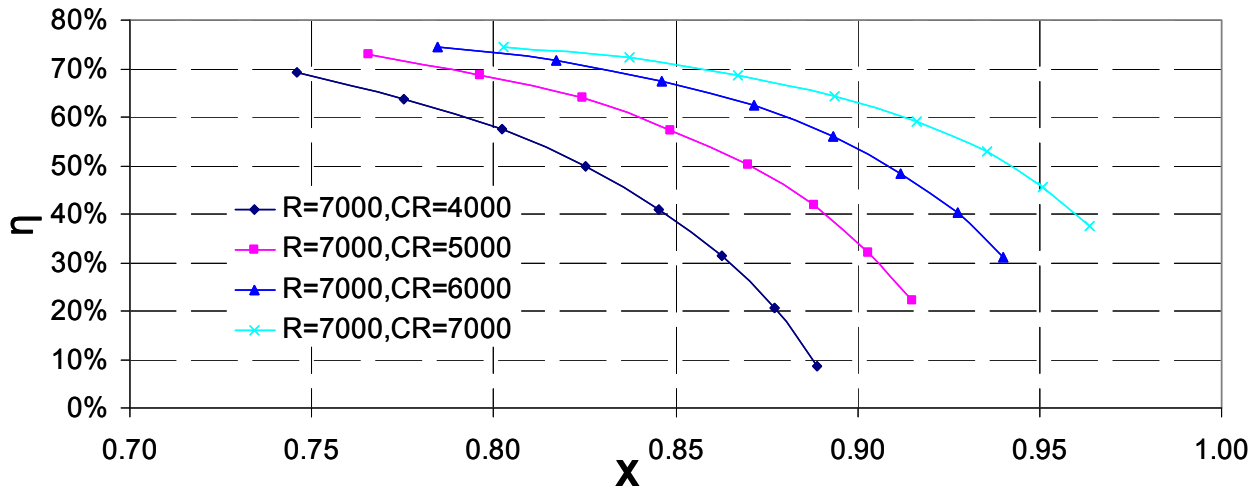


(b)

Figure 6-3 Total pressure ratio curve (a) and isentropic efficiency curve (b) at different $r < 1$ rotational speed ratio (0.54ratio)



(a)



(b)

Figure 6-4 Total pressure ratio curve (a) and isentropic efficiency curve (b) at different $r>1$ rotational speed ratio (0.54ratio)

Fig.6-5 compares circumferentially-averaged relative inlet flow angles at different rotating speed's stall points, when counter rotating speed increases from 7000RPM to 10,000RPM. In the figure, blade angle's distribution has been converted from Fig.6-2 where hub position at hub/tip ratio of 0.54 is marked as starting at the x axis in Fig.6-5. At the designed point when two wheels rotating at both 7000RPM, as it is mentioned previously, for this special blade incidence angle was matched with flow only on blade position; in this figure, an optimum incidence angle exists

around 30% span. However, this angle keeps increasing until it reaches around 45% span and it drops down until around 50% span. Incidence's fluctuation will possibly bring total pressure loss's change, which would influence each wheel's performance. When counter rotating speed increases to 9000RPM and 10,000RPM, incidence angle increases further and it results a large production of swirl and heat generation, which brings down peak efficiency; when counter rotating speed decreases to 5000RPM and 4000RPM, swirl's effect on rotor impeller induced by counter rotor would be less serous. This may be the main reason explaining how counter rotating wheel's speed affects the whole stage's isentropic efficiency.

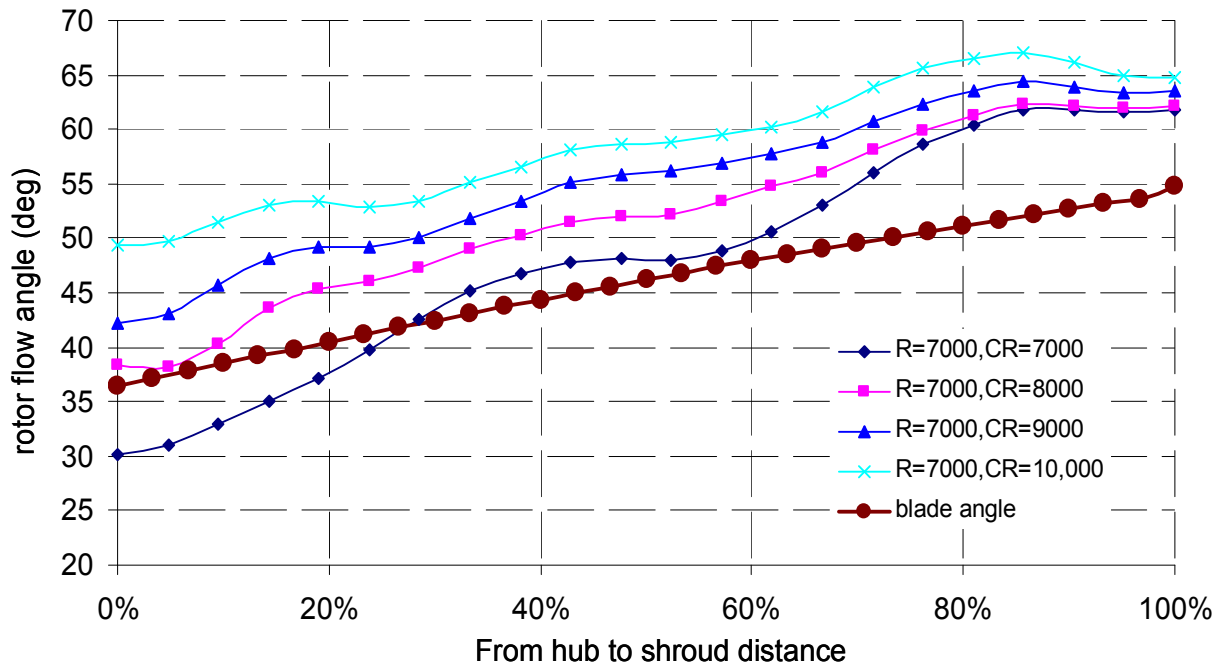


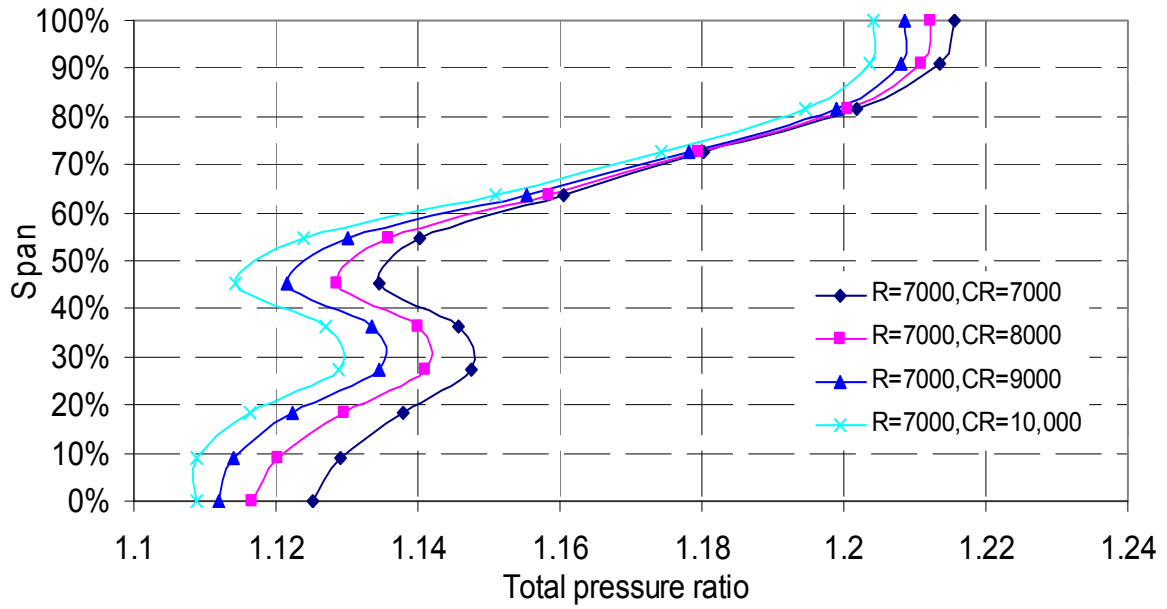
Figure 6-5 Flow angle and blade angle of the rotor at different rotating speed ratio stall point (0.54ratio)

To further analyze flow characteristics in the channel, circumferential averaged total pressure ratio and isentropic efficiencies for two rotating wheels are illustrated in Fig.6-6 and Fig.6-7. From Fig.6-2, it is known that blade angle increases thus increases tangential kinetic energy from hub to shroud and a later conversion into pressure energy through stator; therefore, it is

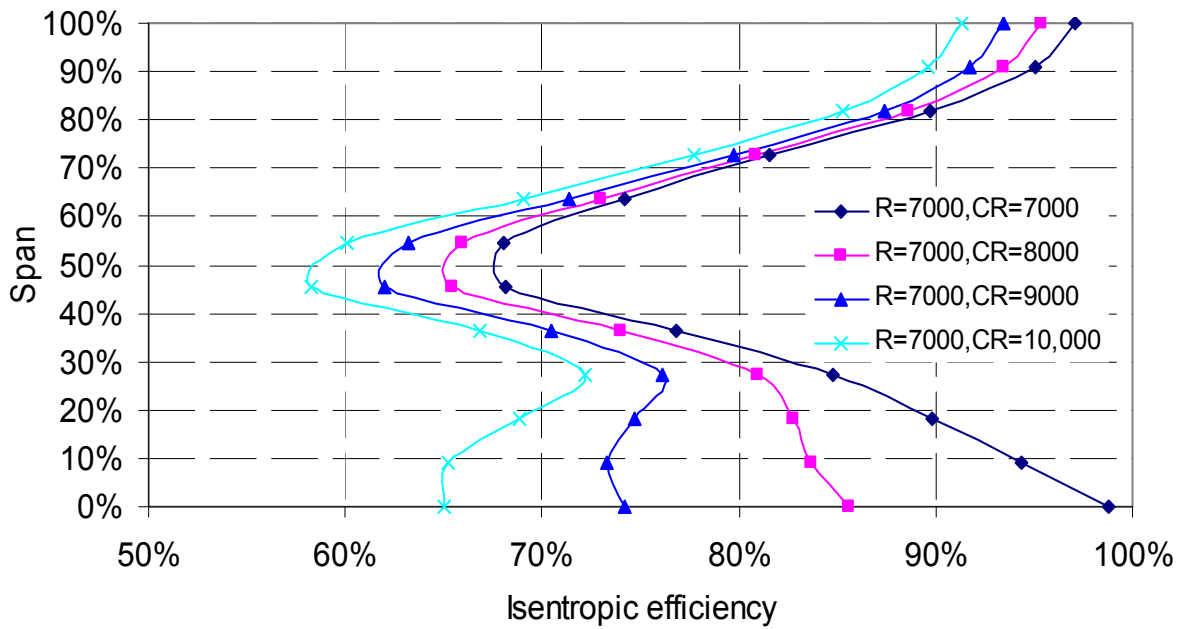
reasonable to have continuously increasing pressure ratios and efficiencies along radial direction. However, distortions have been found in these performance curves and fluid separation can be attributed to this phenomenon. In the case of rotor channels at 30% span, shown in Fig.6-8(upper), minimum relative radial velocity is about 95m/s which is opposite to main radial velocity direction; this negative velocity basically forms a secondary flow and imposes a fluid separation from impeller blade. This secondary flow generates heat and reduces pressure ratio's conversion from kinetic energy, as well as decreasing isentropic efficiency. In case of rotor channel at 45% span shown in Fig.6-8(center), this velocity increases further until it drops down dramatically at 50% span shown in Fig.6-8(lower). Fluctuation of the amplitude reflects the change of incidence angle discussed previously, which also explains torsion curves in these figures. It is therefore can be concluded that this incidence angle's change plays an important role considering pressure loss brought by secondary flow.

As it is mentioned previously, when counter rotating speed increases a large swirl will be induced to rotor channels, and it thus increases the incidence angle at rotor inlet, increasing heat generation and pressure losses. This explains the behavior seen in Fig.6-6, where the rotor's performance drops down a little bit when counter rotor's speed increases, even though a fast speed benefits counter rotor's pressure ratio and efficiency.

In order to reduce secondary flow's effect and improve impeller performance, it thus comes with a design of enlarging hub/tip ratio to 0.75 and maintaining the same blade angle, which is given in the following section.

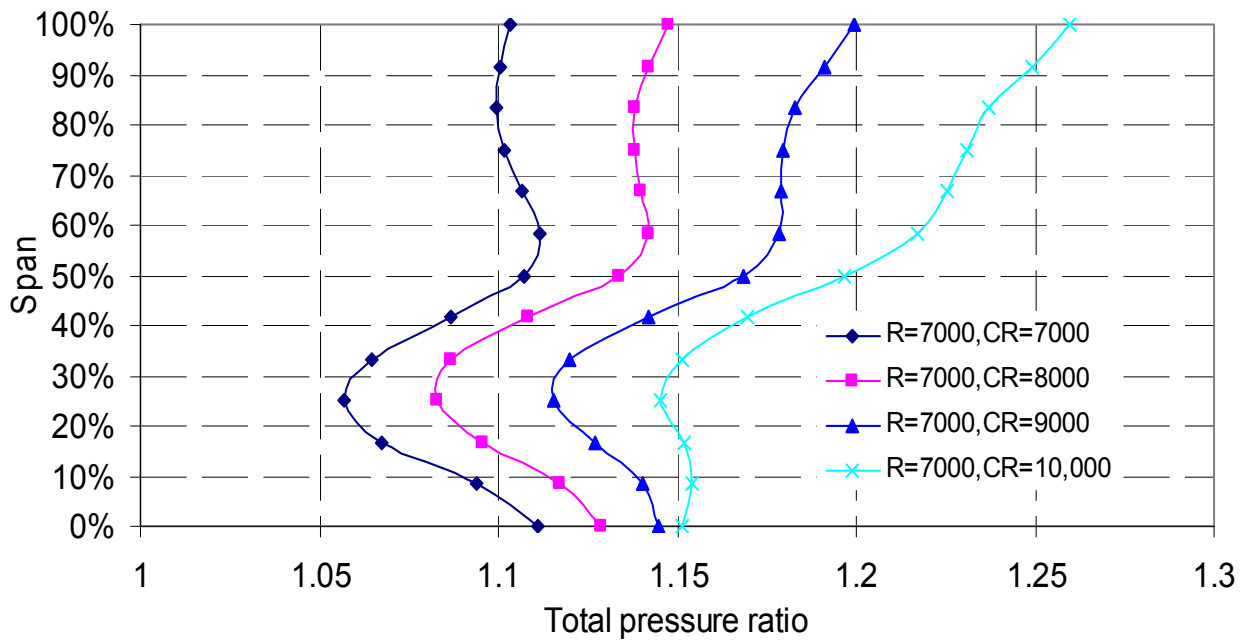


(a)

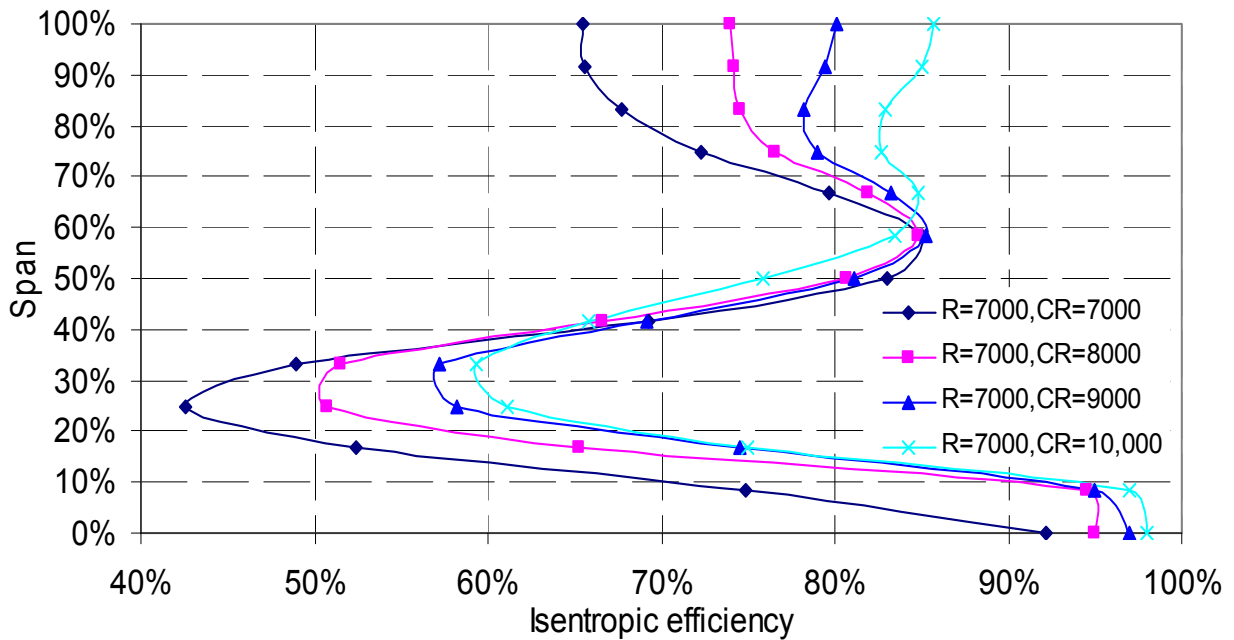


(b)

Figure 6-6 Rotor's pitch averaged total pressure ratio (a) and isentropic efficiency (b) at peak efficiency point ($r < 1$)



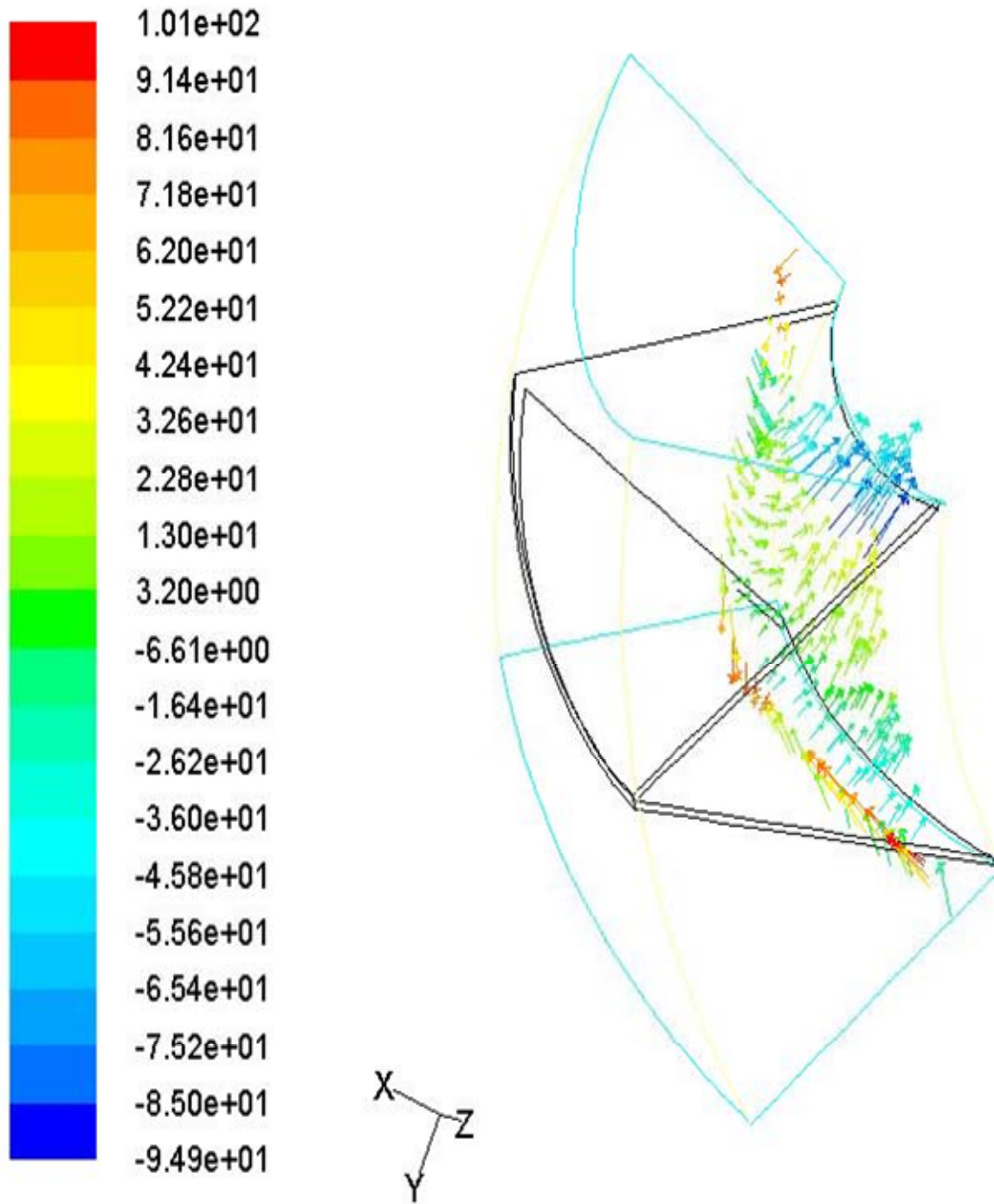
(a)



(b)

Figure 6-7 Counter rotor's pitch averaged total pressure ratio (a) and isentropic efficiency (b) at peak efficiency point ($r>1$)

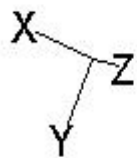
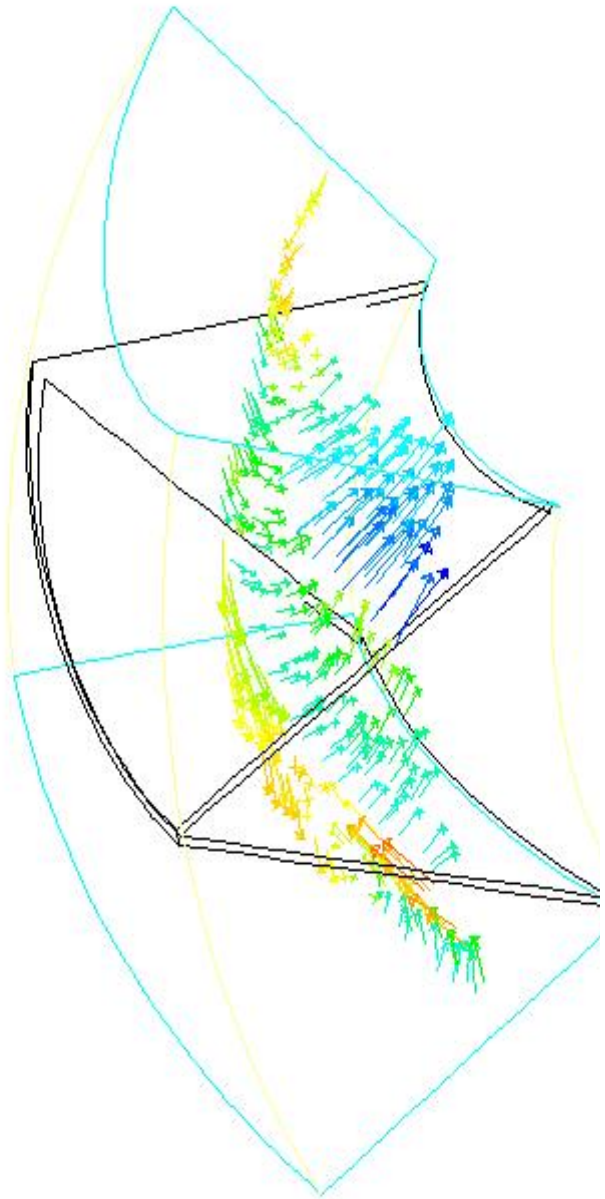
Relative radial velocity, m/s



(a)

Figure 6-8 Comparison of rotor's radial velocity distribution at peak efficiency – (a) 30% span, (b) 45% span, (c) 50% span

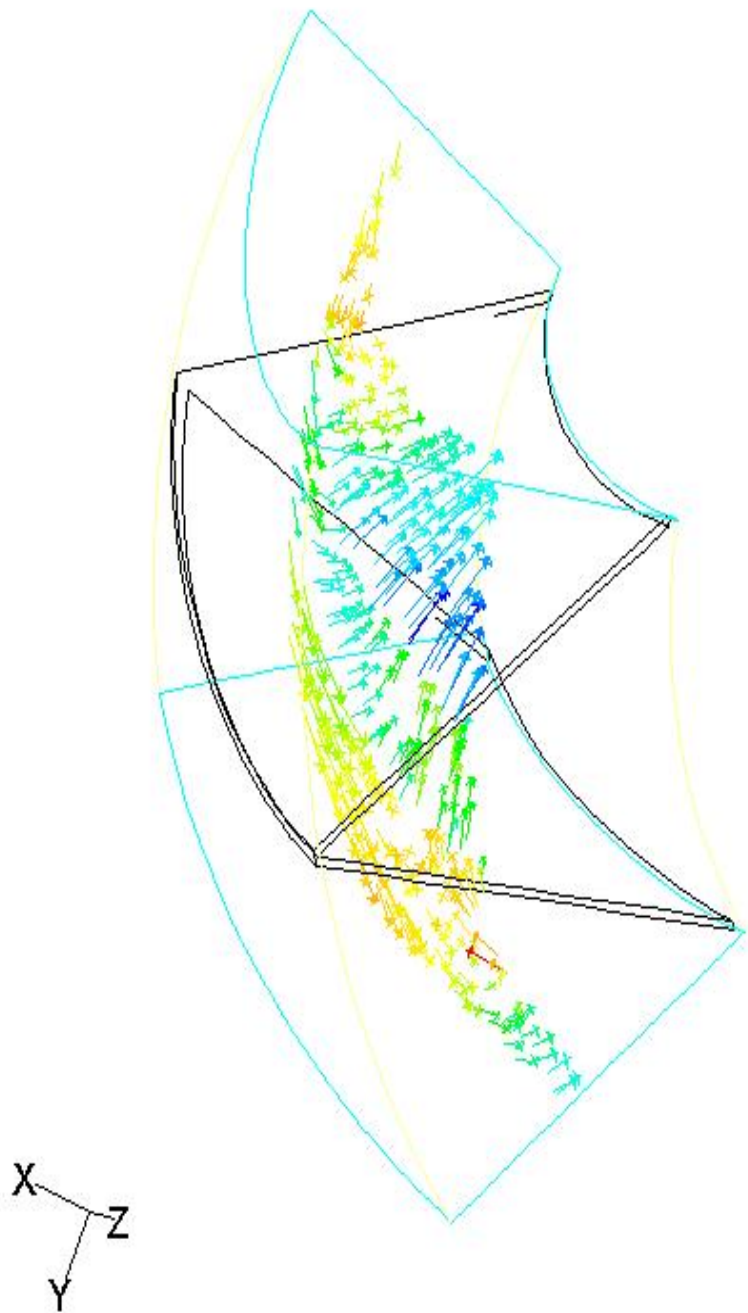
Relative radial velocity, m/s



(b)

Figure 6-8 (cont'd)

Relative radial velocity, m/s

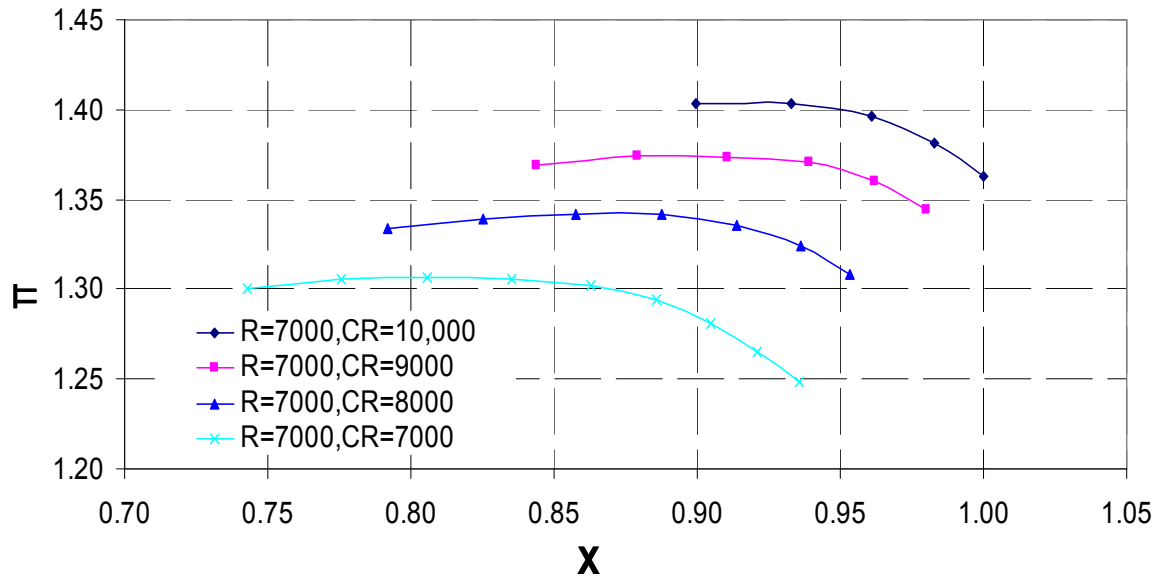


(c)

Figure 6-8 (cont'd)

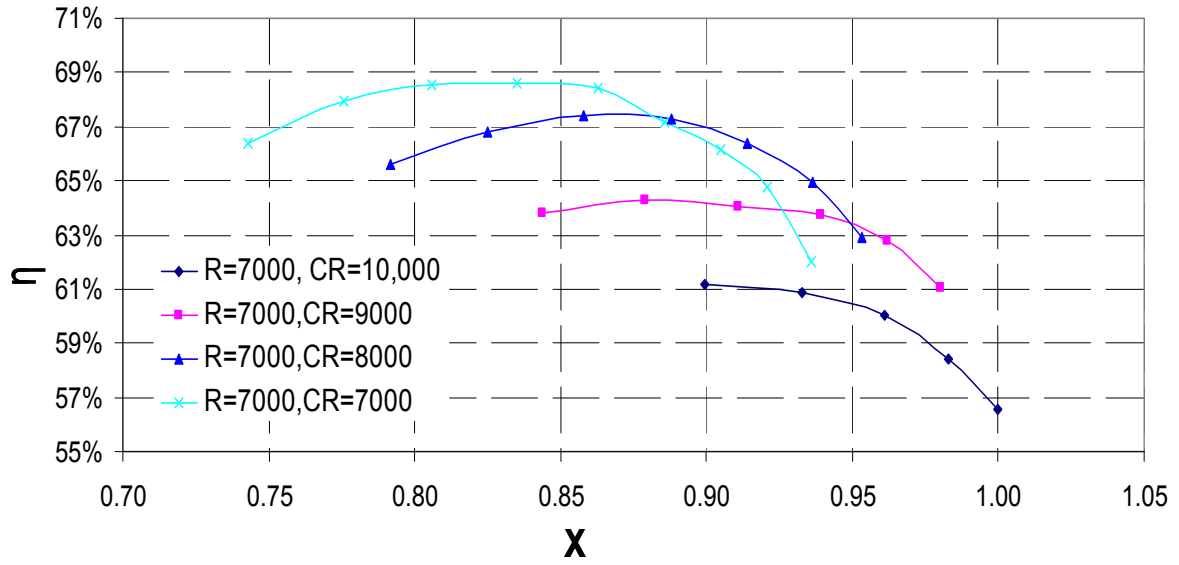
6.2.2 Case 2 0.75 hub/tip ratio

By increasing hub/tip ratio to 0.75, steady state performance curves were mapped in Fig.6-9 and 6-10. In these two figures, peak pressure ratios improve significantly, while stable working range decreases. This is due to contraction of flow area. Since flow inside of the channel is subsonic, when flow cross section contracts to near its critical area, the fluid accelerates and easily gets choked. In addition, mass flow rate decreases at the surge point to reach the incidence angle when stall arises. This is the main reason why the performance map shifts to the left and stable working range narrows. When the counter rotating wheel's speed is the highest, the same phenomenon, as Case 1, can also be observed; stable working range is the narrowest. At the same time, the larger of hub/tip ratio, the larger the turning angle of blade. Thus the amount of momentum transferred from blade to fluid will be greater, as will be the overall stage pressure ratio.



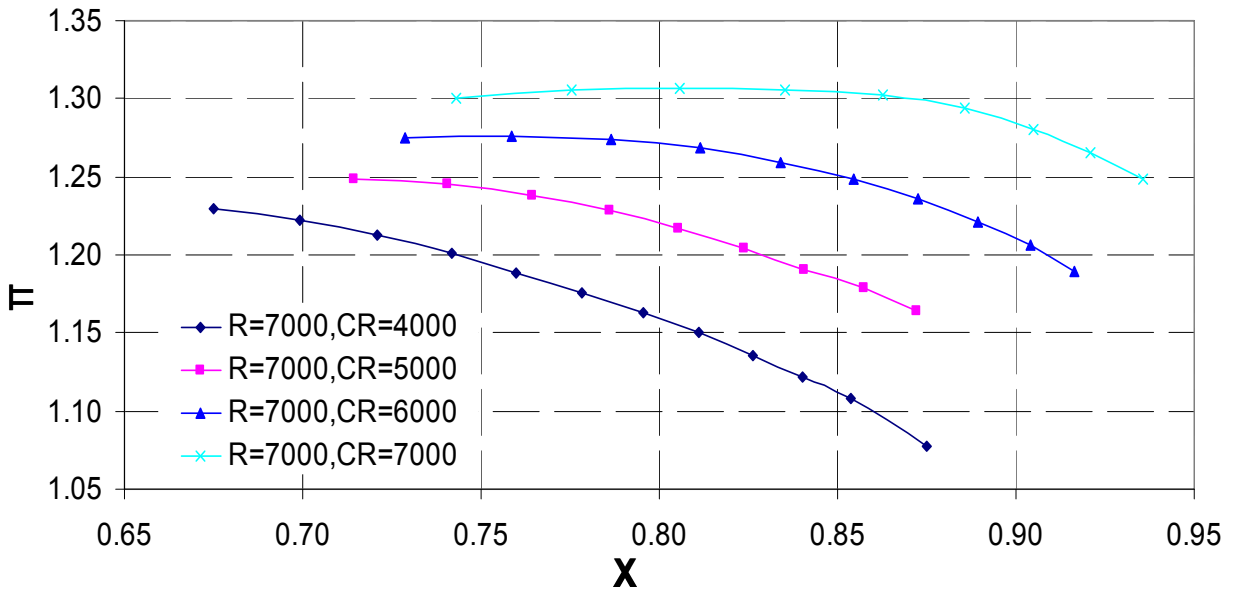
(a)

Figure 6-9 Total pressure ratio curve (a) and isentropic efficiency curve (b) at different $r<1$ rotational speed ratio (0.75ratio)



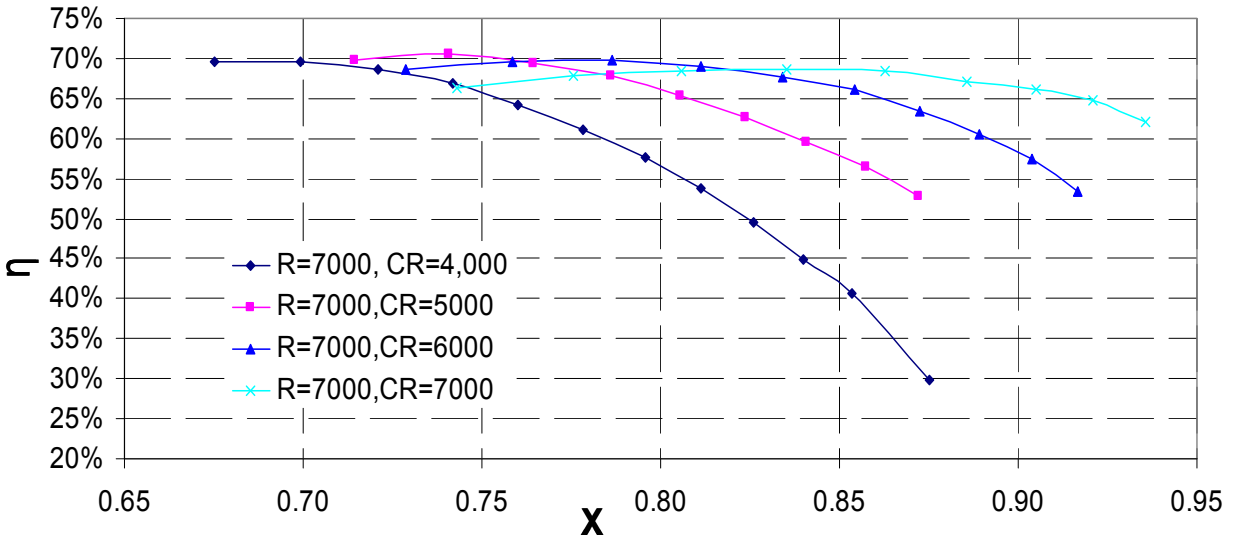
(b)

Figure 6-9 (cont'd)



(a)

Figure 6-10 Total pressure ratio curve (a) and isentropic efficiency curve (b) at different $r>1$ rotational speed ratio (0.75ratio)

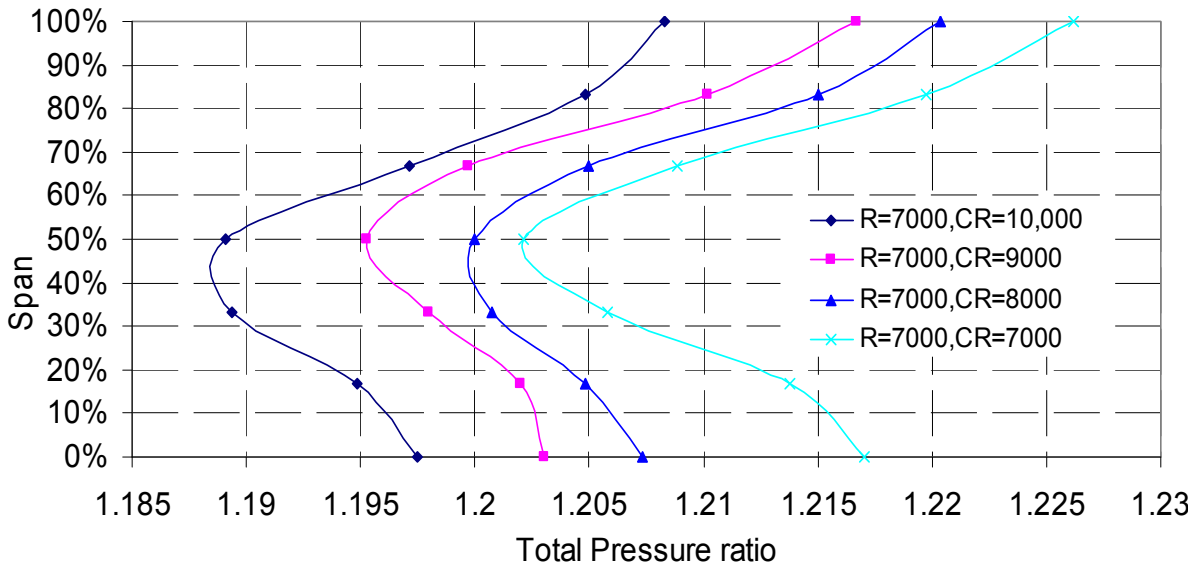


(b)

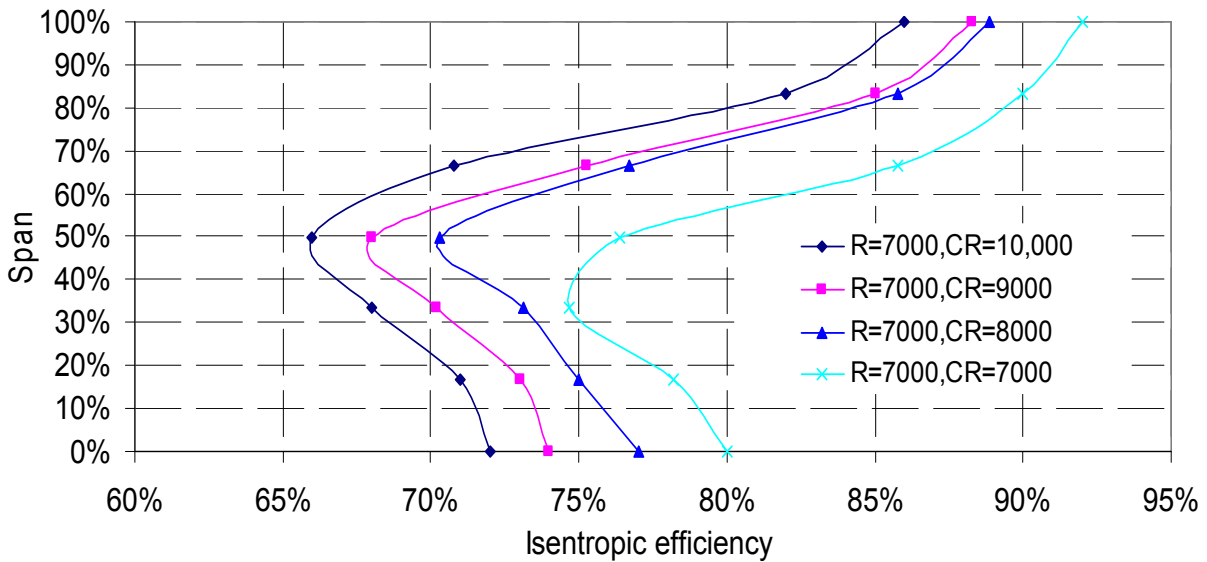
Figure 6-10 (cont'd)

When compared with Fig.6-3, however, peak efficiency in Fig. 6-9 decreases from 75% in case 1 to 69% in bigger hub/tip ratio when speed ratio is less than one. In addition, the efficiency map in bigger hub/tip ratio has the trend that the lower speed relationship interestingly matches with the results at higher speed. The efficiency map is more sensitive to speed ratio, especially when it is less than one. To further explain this phenomenon, detailed circumferential averaged total pressure ratio and efficiency are plotted in Fig.6-11 and 6-12. Both pressure ratio and efficiency curves are still twisted, but less than the smaller hub/tip ratio case, especially for counter rotors. Comparing Fig.6-6 with Fig.6-7, it is interestingly found that distortion existed in Case 1 between span of 30% and 10% which disappeared in Case 2 shown in Fig. 6-11 and 6-12. Only one distortion is found in Case 2, even though a large torsion exists at 50% span in both rotor cases. However when two wheels rotate at the same speed of 7000rpm, efficiency difference from hub to shroud for case 1 is about 30%, whereas for case 2 it is only 20%. A bigger amount of efficiency differences means a bigger separation flow in the channel. By increasing hub/tip ratio performance has been improved throughout the rotor. In counter rotor

part, when comparing with variation of pressure ratio along with radial direction, Fig.6-11 seems to be more serious than Fig.6-6, and it might result a slight efficiency decrease in the whole stage. In addition, simply increasing hub/shroud tip ratio would change the design point and in order to improve isentropic efficiency, new blade angle optimization through CFD approach becomes necessary. Overall, it can be concluded that by the increasing of hub/shroud tip ratio, stage pressure ratio increases significantly. This also causes a decrease in secondary flows influence on each impeller's performance.

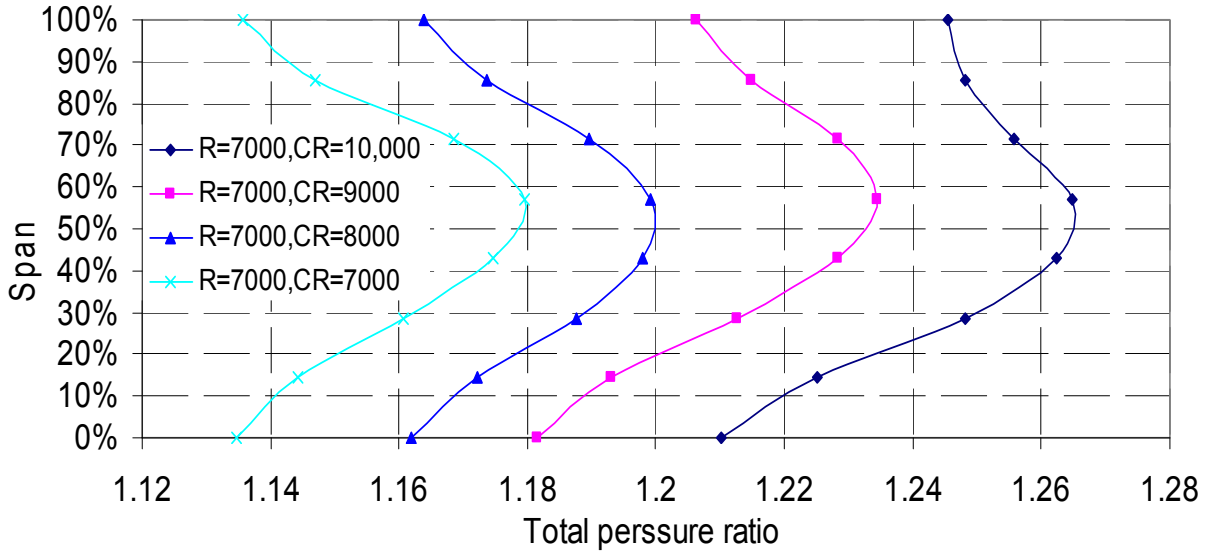


(a)

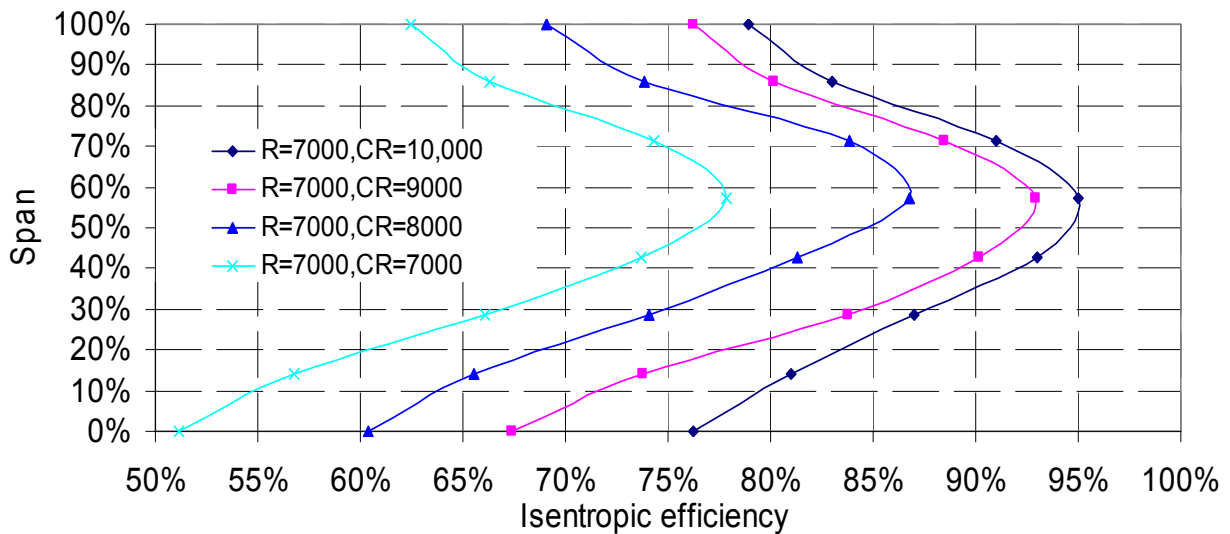


(b)

Figure 6-11 Rotor's pitch averaged total pressure ratio (a) and isentropic efficiency (b) at peak efficiency point ($r < 1$)



(a)



(b)

Figure 6-12 Counter rotor's pitch averaged total pressure ratio (a) and isentropic efficiency (b) at peak efficiency point ($r>1$)

6.3 Summary

A systematic analysis in order to understand water vapor refrigerant's fluid flow characteristics in different hub/shroud ratio of a novel axial counter rotating compressor was carried out. To better demonstrate impeller's geometry, blade angle distribution was derived at

the beginning. Specialties of the impeller pattern were given: with low manufacturing cost using filament winding similar technology, shroud has been integrated with impeller. For this impeller blade angle is different from conventional ones, in that it is a curved line from hub to shroud and it is symmetric to its blade center rather than wheel's center. With 3D CFD, an optimized blade angle at hub/shroud ratio of 0.58, performance curves were mapped. In order to further investigate flow characteristics, single channel's performance was analyzed. Different speed ratios were also simulated for a better understanding of this novel axial impeller's performance. With the same blade angle distribution, hub/shroud ratio increases to 0.75 to decrease secondary flow's influence. Whole stage's performance curves as well as single channel's flow characteristics were also mapped. A comparison between these two hub/tip ratios at different speed ratios was conducted to understand how to utilize this counter rotating technology to compress water vapor as refrigerant.

Using counter rotating technology, stable working range narrows comparing with general rotor-and-stator compressors, since stator vanes were not used directly after rotor. At hub/shroud tip ratio of 0.58, stage pressure ratio has been found to be 1.24 with isentropic efficiency around 75% under subsonic flow conditions. Detailed flow structure inside of one channel shows that a significant secondary flow exists between 30% and 50% span range. When hub/shroud tip ratio increases to 0.75, peak stage pressure ratio increases to 1.41 with efficiency decreases to 61%. The results also show the potential to apply counter rotating technology, using this novel impeller, to compress water vapor as refrigerant. However, further investigations are needed to improve the performance especially for a multi-stage inter-cooling configuration, e.g:

- 1) optimizing each stage's blade angle distribution

2) a mixture of different hub/tip shroud ratios for different stages is necessary from consideration of wide stable working range, high pressure ratio and isentropic efficiency.

CHAPTER 7 Summary and Conclusions

7.1 Summary

Investigation towards utilizing a novel axial composite impeller was conducted to compress water vapor as refrigerant. A manufacturing platform based on CNC machine to produce composite impeller was developed to achieve the concept of weaving composite impeller automatically from endless fiber and epoxy. Experimental test verified the properties against analytical results which show that the platform is able to manufacture composite impeller with qualified mechanical properties. Aerodynamic performance between several impeller patterns with different hub/tip ratio was compared to identify which pattern would provide the best aerodynamic performance for the compression. Stress strain behavior and fatigue life prediction were simulated from rotor dynamics views. In order to better understand the fluid flow inside of specific impeller, flow structures were analyzed, results of which are able to provide reference to optimize hub/tip ratio and blade angle optimization for other patterns.

The idea of using woven impeller to compress water vapor as refrigerant was assessed with both experimental test and FEA & CFD approaches. Designs from manufacturing, aerodynamic and rotor dynamics were taken to realize the idea from concept to reality.

7.2 Conclusions

The conclusions from this research are:

- Compressing water vapor as refrigerant in multi-stage configuration is able to improve coefficient of performance for about 30% comparing with conventional refrigerant R134a. In order to achieve similar or better compression effect, pressure ratio and efficiency per stage in a seven stage inter cooling configuration ought to reach 1.288 and 70% respectively.

- Mechanical properties of woven wheel manufactured through CNC machine based platform have about 10% difference from composite micro mechanical analytical values. Void inside of the composites and impeller blade surface toughness would be explained for reasons. Manufacturing issues for better mechanical properties were advanced. It is recommended that several threads weaving together be able to increase fiber's volume fraction.
- Aerodynamics performance for two typical impeller patterns with various hub/tip ratios were simulated using computational fluid dynamic method. It is found that 8B pattern would be able to produce better pressure ratio and isentropic efficiency. Small triangle inside of the pattern is found to be able to guide fluid flow.
- Based on mechanical properties tested, stress and strain behaviors were simulated using finite element method. Maximum deflection of the wheel reaches about 1.25mm under 7000RPM, which is beyond compressor clearance of 4mm. Fatigue life based on centrifugal stress and aerodynamic stress was predicted and it is concluded that for complicated impeller geometry, aerodynamic stress is important for an accurate fatigue life prediction.
- Further aerodynamic analysis inside of 8B impeller channels show that a large separation exists between 30% and 50% span range. With enlarging hub/tip ratio, separation reduces a little still blade angle optimization is necessary to improve the performance.

7.3 Contributions

The major contributions of this research include bringing a composite impeller manufacturing concept up to the table and discussing its design to compress water vapor as refrigerant.

Automatic manufacturing process enables a large decrease in manufacturing cost which solves the bottle neck of applying axial compressor to compress water vapor as refrigerant. A new methodology based on both aerodynamic and rotor dynamics was developed to better evaluate fatigue life to composite impeller, especially to those with complicated geometries. Another major contribution of this research is analyzing flow structure inside of this novel impeller and providing direction to overcome fluid separation problems.

7.4 Recommendations for Future Work

- Manufacturing approach should be enhanced to produce woven wheel with multi threads simultaneously and fiber volume fraction ratio thus should increase for better mechanical properties.
- Blade angle optimization should be done for each stage in a multi stage compression configuration and hub/tip ratio should also be optimized for the best performance. Depending on the optimized results, woven wheel may be manufactured and test to conduct a further proof-of-concept experiment.
- It would be desirable to further verify rotor dynamic performance of woven wheel experimentally and it would be good stress and strain can be measured when woven wheel rotates. A further aerodynamic performance investigation is necessary to be conducted experimentally to verify turbulence model settings.

BIBLIOGRAPHY

BIBLIOGRAPHY

1. ASHRAE, *ASHRAE Standard 34 -- Designation and Safety Classification of Refrigerants*. 1994, American Society of Heating Ventilating and Air-Conditioning Engineers: Atlanta, GA.
2. Kilicarslan, A.a.N.M., *A Comparative study of Water as a Refrigerant with some current Refrigerants*. International Journal of Energy Research, 2005. **29**: p. 947-959.
3. Brandon F. Lachner Jr., G.F.N., Douglas T. Reindl, *The commercial feasibility of the use of water vapor as a refrigerant*. International Journal of Refrigeration, 2007. **30**(4): p. 699-708.
4. Dixon, S.L., *Fluid Mechanics and Thermodynamics of Turbomachinery*. 1998: Butterworth-Heinemann.
5. Albring P., A.R., Burandt B., Müller N., , *Grundlagenuntersuchungen energierationeller Kreisprozesse mit Wasser als Kältemittel und Erprobung einer Versuchs-Großanlage (Fundamental investigations of energy efficient cycles with water as a refrigerant and test of a full-size test unit)*, in *Abschlußbericht (final report) zum BMBF-Forschungsvorhaben 0326921A*. . 1999.
6. Orshoven, D.V., Klein, S. A., and Beckman, W. A, *Investigation of Water as a Refrigerant*. Journal of Energy Resources Technology, 1993. **115**(4).
7. Kuhn-Kinell, J., *New age water chillers with water as refrigerant*, CERN-European Organization for Nuclear Research: Geneva.
8. Wight, S.E., Yoshinaka, Tsukasa, Le Drew, Brenda A., D'Orsi, Nicholas C., *The Efficiency Limits of Water Vapor Compressors*, in *ARTI-21CR/605-10010-01*. 2000, The Air-Conditioning, Heating and Refrigeration Institute (AHRI).

9. Z, Z., *Development of large capacity high efficiency mechanical compression (MVC) units*. Desalination, 1994. **96**: p. 51-58.
10. Albring, P., Burandt B and Schenk, N, *Water Vapour Compression: Application and Outlook*. KI Luft Kältetech DE, 2002. **38**(6): p. 276-281.
11. Mallick, V., *Thermoplastic composite based processing technologies for high performance turbomachinery components*. Composites: Part A, 2001. **32**: p. 1167-1173.
12. Mueller, N., et al. *An electric flight concept*. in *3rd International Symposium on Innovative Aerial/Space Flyer Systems*. Nov 2006. Tokyo.
13. Allen Eyler, N.M. *Simulation and production of wound impellers*. in *ASME Turbo Expo 2008: Power for land, sea and air, GT2008-51310*. 2008. Berlin.
14. M.O. McLinden, D.A.D., *Quest for alternatives*. ASHRAE Journal, 1987.
15. Demiss A. Amibe, Q.L., Norbert Mueller. *Multi stage variable speed turbo compressor for enhancing seasonal energy efficiency ratio of air conditioners using R718 as refrigerant*. in *ASME Turbo Expo 2010*. 2010. Glasgow, UK.
16. Saari, J., Backman, J., Peussa, J., . *Conceptual design of a multistage high-speed motor driven air compressor*. in *Proceedings of ASME Turbo Expo 2008: Power for Land, Sea and Air*. 2008.
17. Bathie, W.W., *Fundamentals of Gas Turbines*. second ed ed. 1996: John Wiley & Sons, Inc.
18. M.J, R., *Mechanics of composite materials*. 85-98.
19. Eyler.A, N.M., *Simulation and production of wound impellers*, in *ASME-IMECE Paper 2008-51310*. 2008.
20. Cohen, D., S.C. Mantell, and L. Zhao, *The effect of fiber volume fraction on filament wound composite pressure vessel strength*. Composites Part B: Engineering, 2001. **32**(5): p. 413-429.
21. *ASTM International Standars Worldwide*, in *Annual Book of ASTM Standards*. D792.

22. Jones, R.M., *Mechanics of composite materials*. 1st ed. 1975: McGraw-Hill Book Company. 85-98.
23. Gibson, R.F., *Principles of composite materials mechanics* 1994: McGraw-Hill Inc.
24. A. Banerjee, e.a., *Model and experimental study of fiber motion in wet filament winding*. Composites Part A: Applied science and manufacturing, 1998. **29**(3): p. 251-263.
25. Tuttle, M.E.B., H.F, *Resistance-foil strain-gage technology as applied to composite materials*. Experimental Mechanics, 1984. **24**: p. 54-65.
26. Mallick, V., *Thermoplastic composite based processing technologies for high performance turbomachinery components*. Composites Part A: Applied science and manufacturing, 2001. **32**(8): p. 1167-1173.
27. Genta, G., *Kinetic energy storage: theory and practice of advanced flywheel systems*. 1985, London: Butterworth & Co.
28. Kaw, A.K., *Mechanics of composite materials*. 2end ed. 2006: Taylor & Francis Group. 203-311.
29. Li, Q., J. Wang, and N. Mueller. *On the realization of filament wound composite impeller for water refrigerant*. in *ASME Paper IMECE2009-12786*. 2009. Orlando.
30. ANSYS, *ANSYS FLUENT 12.0 User's Guide*, R.A. Inc, Editor. 2003.
31. Lei, V.-M., *A simple criterion for three dimensional flow seperation in axial compressors*, in *Massachusetts Institute of Technology*. 2006, Massachusetts Institute of Technology.
32. Lauder, B.E.a.S., D.B., *The numerical computation of turbulent flows*. Comput. Math. Appl. Mech. Engrg, 1974. **3**: p. 269-289.
33. Tousi, R.A.T.a.A.M., *Design and CFD analysis of centrifugal compressor for a microgasturbine*. Aircraft Engineering and Aerospace Technology: An International Journal. **79**(2): p. 137-143.
34. MN, Z., *Collections on aeroengine service life and speeding-up simulated trial operation (in Chinese)*. 1991, Shenyang: Liaoning Science Technology Press.

35. Burns, J., *Gas turbine engine blade life prediction for high cycle fatigue*. The technical cooperation program (TTCP), 1998. **P-TP1**.
36. PC, C., *Compressor blade high cycle fatigue life--case study*. The technical cooperation program (TTCP), 1998. **P-TP1**.
37. Troshchenko V.T, P., A.V, *Fatigue strength and life of compressor blades for marine gas turbine engines*. Strength of Materials, 1999. **31**(1).
38. TSR, R., *A review of recent aeroelastic analysis methods for propulsion at NASA Lewis research center*. NASA Technical Paper, 1993. **3406**.
39. Walls DP, D.R., Cunningham SE. , *Damage tolerance based life prediction in gas turbine engine blades under vibratory high cycle fatigue*. Journal of Engineering for Gas Turbines and Power, 1997. **119**: p. 143-6.
40. Witek L, W.M.a.P.A., *Fracture analysis of compressor blade of a helicopter engine* Engineering Failure Analysis, 2008. **16**(5): p. 1616-1622.
41. Lijie Chen, Y.L., Liyang Xie, *Power-exponent function model for low cycle fatigue life prediction and its applications -- Part II: Life prediction of turbine blades under creep-fatigue interaction* International journal of fatigue, 2007. **29**: p. 10-19.
42. A. Kermanpur, H.S.A., S. Ziaei-Rad, N. Nourbakhshnia, M. Mosaddeghfar, *Failure analysis of Ti6Al4V gas turbine compressor blades*. Engineering Failure Analysis, 2008. **15**: p. 1052-1064.
43. Eyler Allen, M.N., *Simulation and production of wound impellers*, in *ASME Paper IMECE2008-51310*. 2008.
44. Li Qubo, J.W., Norbert Mueller, *On the realization of filament wound composite impeller for water refrigerant*, in *ASME Paper IMECE2009-12786*. 2009: Orlando.
45. Li Qubo, P., J, Mueller, N, *Aerodynamic Design and CFD Analysis of a Novel Axial Compressor*, in *40th AIAA Fluid Dynamics Conference 2010*: Chicago.
46. Li Qubo, W.J.a.M.N., *On the realization of filament wound composite impeller for water refrigerant*, in *ASME Paper IMECE2009-12786*. 2009: Orlando.

47. ANSYS, *ANSYS Theory Reference Manual* 2003.
48. Tsai SW, H.S., Gay D, *Composite materials, design and applications*. 2003: CRC Press
49. ANSYS, *ANSYS FLUENT 12.0 User's Guide*, R.A. Inc, Editor. 2003.
50. Li Qubo, J.P.a.N.M., *Aerodynamic design and CFD analysis of a novel axial compressor*, in *40th AIAA Fluid Dynamics Conference and Exhibit*. 2010: Chicago.
51. Ye, L., *On fatigue damage accumulation and material degradation in composite materials*. Compos Sci Technol 1989. **36**: p. 339-50.
52. Mahmood M. Shokrieh, R.R., *Simulation of fatigue failure in a full composite wind turbine blade*. Composite Structures, 2006. **74**: p. 332-342.
53. Charewics A, D.I., *Damage mechanics and accumulation in graphite/epoxy laminates*. Composite Materials: fatigue and fracture, 1986. **ASTM STP 907**: p. 247-97.
54. Lee JW, D.I., Yaniv G, *Fatigue life prediction of cross-ply composite laminated* Composite Materials: fatigue and fracture, 1989. **ASTM STP 1012** p. 19-28.
55. Shokrieh M, L.L., *Progressive fatigue damage modeling of composite materials, Part I: Modeling*. Journal of Composite Materials, 2000. **34**(13): p. 1056-80.
56. Miner, M.A., *Cumulative damage in fatigue*. Journal of Applied Mechanics, 1945. **12**(3): p. 159-164.